NANOFIBER BASED LIGHT-MATTER INTERACTION FOR HIGH PERFORMANCE LASER SPECTROSCOPY

QI YUN

PhD

The Hong Kong Polytechnic University

2020

The Hong Kong Polytechnic University

Department of Electrical Engineering

Nanofiber based light-matter interaction for high performance laser spectroscopy

QI YUN

A thesis submitted in partial fulfillment of the requirements for

the degree of *Doctor of Philosophy*

December 2019

CERTIFICATE OF ORIGINALITY

I hereby declare that this thesis is my own work and that, to the best of my knowledge and belief, it reproduces no material previously published or written, nor material that has been accepted for the award of any other degree or diploma, except where due acknowledgement has been made in the text.

…… …….. (Signed)

……QI Yun…….. (Name of student)

Abstract

Trace gas detection is critical for industrial safety, environmental monitoring and public security. Among the various kinds of techniques, the molecular spectroscopy may be the most all-round method for trace gas detection, in consideration of its high selectivity and sensitivity. Optical nanofiber is widely recognized as an excellent platform for light-matter interaction, due to its guided-wave property, high intensity of the evanescent field and the immunity from mode noise. The nanofiber based molecular spectroscopy is then expected to achieve promising performance in trace gas sensing, which is the research target of this thesis.

Photothermal interferometry (PTI) is generally a more sensitive method for trace gas detection compared with the direct absorption spectroscopy (DAS) for the same optical absorption length, because the power of pump beam in PTI spectroscopy can be set sufficiently high to achieve larger phase modulation without the issue of power saturation for the probe beam. Both the traditional free space and the newly-developed hollow-core photonic bandgap (HC-PBG) fiber based PTI rely on the absorption induced temperature and thus refractive index (RI) change of the air, which, however, has a relatively low thermo-optic coefficient compared with solid materials. An intriguing advantage of the nanofiber based PTI is that the generated heat due to evanescent wave absorption can be transferred to the nanofiber. Due to the orders of magnitude higher thermo-optic coefficient of the core material than the air, the phase modulation amplitude and thus the photothermal signal in nanofiber based PTI spectroscopy can be much improved. With a piece of 12 mm long and 800 nm-diameter silica nanofiber, the trace acetylene detection limit of 600 parts per billion (ppb) have been achieved. Numerical simulations predict that for the nanofiber/waveguide made of materials with much larger thermo-optic coefficients, such as silicon, further tremendous enhancement in photothermal phase modulation efficiency can be achieved.

The nanofiber based PTI method is only applicable to the molecules with strong absorption lines and fails for the homodiatomic ones such as hydrogen. However, the high-intensity evanescent field

associated with the nanofiber makes the stimulated Raman scattering (SRS) process for Raman-active molecules much more efficient compared with the free space and the HC-PBG fiber counterparts. The nanofiber enhanced SRS for high-sensitivity and fast-response hydrogen detection is demonstrated. The high sensitivity results from the large SRS gain and the single-mode operation of the nanofiber. The trace hydrogen detection limit of 3 ppm with response time less than 10s has been achieved using a piece of 48-mm-long and 700-nm-diameter silica nanofiber. The change of polarization states in both the pump and probe beam should be the primary cause for the long term signal drift, which is also addressed.

The evanescent field is tightly constrained around the nanofiber, so the light-matter interaction time is limited due to the inevitable thermal motion of the molecules, which results in additional transit time broadening. The shorter the interaction time, the broader the linewidth and thus the lower the peak absorption coefficient of the gas molecules. To which extent the transient time effect contributes to the overall linewidth, is explored by numerical simulation using the density matrix method as well as verified by experiments. It is concluded that for the absorption lines of common molecules in the near infrared band at the atmospheric pressure, the transit time broadening is negligible compared with the dominant collisional broadening. However, for the nanofiber-based SRS of hydrogen, the situation is much different. Due to the lighter molecular weight and thus higher thermal velocity, the transit time effect of hydrogen is the dominant broadening factor over both the collisional and Doppler broadening at the atmospheric pressure.

Besides the spectroscopic applications of nanofiber, the potential ability of light manipulation by nanofiber is also explored. It is found that the non-circularly symmetric optical field of the linearly polarized fundamental modes can produce a transient temperature distribution with a two-fold rotational symmetry in the surrounding air, which results in a transient birefringence of the nanofiber. This transient photothermal phenomenon can then be exploited for all-optical polarization switching, which may find application in optical communication. With a piece of 15-mm-long and 600 nm-diameter nanofiber in pure acetylene of 4 bar and a 15 ns pulsed pump with peak power of 30W,

polarization switching with efficiency up to 90 %, on and off time of 11 and 37 ns have been achieved.

Publications Arising from the Thesis

Journal Articles

Y. Qi, F. Yang, Y. Lin, W. Jin, and H. L. Ho, "Nanowaveguide Enhanced Photothermal Interferometry Spectroscopy," *Journal of Lightwave Technology,* vol. 35, pp. 5267-5275, 2017.

Y. Qi, Y. Zhao, H. Bao, W. Jin, and H. L. Ho, "Nanofiber enhanced stimulated Raman spectroscopy for ultra-fast, ultra-sensitive hydrogen detection with ultra-wide dynamic range," *Optica,* vol. 6, pp. 570-576, 2019.

Y. Qi, W. Jin, and H. L. Ho, " Investigation of the transit-time broadening in optical nanofiber based spectroscopy," *Optics Express*, vol. 28, pp. 8324-8330, 2020.

Z. Li, Z. Wang, **Y. Qi**, W. Jin, and W. Ren, "Improved evanescent-wave quartz-enhanced photoacoustic CO sensor using an optical fiber taper," *Sensors and Actuators B: Chemical,* vol. 248, pp. 1023-1028, 2017/09/01/ 2017.

F. Yang, Y. Zhao, **Y. Qi**, Y. Z. Tan, H. L. Ho, and W. Jin, "Towards label-free distributed fiber hydrogen sensor with stimulated Raman spectroscopy," *Optics Express,* vol. 27, pp. 12869-12882, 2019/04/29 2019.

Y. Tan, W. Jin, F. Yang, **Y. Qi**, C. Zhang, Y. Lin*, et al.*, "Hollow-Core Fiber-Based High Finesse Resonating Cavity for High Sensitivity Gas Detection," *Journal of Lightwave Technology,* vol. 35, pp. 2887-2893, 2017/07/15 2017.

F. Yang, Y. Tan, W. Jin, Y. Lin, **Y. Qi**, and H. L. Ho, "Hollow-core fiber Fabry–Perot photothermal gas sensor," *Optics Letters,* vol. 41, pp. 3025-3028, 2016/07/01 2016.

Conference articles

Y. Qi, Y. Zhao, H. Bao, W. Jin, H. L. Ho, and H. Luo, "Nano-taper enhanced stimulated Raman gain spectroscopy for high sensitivity hydrogen detection," in *26th International Conference on Optical Fiber Sensors*, Lausanne, 2018, p. FA3. (received best confernece paper award)

F. Yang, Y. Zhao, **Y. Qi**, Y. Tan, H. L. Ho, and W. Jin, "Label-free distributed hydrogen sensing with stimulated Raman scattering in hollow-core fibers," in *26th International Conference on Optical Fiber Sensors*, Lausanne, 2018, p. TuE4.

Acknowledgements

First, I would like to express the sincerest gratitude to my supervisor Prof. Wei Jin for his invaluable guidance and continuous support. His prudent research attitude and great enthusiasm set a precious example for me. The meeting and talks with him are always enlightening and inspiring. His knowledge, patience and honesty helped me overcome the difficulties throughout my PhD study.

Special thanks to Dr. Hoi Lut Ho, Dr. Chao Wang, Dr. Fan Yang, Dr. Yuechuan Lin and Dr. Yanzhen Tan for your great help when I just started my PhD study as well as the continuous support later.

I would also like to acknowledge the group members Dr. Congzhe Zhang, Dr. Yinping Miao, Mr. Yan Zhao, Mr. Haihong Bao, Dr. Haipeng Luo, Mr. Pengcheng Zhao, Miss Han Gao, Mr. Feifan Chen, Miss Yingzhen Hong, Dr. Shoufei Gao and Dr. Shoulin Jiang for the useful discussions and kind help.

Finally, I want to express my deep gratitude to my beloved families. Thanks for your unconditional support and continuous encouragement.

Table of Contents

List of Figures

List of Tables

List of Acronyms

PTI	photothermal interferometry
DAS	direct absorption spectroscopy
HC-PBG	hollow-core photonics bandgap
RI	refractive index
ppb	parts per billion
SRS	stimulated Raman scattering
HWHM	half width half maximum
FWHM	full width half maximum
WMS	wavelength modulation spectroscopy
SNR	signal to noise ratio
FEM	finite element method
SMF	single mode fiber
MZI	Mach-Zehnder interferometer
CW	clockwise
CCW	counter-clockwise
BPD	balanced photodetector
DFB	distributed feedback
EDFA	Erbium doped fiber amplifier
ASE	amplified spontaneous emission

AOM	acousto-optic modulator
BBS	broad band source
PC	polarization controller
PZT	piezoelectric transducer
PD	photodetector
LPF	low-pass filter
HPF	high-pass filter
WDM	wavelength division multiplexer
CYTOP	cyclic transparent optical polymer
SRG	stimulated Raman gain
SRL	stimulated Raman loss
MFD	mode field diameter
DF	dust filter
MFC	mass flow controller
ppm	parts per million
LPG	long period grating
FBG	fiber Bragg grating
FPI	Fabry-Perot interferometer
SPR	surface plasma resonance
EWA	evanescent wave absorption
SRSTL	stimulated Raman scattering thermal lens

SRSPA	stimulated Raman scattering photoacoustic
SR	spontaneous Raman
MMF	multi mode fiber
Hi-Bi	highly-birefringent
OA	optical attenuator
VP	vacuum pump
PG	pressure gauge
SG	signal generator
DFS	Doppler free saturation absorption spectroscopy
DC	direct current
PBS	polarization beam splitter

Chapter 1 Introduction

1.1 Literature review

Trace gas detection is important for industrial safety, production control, environmental monitoring, medical examination and public security [1]. In coal mining, real-time monitoring of methane is critical to the prevention of mine gas explosion [2]. In semiconductor fabrication, precise controlling of each gas phase component is the key point for material growth by the technique of chemical vapor deposition [3]. Continuous monitoring of the concentration of greenhouse gases, such as carbon dioxide, methane and nitrous oxide, in atmosphere helps slow down the progress of global warming [4]. In health care, detection of the concentration of specific kinds of trace components in exhaled gas whose abnormal level are related with certain disease helps in early diagnosis [5]. In public security, detection of trace gas released from explosive and toxic material can contribute to fighting against terrorism [6].

Inasmuch as its wide and irreplaceable applications, there are various techniques for trace gas sensing, such as the chromatography combined with mass spectrometry technique [7, 8], electrochemistry [9-11] and photoionization [12, 13]. For the method of chromatography combined with mass spectrometry, the gas sample is first separated into different parts according to their affinity with the stationary phase material in the tube. Then each part is successively transported into the mass spectrometry, where the gas sample is ionized for analysis of their mass-to-charge ratio and plot of the mass spectrum, with which the species and their concentration can be confirmed. Despite of the high sensitivity of this technique, it has limitations for field applications, due to the time-consuming measurement process, large size and high price [14]. The electrochemistry technique is the most prevalently adopted one for present commercial gas sensor. Although there are lots of implementation models, such as fuel cells [15], semiconductor [16], and catalytic combustion [17], each of them is based on the chemical reaction of the target gas species between or mediated by the gas sensor with the resulting change of current, voltage or heat detected for

determination of gas concentration. Those electrochemistry-based methods have the advantages of small size, light weight and low price, but they all share the problems of low selectivity and temperature sensitivity [18, 19].

Compared with abovementioned techniques, infrared laser spectroscopic method offers great advantages in trace gas sensing [21, 22]. It is based on the unique transition lines of molecules, which makes it highly selective. As the wavelength of excitation laser beam locates within infrared band with low photon energy, the trace gas molecules would not be ionized or break down, so that the gas sample is kept intact. Among the various kinds of infrared laser spectroscopic techniques, the absorption spectroscopy is the most fundamental one, in which a beam of light with its wavelength matching the transition line of the gas molecule is attenuated when propagation through the gas sample. By monitoring the degree of attenuation of the transmitted light beam, the

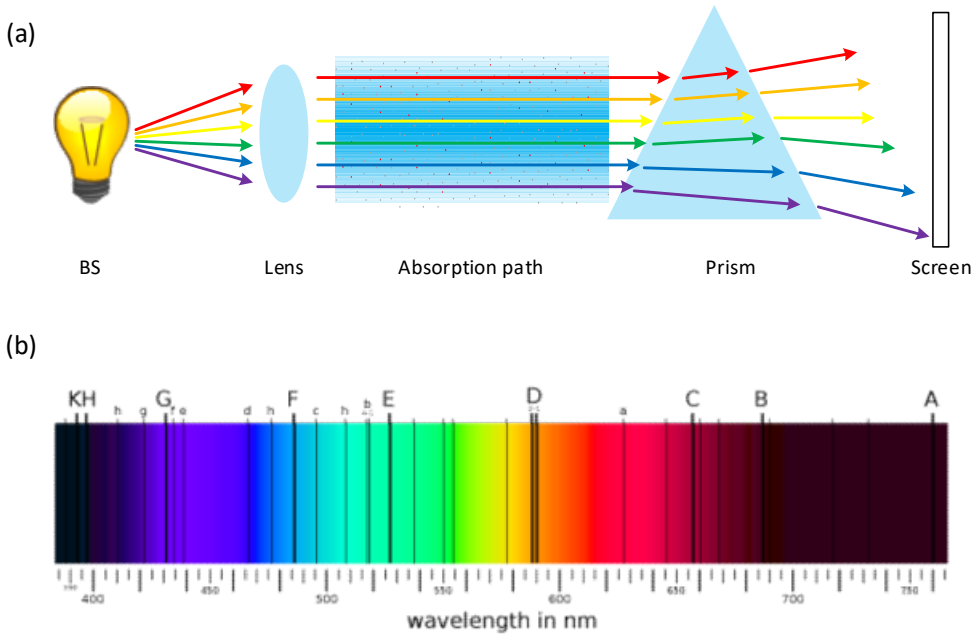

Fig. 1.1 Illustration of the primitive absorption spectroscopy. (a) A representative experimental setup, (b) A typical solar spectrum. The dark lines are called as Fraunhofer lines which is due to the absorption of solar atmosphere [20].

concentration of the target gas species can be retrieved [23]. Before the appearance of laser, which is first predicated by Einstein in 1917, later systematically founded by Townes and Schawlow in 1950s and finally built by Maiman in 1960, the primitive absorption spectroscopy technique uses the broadband halogen or mercury lamps as the light source. To distinguish the unique absorption line, a spectrometer such as the prism or grating is needed to resolve the spectrum [24], as illustrated in Fig. 1.1(a). Due to the limited spectral resolution, the performance of traditional absorption spectroscopy is circumscribed. As an example, Fraunhofer only discovered 570 dark lines in the solar spectrum, with the relatively strong absorption lines denoted by the letters from A to K, as shown in Fig. 1.1(b), while there have been thousands of lines discovered nowadays. With the advent of narrow linewidth laser source, the absorption spectroscopy starts to boom with various implementation configurations coming out, including cavity enhanced absorption spectroscopy [25, 26], cavity ring-down spectroscopy [27, 28] and modulation spectroscopy [29, 30], all with the aims to enhance the signal amplitude or to reduce the noise and thus to increase the sensitivity. In regards to the attempt to obtaining higher signal level, the cavity enhanced methods shows the most straightforward benefits due to the much longer absorption path, according to the Beer-Lambert law [24]:

$$\Delta P(\nu) = P_0(\nu) \cdot \left(1 - e^{-N\alpha_0(\upsilon)z}\right), \qquad (1.1)$$

where, the $P_0(\nu)$ is the power of incident light beam, $\alpha(\upsilon)$ is the absorption coefficient, N is the

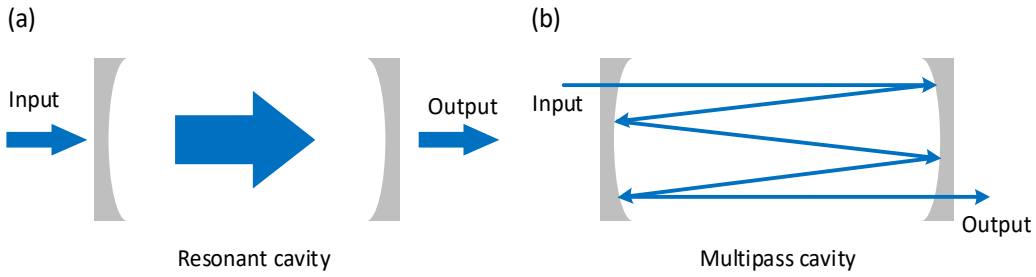

Fig. 1.2 Illustration of the (a) cavity ring-down and (b) cavity enhanced absorption spectroscopy.

molecular density of the trace species and z is the length of absorption path. In the low concentration range, the exponent $N\alpha_0 z$ is close to zero. So, by performing the Taylor expansion to the exponential and taking the first two terms, the above equation is reduced to:

$$\Delta P(\nu) = P_0(\nu) N \alpha_0(\upsilon) z, \qquad (1.2)$$

As seen, the absorption signal is directly proportional to the $P_0(\nu)$ and z. So both the methods of increasing optical power and interaction length, can effectively enhance the signal, just as what is attempted to achieve by the cavity ring-down spectroscopy and the cavity enhanced absorption spectroscopy, as shown in Fig. 1.2(a) and 1.2(b) respectively. On another hand, the sensitivity can be improved by reduction in noise. Generally, the noise is quite large in the low-frequency range and drops gradually with increased operating frequency. So, by applying a modulation to the light beam, such as intensity modulation or frequency modulation at a relatively higher frequency and then demodulating it after the interaction with the gas species, the interference from the relatively large low-frequency noise would be suppressed.

For the infrared laser spectroscopy, besides the most basic one of direct absorption, there are also kinds of indirect methods, such as photothermal and photoacoustic spectroscopy [31-34]. These two techniques share the same origination that the absorbed energy by the trace molecules is released to the surrounding, heating up the air, as shown in Fig. 1.3. The temperature change will generate

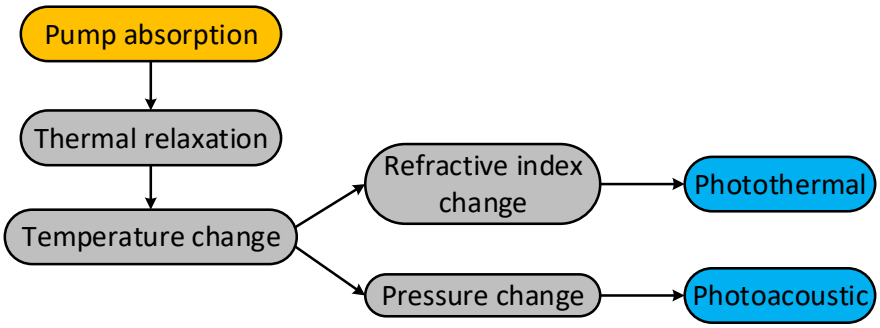

Fig. 1.3 Illustration of the generation of photoacoustic and photothermal effects.

sound wave which can then be detected by the acoustic sensor resulting in photoacoustic signal while the refractive index change can be probed and demodulated by another beam of light using the interferometry technique and generate photothermal signal [35]. As the power of pump beams in these two indirect methods can be set very high without the problem of power saturation for the probe beam, high sensitivity in trace gas detection can be achieved.

All the above mentioned techniques can be combined with the fiber-optic technologies. Not only will the combination keep the existing advantages as in free space, but it also embraces the intrinsic benefits of fiber optics, such as flexible implementation, convenient multiplication, remote interrogation and electromagnetic interference immunity [36-38]. The simplest hybridization between the traditional free space absorption spectroscopy and the fiber-optics may be the collimated lens pair structure with the fibers pigtailed for optical connection, as shown in Fig. 1.4(a) [39]. Although the sensing part is still the free-space one, the fiber-optic connection in this scheme alleviate the cumbersome task of optical path alignment as in traditional absorption spectroscopy and thus makes the whole system flexible and compact. To improve the sensitivity, the strategy of cascaded combination of the collimated lens pairs can be adopted to increase the total absorption path, as shown in Fig. 1.4(b) [40]. Although these two kinds of schemes exhibit the advantages of

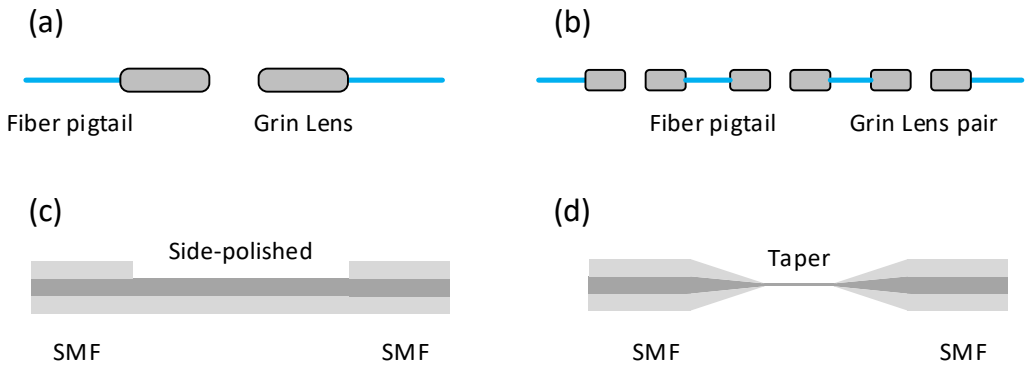

Fig. 1.4 Illustration of (a) Single Grin lens pair with fiber pigtails (b) Cascaded Grin lens pairs (c) Side-polished D-shaped fiber (d) Tapered fiber.

flexible implementation due to the combination with optical fiber working as the light transmission path, they are still not all-fiber spectroscopic method, in which both the sensing element and transmission line should be made up of optical fiber. In addition, stringent alignment of the Grin lens pair is required in those methods. All-fiber direct absorption gas sensor can be realized in D-shaped or tapered fibers [41, 42]. For the D-shaped fiber, one side of the cladding is abraded off, as shown in Fig. 1.4(c). A portion of optical power extends outside the core propagating along the silica-air interface in the form of evanescent field which is then attenuated by trace gas absorption. As most of the light power keeps inside the silica, the effective absorption strength is commonly far less than the free space. To deal with the problem of inefficiency, the D-shape fiber can be replaced with the tapered fiber, whose portion of power in evanescent field can be as large as tens of percent so that the effective strength can be on the same order as the free-space one, as shown in Fig. 1.4(d) [43, 44]. However, due to the difficulties in fabrication and protection, the length of nanofiber is commonly limited to several centimeters and the total absorption length is less than the free-space one.

The invention of hollow-core photonic bandgap (HC-PBG) fiber is a milestone not only in fiber optics but also in spectroscopy [45].The strong confinement for the propagating light beam in the

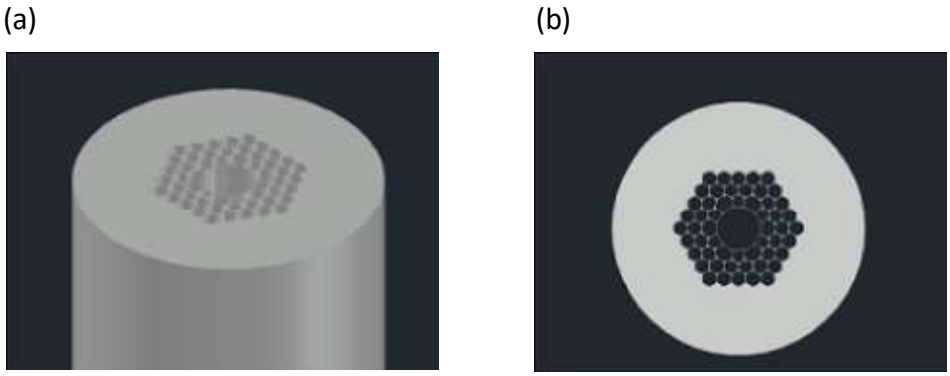

Fig. 1.5 Illustration of the structure of HC-PBG fiber with (a) Top view (b) cross section.

central hole remarkably increases the effective interaction strength of light and gas molecules, as shown in Fig. 1.5. Besides the extraordinary achievements brought by this novel hollow-core optical fiber in areas such as supercontinuum generation [46, 47], ultraviolet generation [48, 49], pulse compression [50, 51], frequency comb generation [52, 53] and high-power delivery [54, 55], it also offers new opportunities for fiber-optic spectroscopic trace gas sensing as it could naturally act as a gas cell with long light-matter interaction path and compact size [56]. Direct absorption spectroscopy [57], spontaneous Raman spectroscopy [58-60], photothermal spectroscopy [33, 61-63] and stimulated Raman spectroscopy [64-66] based on this novel platform have been reported with the straightforward enhancement in the signal amplitude due to the longer interaction length. However, an obvious drawback of trace gas sensing by the HC-PBG fiber is the difficulty in diffusion into the central hole for the gas molecules. Both the methods of cascaded connection for sections of HC-PBG fiber by butt coupling and side-hole drilling by femtosecond laser have been

put forward to deal with this problem, but with the second method being preferred due to the much less propagation loss introduced. Compared with the meticulous attempts in solving the problem of long response time for HC-PBG fiber, the nanofiber based spectroscopic gas detection is inherently free from this issue due to its exposed evanescent field ready for convenient light-matter interaction.

Tapering the commercially available optical fiber so that the propagating optical field previously

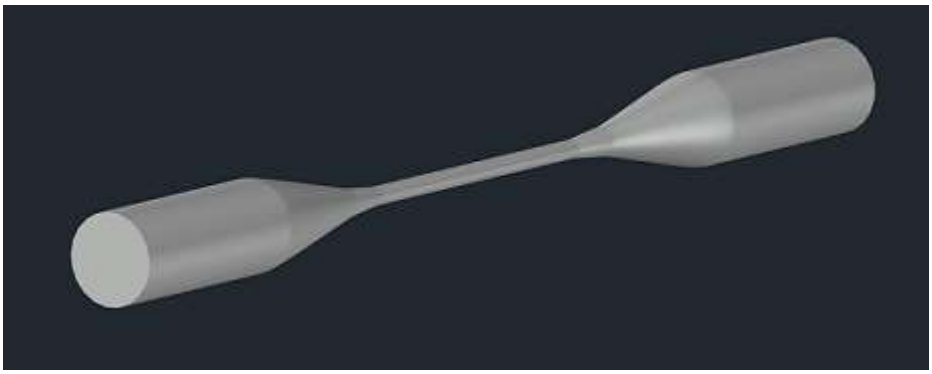

Fig. 1.6 The typical structure of a piece of fiber taper.

constrained inside the core can extend out into the cladding and even into the air to couple with another piece of fiber taper is a quite basic technique for the fabrication of the widely used fiber-optic components such as coupler and mode splitter [67-69]. However, it was not until the year 2003 that the low-loss sub-wavelength optical nanofibers were first fabricated [70]. Although it is later demonstrated that this first method was not only cumbersome but also incomplete, its ground breaking success is, nevertheless, sufficient to ignite the research interest in nanofiber [71-73]. The typical structure of a piece of fiber taper is depicted in Fig. 1.6, where the thinner waist is the zone of nanofiber. The most straightforward advantage of the optical nanofiber is the strong confinement of the optical field, which results in orders of improvement in the light intensity under the same input power level [74]. Another benefit inherently offered by the nanofiber is the flexibility in choosing its diameter by which the total dispersion can be tailored with large degree of freedom [75, 76]. These two advantages appeals well to the nonlinear optics and results in high-performance nanofiber based supercontinuum generation [77-79], pulse compression [80, 81] and third-harmonic generation [82-84].

On the other hand, due to the exposed strong evanescent field, convenient and enhanced light-matter interaction can be achieved on this new platform. There have been a large quantity of elaborate experiments using the evanescent field associated with the nanofiber to trap molecules or to manipulate nano-particles [85]. In the molecule trapping experiments, two beams of light with their wavelengths respectively red and blue detuned relative to the line central of the atomic absorption, are launched from the two ends of the nanofiber pigtail to establish standing fields for both of the two light beams. Due to the attractive and repulsive dipole force exerted by the evanescent field of the red and blue detuned light beams, the atoms will be trapped at a spot near the nanofiber, where the two anti-parallel force cancel each other and create a minimum potential well as the result of the different decay length of the evanescent field of the two light beams used for trapping [86, 87]. The molecular trapping on the nanofiber platform should be a hybridization between the quantum optics and fiber-optics and may find its application in quantum communication in the future. Apart from the manipulation on the molecular level, the nanofiber can also be used to control particles with the

size up to micrometers. The particles can be either trapped around the nanofiber due to the optical gradient force or propelled forward along the surface of nanofiber. This type of manipulation is totally based on the principle of optical tweezers, in which the conservation of transverse momentum for the refracted photons will push the particle towards the position with higher light intensity [88]. While for the propelling manipulation, it results from the transfer of longitudinal momentum from the forward propagating photons to the particles.

Taking advantage of the easy access to the exposed evanescent optical field, nanofibers are also widely used for substance sensing, including but not limited to the detection of humidity [89], salinity [90], DNA strands [91] and gas molecules [92]. The sensing principles can be categorized into either the adsorption induced absorbance or refractive index change. However, as the nanofiber is primitively made of silica which is not an active material that can readily interact with the sensing substance, post processing or functionalization to the nanofiber are generally needed. The surface of the nanofiber can be modified by various coating materials, such as polymers [91], graphene [92], gelatin [89] or even metallic films [93], to make it possible for the various substances to interact with the nanofiber and modulate the propagating light beam. However, the coatings may not exclusively interact only with the substance to be measured, which results in the widely existed problem of cross-sensitivity and makes the nanofiber-based substance sensing barely satisfactory with no exception for the functionalized nanofiber for trace gas molecules detection presently.

1.2 Motivation of this work:

Fast, sensitive and selective detection of trace molecules is very important. Nanofiber based laser spectroscopy method may simultaneously satisfy these three requirements. The exposed evanescent field makes it convenient for light-matter interaction, so it is inherently of fast response. In addition, the spectroscopic nature, in which the molecular transition lines are unique for different species, makes it highly selective. However, the nanofiber based spectroscopic gas detection is rarely researched. The research interest may be discouraged by the preconception that the optical path in

nanofiber cases are quite limited. However, if there exist mechanisms by which the light-matter interaction strength in unit length can be enhanced compared with the free-space or HC-PBG fiber cases, the limited length of optical path in nanofiber will not be as serious as its first sight. The motivation of this work is to reveal and demonstrate that there do exist mechanisms to achieve enhanced sensitivity in nanofiber based laser spectroscopy for the light-absorbing or Raman-scattering molecules.

In the first part, we investigate the nanofiber enhanced photothermal spectroscopy. In both of the traditional free space and the newly developed HC-PBG fiber setup, the photothermal signal originates from the thermo-optic effect of the air, which has relatively low thermo-optic coefficient. While in the case of nanofiber, the light beam is guided along the silica core, whose thermo-optic coefficient is about one order larger than the air, resulting in much higher photothermal efficiency under the same temperature modulation level. The introduction of the material property into the photothermal spectroscopy to improve the phase modulation amplitude should be an interesting research direction and could achieve high sensitivity in trace gas detection.

In the second part, we investigate the nanofiber enhanced stimulated Raman spectroscopy for the Raman active molecules, especially for the homonuclear diatomic molecules such as hydrogen which do not have strong absorption lines in the near infrared band. Due to the relatively small scattering cross section of the molecules, the fiber-optic Raman spectroscopy are mainly preformed in HC-PBG fiber which can confine both the optical field and the molecules in its central hole with long interaction length. However, the Raman scattering efficiency can be greatly enhanced in nanofiber by virtue of the tightly focused mode field and thus high intensity of the evanescent wave. The high SRS efficiency of nanofiber makes it possible to achieve lower detection limit even with a short piece of nanofiber.

In the third part, we step forward to reveal the more subtle problem of the line broadening effect in nanofiber based laser spectroscopy. As the mode field of the nanofiber is tightly confined, the interaction time between the randomly moving gas molecules and the evanescent field should be

relatively short compared with traditional free-space and HC-PBG fiber-based spectroscopy. The additional line broadening phenomenon in nanofiber originating from the limited interaction time is called as the transit time effect and will be investigated both numerically and experimentally.

The high-performance laser spectroscopy based on nanofiber originates from its high efficiency for light matter interaction, so enhanced physical change is achieved even with low concentration of target gas molecules. Those physical changes are expected to be remarkable if the concentration of trace molecules are greatly increased, which makes the nanofiber a promising platform for all optical light manipulation. A interesting phenomenon of transient birefringence in nanofiber induced by photothermal dynamics is observed and investigated, based on which a potential application of all-optical polarization switching is proposed.

1.3 Thesis outline:

Chapter1 reviews the common techniques of infrared laser spectroscopy and the development of fiber-optic based spectroscopic trace gas sensing. It is demonstrated that the recently developed novel optical fibers, including the HC-PBG fiber and nanofiber, offer the new opportunities for spectroscopic gas sensing. The brief introduction of the nanofiber and its promising application in trace gas sensing is presented, as well as the motivation of this work.

Chapter 2 introduces the fundamentals of molecular spectroscopy and the techniques of the spectroscopic gas detection. The basic theory of optical nanofiber is also presented. The concepts and principles presented in this chapter work as the basis of the following chapters.

Chapter 3 describes the nanofiber enhanced photothermal spectroscopy. The mechanisms of the enhanced photothermal phase modulation amplitude in nanofiber is explained. The enhancement effect is supported by the result of numerical simulations and is further verified by the experiments. High-sensitivity trace acetylene detection is experimentally demonstrated. Much higher photothermal signal is anticipated in nanofiber/waveguides made of materials with higher thermo-

optic or thermal expansion coefficients, as supported by the simulations.

Chapter 4 presents the nanofiber enhanced stimulated Raman scattering for highly sensitive trace hydrogen detection. The mechanism of the enhanced SRS efficiency mediated by nanofiber is described. Experiments of trace hydrogen detection is demonstrated with high sensitivity as well as fast response. The experimentally observed polarization dependent SRS gain is explored. The problem of polarization drift and the potential solutions are discussed.

Chapter 5 studies the line broadening factors, especially the transit time broadening, in nanofiber based spectroscopy. A description of the transit time effect based on the classical oscillator model is first presented. The more general density matrix method is then adopted to systematically study the transit time effect associated with the nanofiber. The theory is verified by experiments of nanofiber based absorption spectroscopy for acetylene.

Chapter 6 studies the phenomenon of transient birefringence induced by dynamic photothermal effect in a nanofiber. The numerical simulations explain the origin of this phenomenon. The implementation of a polarization switch based on this transient birefringence effect is demonstrated.

Chapter 7 summarizes the works presented in this thesis and states the possible future works along this direction.

Chapter 2 Background knowledge

In this chapter, the fundamentals of molecular spectroscopy will be introduced. The molecules are treated quantum mechanically with discrete energy eigenstates. Transition happens when the frequency of incident light matches the differential energy between the lower and upper levels as long as the selection rules are satisfied. For the infrared absorption spectroscopy, it is the ro-vibrational transition that is of most concern. Due to the molecular random thermal motion, collisions and the naturally limited lifetime of the energy levels, the transition lines are inevitably broadened, which reduces the peak absorbance of the molecules. The methods in modulation spectroscopy can reduce the noise level and thus improve the signal-to-noise ratio for trace molecule detection. The basic properties of optical nanofiber will also be introduced.

2.1 Energy levels of molecules

2.1.1 Molecular Hamiltonian

A molecule is a multi-body system made up of nuclei and electrons, with the equation of motion for the whole system governed by the time-dependent Schrodinger equation [94], as:

$$i\hbar\frac{d}{dt}|\Psi(t)\rangle = \left(\widehat{H}_0 + \widehat{H}'\right)|\Psi(t)\rangle, \qquad (2.1)$$

where, $|\Psi\rangle$ is the quantum state which contains all the information that we can retrieve from the molecule, $\widehat{H}_0$ is the Hamiltonian for the unperturbed molecular system which is independent of time and $\widehat{H}'$ is the external perturbation. When the total Hamiltonian is independent of time, the time part of the wave function can be separated out as a factor of $e^{-iE\hbar^{-1}t}$, leaving the remaining part of the wave function an eigenfunction of the Hamiltonian operator with eigenvalue of E, as:

$$\widehat{H}\Psi\left(\vec{r}, \vec{s}\right) = E\Psi\left(\vec{r}, \vec{s}\right), \qquad (2.2)$$

where the wave function only contains the spatial $\vec{r}$ and spin $\vec{s}$ variables. Apart from the classic kinetic and coulombic potential contribution to the full Hamiltonian operator, there are also additional energy terms that originate from the intrinsic spin magnetic moment of both the electrons and nucleus and give rise to the spin-orbit coupling, spin-spin coupling, spin-rotation coupling and et al. Not only will those spin-originated terms remove the degeneracy for the energy eigenstates to a certain degree and thus introduce much more abundant and complex spectra lines, but also make the precise computation of the line position in the spectrum quite heavy. However, as the contribution from those terms are comparatively small, we may just neglect them in the molecular Hamiltonian and keep track of the dominant parts. Then there is the so-called non-relativistic Hamiltonian [95], as:

$$\hat{H} = -\frac{\hbar^2}{2m_e}\sum_i \nabla_{r_i}^2 - \frac{\hbar^2}{2}\sum_i \frac{1}{M_i}\nabla_{R_i}^2 - \sum_i\sum_j \frac{Z_i e^2}{4\pi\epsilon_0|R_i - r_j|} + \frac{1}{2}\sum_i\sum_{i\neq j}\frac{e^2}{4\pi\epsilon_0|r_i - r_j|}$$

$$+\frac{1}{2}\sum_i\sum_{i\neq j}\frac{Z_i Z_j e^2}{4\pi\epsilon_0|R_i - R_j|}, \qquad (2.3)$$

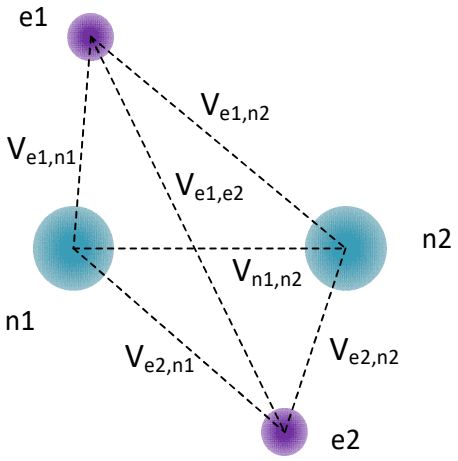

Fig. 2.1 The coulombic potential among the electrons and nuclei (only two electrons and nuclei are depicted for demonstration).

where, $\hbar$ is the reduced Planck constant, m_e and e are the mass and charge of electron, r_i is the space coordinate of the i-th electron, M_i, R_i and Z_i are the mass, space coordinate and charge of the i-th nucleus, ϵ_0 is the vacuum permittivity. The first two terms are kinetic energy for the electron and the nucleus respectively, the third term is the coulombic attraction potential between the oppositely charged electron and nucleus, the last two terms are the coulombic repulsion potential among the electrons and the nucleus respectively. For the convenience of writing, these five terms can be denoted as $\hat{T}_e$, $\hat{T}_n$, $\hat{V}_{en}$, $\hat{V}_{ee}$ and $\hat{V}_{nn}$, in sequence. Depicted in Fig. 2.1 are the coulombic potential among the electron and nucleus where the two purple and cyan circles represents electrons and nucleus respectively, the $V_{a,b}$ represents the coulombic potential between particle a and b.

Although the energy contribution from the spin coupling part is neglected in the Hamiltonian, its effect on the wave function cannot be omitted so the complete wave function should still have four coordinates, three for the spatial distribution and one for the spin. The wave function for the fermion, such as electron and hydrogen nucleus (the proton) should be anti-symmetric upon interchange, while for the boson, such as the oxygen nucleus, it should be symmetric upon interchange. The molecular Hamiltonian do not operate on the spin coordinate and thus the energy of the eigenstates are influenced by the spin part, but the requirement from the spin factor on the eligible wave function does have a fundamental impact on the molecular spectrum. On the other hand, the additional degeneracy introduced by the spin factor determines the distribution of a cluster of molecules among each energy states. However, we may still neglect the spin factor here, as it is unreasonable to talk about statistics for a single molecule. Hiding the spin coordinate but still abiding by the symmetry requirement with it, the wave function will only have the spatial part explicitly. Then the time-independent Schrodinger equation is expressed as:

$$\hat{H}\Psi(\vec{r}_i, \vec{R}_i) = E\Psi(\vec{r}_i, \vec{R}_i), \qquad (2.4)$$

where the $\vec{r}_i$ and $\vec{R}_i$ represent the spatial coordinates for all the electrons and nuclei, respectively, with three coordinates required for each one.

2.1.2 Born-Oppenheimer approximation

Although much simplification has been done by neglecting the spin factor, it is still nearly impossible to directly solve the coupled spatial part. Fortunately, due to the large difference in mass between the electron and the nucleus, the time scale of motion for the electron is much less than the nucleus. For any change in the nuclear position, the electron can response fast and adjust their distribution to seek the minimum energy for the instant nuclear framework. Then the wave function can be separated into the nuclear and electronic parts, with the coordinates of nucleus being a parameter for the later one. This separated treatment for the total wave function is known as Born-Oppenheimer Approximation [24], under which, the Schrodinger equation and wave function can be separated into electronic and nuclear parts, as:

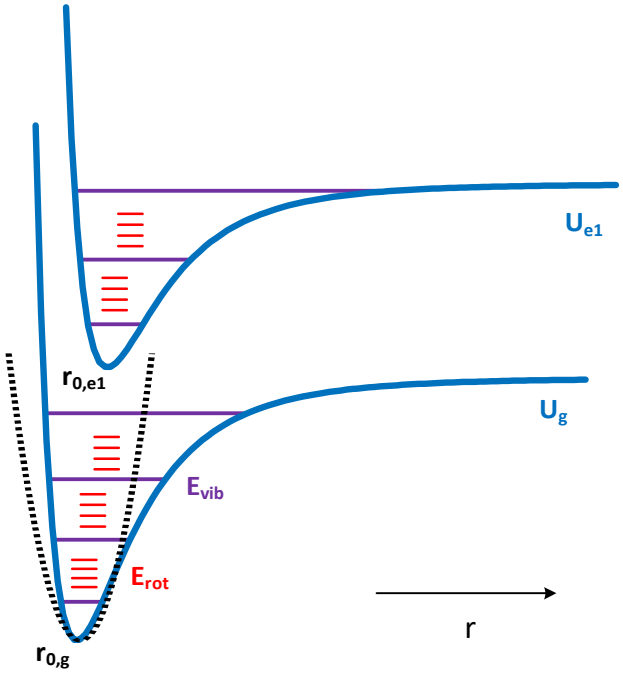

Fig. 2.2 A typical diagram for the molecular energy levels. The black dotted line is a quadratic fitting of the potential curve.

$$\begin{matrix}\hat{H} = \hat{H}_e + \hat{H}_n \\ \Psi(\vec{r}_i, \vec{R}_i) = \Psi_e(\vec{r}_i; \vec{R}_i)\Psi_n(\vec{R}_i)\end{matrix}, \quad with \begin{cases} \hat{H}_e = \hat{T}_e + \hat{V}_{en} + \hat{V}_{ee} \\ \hat{H}_n = \hat{T}_n + U(\vec{R}_i) = \hat{T}_n + \hat{V}_{nn} + E_e(\vec{R}_i) \end{cases}, \tag{2.5}$$

where, the electronic wave function, as well as the electronic energy depends parametrically on the coordinate of the nucleus. As the $\hat{H}_n$ contains the potential energy U, which depends on the $E_e(\vec{R}_i)$ meanwhile, the electronic wave function with a series value of $\vec{R}_i$ as the parameter needs to be solved to get the $E_e(\vec{R}_i)$, so that the potential energy curve $U(\vec{R}_i)$, which is the summation of $\hat{V}_{nn}$ and $E_e(\vec{R}_i)$, can be obtained to construct the $\hat{H}_n$. It should be mentioned that there are always a bunch of potential energy curves $U(\vec{R}_i)$, each of which corresponds to a certain electronic configuration. However, for the infrared laser spectroscopy, due to the relatively small energy of the photons, the transition generally happens between the vibration/rotation energy levels with the same electronic configuration, which is the ground one for almost all the cases. A typical potential curve for a diatomic molecule is plotted in Fig. 2.2. As shown in Fig. 2.2, U_g and U_{e1} are the potential curves for the ground and the first excited electronic states with their minimum energy points $r_{0,g}$ and $r_{0,e1}$, which are the equilibrium distance between the nuclei, not necessarily the same. E_{vib}

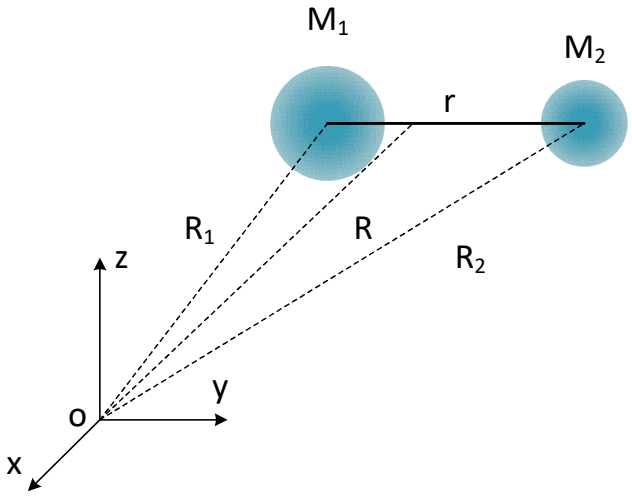

Fig. 2.3 Coordinate transformation from the absolute coordinate system $(\vec{R}_1, \vec{R}_2)$ to the center of mass internal coordinate system $(\vec{R}, \vec{r})$.

and E_{rot} represent respectively the energy levels of vibrational and rotational eigenstates. The black dotted line represents a parabolic fitting for the real potential. For the nuclear wave function, it can be further factorized into three basically independent modes of motion as the vibrational, rotational and translational parts [96]:

$$\Psi_n(\vec{R}_i) = \psi_{tr}\psi_{rv} = \psi_{tr}\psi_{vib}\psi_{rot}, \qquad (2.6)$$

For a N-nucleus molecule, there are totally $3N$ degree of freedom, with three for the translational motion, two or three for the rotational motional depending on whether the molecule is linear or not and the remaining allocated to the vibrational motion. Each degree of freedom corresponds to one quantum number. For demonstration of the principle, it is better to start from the simplest diatomic molecule as depicted in Fig. 2.3, whose nuclear Hamiltonian is then:

$$\hat{H}_n = -\frac{\hbar^2}{2M_1}\nabla_{\vec{R}_1}^2 - \frac{\hbar^2}{2M_2}\nabla_{\vec{R}_2}^2 + U(|\vec{R}_2 - \vec{R}_1|), \qquad (2.7)$$

By the substitution of absolute coordinates $\vec{R}_1$ and $\vec{R}_2$ with the internal coordinates $\vec{r} = \vec{R}_2 - \vec{R}_1$ and the coordiante of center of mass $\vec{R} = (M_1 + M_2)^{-1} \cdot (M_1\vec{R}_1 + M_2\vec{R}_2)$, the nuclear Hamiltonian is transformed into:

$$\hat{H}_n = -\frac{\hbar^2}{2M_t}\nabla_{\vec{R}}^2 - \frac{\hbar^2}{2\mu}\nabla_{\vec{r}}^2 + U(r), \qquad (2.8)$$

where, the $M_t = M_1 + M_2$ is the total molecular mass and $\mu = M_1M_2(M_1 + M_2)^{-1}$ is the reduced mass. As there is no coupling between the $\vec{R}$ and $\vec{r}$, the external (translational) and internal (ro-vibrational) part of the nuclear wave function can be separated as:

$$\begin{aligned}\hat{H}_n\psi_{tr}(\vec{R})\psi_{rv}(\vec{r}) &= \left[-\frac{\hbar^2}{2M_t}\nabla_{\vec{R}}^2 - \frac{\hbar^2}{2\mu}\nabla_{\vec{r}}^2 + U(r)\right]\psi_{tr}(\vec{R})\psi_{rv}(\vec{r}) \\ &= (E_{tr} + E_{rv})\psi_{tr}(\vec{R})\psi_{rv}(\vec{r}), \qquad (2.9)\end{aligned}$$

where, the translational energy E_{tr} and internal energy E_{int} are the eigenvalues of the separated

Schrodinger equations for ψ_{tr} and ψ_{rv}, respectively:

$$\begin{matrix} -\frac{\hbar^2}{2M_t}\nabla_{\vec{R}}^2\psi_{tr}(\vec{R}) = E_{tr}\psi_{tr}(\vec{R}) \\ \left[-\frac{\hbar^2}{2\mu}\nabla_r^2 + U(r)\right]\psi_{rv}(\vec{r}) = E_{rv}\psi_{rv}(\vec{r}) \end{matrix}, \qquad (2.10)$$

For the translational part, the Schrodinger equation is simply for the case of particle in box, in which the $\vec{R}$ containes three spatial coordinates (x, y, z) representing the position for the center of mass of the moleucle. In the translational Schrodinger equation, it is assumed that the molecule do not experience position-dependent external force, which is reasonable for the electrically neutral single molecule in dilute limit. The translational wave function can be further factorized based on the three independent spatial coordinates as $\psi_{tr}(\vec{R}) = \psi_{tr}(x)\psi_{tr}(y)\psi_{tr}(z)$, And the boundary condition force the E_{tr} to be quantized with the final result turning out to be:

$$\widehat{H}_{tr}\psi_{tr} = E_{tr}\psi_{tr},\ with \begin{cases} \psi_{tr} = sin\left(\frac{2\pi n_1 x}{L_x}\right)sin\left(\frac{2\pi n_2 y}{L_y}\right)sin\left(\frac{2\pi n_3 z}{L_z}\right) \\ E_{tr} = \frac{h^2}{8M_t V^{\frac{2}{3}}}(n_1^2 + n_2^2 + n_2^2) \end{cases}, \qquad (2.11)$$

where, V is the volumn of gas container and n_i are the translational quantum numbers. Considering the extremely small value of the square of the Planck constant in the front coefficient, the energy gaps between each translational energy levels will be too tiny to be sensible in common situations, making the quantum mechanical treatment not necessary for the translational part.

2.1.3. Ro-vibrational energy modes

Then we try to separate the remaining part of the nuclear wave function into the rotational and vibrational parts. It is much more convenient to work with spherical coordinate system rather than the Cartesian one for the internal part of the two-particle system. Recalling the lower one in Equ.(2.12) and expressing it in the spherical coordinate, we get:

$$\left[-\frac{\hbar^2}{2\mu}\left[\frac{d}{dr}\left(r^2\frac{d}{dr}\right)+\frac{1}{sin\theta}\frac{\partial}{\partial\theta}\left(sin\theta\frac{\partial}{\partial\theta}\right)+\frac{1}{sin^2\theta}\frac{\partial^2}{\partial\varphi^2}\right]+r^2U(r)\right]\psi_{rv}(r,\theta,\varphi)$$
$$=r^2E_{rv}\psi_{rv}(r,\theta,\varphi), \qquad (2.12)$$

The potential term solely depends on the r and thus is spherically symmetric. Reforming the above equation, so that the radial and azimuthal dependent operators are put at the opposite sides of the equation. Then the cultivated method would be assuming the $\psi_{rv}(r,\theta,\varphi)$ separable into its radial and azimuthal parts as $\psi_{rv}(r,\theta,\varphi)=R(r)Y(\theta,\varphi)$. Following the method of separation of variables, the above equation is reformed as:

$$\begin{matrix}\left[-\frac{\hbar^2}{2\mu}\frac{1}{r^2}\frac{d}{dr}\left(r^2\frac{d}{dr}\right)+[U(r)+r^{-2}\lambda]\right]R(r)=E_{rv}R(r)\\ \frac{\hbar^2}{2\mu}\left[\frac{1}{sin\theta}\frac{\partial}{\partial\theta}\left(sin\theta\frac{\partial}{\partial\theta}\right)+\frac{1}{sin^2\theta}\frac{\partial^2}{\partial\varphi^2}\right]Y(\theta,\varphi)=-\lambda Y(\theta,\varphi)\end{matrix}, \qquad (2.13)$$

where the λ is a constant. The operator before the azimuthal wave function turns out to be nothing but just the $-(2\mu)^{-1}\hat{L}^2$, where the $\hat{L}$ is the orbital angular momentum operator. The eigenfunctions for the $\hat{L}^2$ are simply the spherical harmonics $Y_J^M(\theta,\varphi)$ with eigenvalues of $J(J+1)\hbar^2$, where J is the total rotational quantum number and M is the quantum number for the

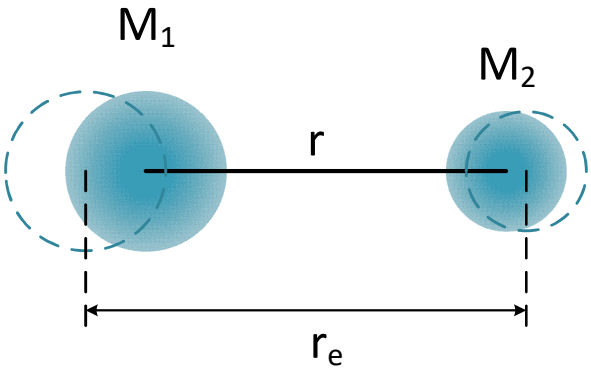

Fig. 2.4 One dimensional harmonic oscillator simplification for the vibrational motion of the nucleus around the equilibrium position.

z-directional component. Classically, the rotational energy is related with the angular momentum as $E_{rot} = (2I)^{-1}L^2$, where I is the rotational inertia. According to the correspondence principle, the rotational Hamiltonian for a molecule still has the form as $\widehat{H}_{rot} = (2I)^{-1}\hat{L}^2$, with $I = \mu r^2$ for the diatomic molecules. Then the lower one in Equ.(2.13) can be directly related with the rotational eigenstates as:

$$\widehat{H}_{rot}\psi_{rot} = E_{rot}\psi_{rot},\ with \begin{cases} \psi_{rot}(\theta,\varphi) = Y_J^M(\theta,\varphi) \\ E_{rot} = \dfrac{J(J+1)\hbar^2}{2I} = r^{-2}\lambda \end{cases}, \qquad (2.14)$$

The $r^{-2}\lambda$ in the upper one of Equ.(2.13) can be substituted by E_{rot}, which can then be subtracted from E_{rv} with only E_{vib} remained. Assuming a harmonic oscillator potential well $U(r) = 2^{-1}k_e x^2$ as depicted in the dashed parabolic in Fig. 2.2, which fits satisfyingly for the relatively lower vibrational levels where the displacement of the nuclei from the equilibrium position is limited. With variable substitutions of $S(r) = rR(r)$ and $x(r) = r - r_e$, the differential equation for vibrational part is simplified as:

$$\left[-\frac{\hbar^2}{2\mu}\frac{d^2}{dx^2} + 2^{-1}k_e x^2\right]S(x) = E_{vib}S(x), \qquad (2.15)$$

which is well-known as the Schrodinger equation for one dimensional harmonic oscillator, as simplified in Fig. 2.4. Then the eigenfunctions and eigenvalues for the vibrational part of diatomic molecule are:

$$\widehat{H}_{vib}\psi_{vib} = E_{vib}\psi_{vib},\ with \begin{cases} \psi_{vib}(r-r_e) = r^{-1}S_v(r-r_e) = N_v r^{-1}H_v[\alpha(r-r_e)]e^{-\frac{1}{2}\alpha^2(r-r_e)^2} \\ E_{vib} = (v+2^{-1})\mathrm{h}\upsilon_e \end{cases}, (2.16)$$

where, N_v is the normalization coefficient, H_v is the Hermite polynomial, α and υ_e are constants equalling to $\hbar^{-1/2}(2\pi\mu\upsilon_e)^{1/2}$ and $(2\pi)^{-1}k_e^{1/2}\mu^{-1/2}$, respectively.

In summary, the energy modes of the molecule have been separated into the electronic, vibrational,

rotational and translation parts:

$$\begin{gathered}\left(\hat{H}_{ele}+\hat{H}_{vib}+\hat{H}_{rot}+\hat{H}_{tr}\right)\Psi=\left(E_{ele}+E_{vib}+E_{rot}+E_{tr}\right)\Psi \\ \Psi=\psi_{ele}\psi_{vib}\psi_{rot}\psi_{tr}\end{gathered}, \qquad (2.17)$$

Although the illustration of separation of the electronic, vibrational and rotational modes is presented with the example of diatomic molecule, the same ideal is shared for treatment of other molecules. Generally, only the vibrational and rotational modes are involved in the infrared spectroscopy. However, the dependence of the nuclear wave function on the internal potential energy makes the solution of electronic wave function still necessary. For the handling of the vibrational levels in polyatomic molecules, the technique of normal mode analysis can be used for simplification, in which the molecular vibration is decoupled into a set of independent simple harmonic oscillators. It should be mentioned that the quadratic potential in simple harmonic vibration is just a second order approximation for the Morse potential, which is even also an approximation for the real potential. The vibrational anharmonicity will cause inequality in the gap of vibrational levels as well as the overtone transition. For the rotational modes, the rigid-rotor treatment above neglects the rotational centrifugal stretching effects, which increases the bond length as well as the rotational inertia for higher rotational levels and is nonnegligible for more satisfying approximation.

2.2. Light-matter interaction:

2.2.1. Transition dipole

Light is a kind of electromagnetic wave, which is first theorized by Maxwell and then conclusively verified by Hertz. Although the modern quantum theory generalizes the electromagnetic field as photon, the classical theory of electromagnetic wave is enough to describe the absorption of light by molecules. So the description of light-matter interaction here is semi-classical, that is the molecules are treated quantum-mechanically and thus are only allowed to be in the discrete energy levels as demonstrated in the previous section, while the light is treated classically as the oscillating

electric and magnetic field. As the electric dipole transition is the dominant type for light absorption, the perturbation Hamiltonian may just contain this single term as [97]:

$$\widehat{H}' = -\hat{\mu} \cdot 2^{-1}\vec{E}[exp(-i\omega t) + c.c.], \qquad (2.18)$$

where, $\vec{E}$ is the electric field of light which oscillates over time but is assumed to be spatially even on the scale of molecular size, $\hat{\mu} = \sum q_i \vec{r}_i$ is the electric dipole moment operator. Without the external perturbation, the molecule can reside in any eigenmode of the unperturbed Hamiltonian. So the total wave function is a linear combination of all the energy eigenstates as:

$$\Psi = \sum_m C_m|\psi_m\rangle\, exp(-i\omega_m t)\,, \qquad (2.19)$$

where, C_m is the time-independent probability amplitude whose square is the probability that the molecule can be found in the m-th energy eigenstate, ψ_m is the m-th energy eigenfunction and $\omega_m = \hbar^{-1}E_m$. The light field will perturb the probability amplitude, which process is governed by the time-dependent Schrodinger equation as:

$$i\hbar \sum_m |\psi_m\rangle \frac{d}{dt}[C_m(t)\, exp(-i\omega_m t)] = \sum_m C_m(t)\, exp(-i\omega_m t)\left(\widehat{H}_0 + \widehat{H}'\right)|\psi_m\rangle\,, \qquad (2.20)$$

where, $\widehat{H}'$ is given in Equ.(2.20) above. Multiplying $\langle\psi_n|$ each side and taking the orthonormal property of $\langle\psi_n|\psi_m\rangle = \delta_{nm}$, the time derivative for the slow-varying probability amplitude of the n-th level $C_n(t)$ will be:

$$\dot{C}_n(t) = \frac{1}{i\hbar}\sum_m \left[C_m(t)\, exp(i(\omega_n - \omega_m)t) \cdot \langle\psi_n|\widehat{H}'|\psi_m\rangle\right],\ with\ \langle\psi_n|\widehat{H}'|\psi_m\rangle$$
$$= -2^{-1}\vec{E} \cdot \langle\psi_n|\hat{\mu}|\psi_m\rangle[exp(-i\omega t) + c.c.], \qquad (2.21)$$

The probability amplitude $C_n(t)$ can be gotten by time integration from $t_0 = 0$ to t. The transition probability from n-th to m-th level or reversely is found to be proportional to the square of the transition dipole moment $\langle\psi_n|\hat{\mu}|\psi_m\rangle$, which can be denoted as $\vec{\mu}_{nm}$. For the infrared laser

spectroscopy, the transition happens between different ro-vibrational levels with the same electronic states.

2.2.2. Ro-vibrational transition

The pure rotational transition happens mainly in the microwave band, due to the small energy gaps between the rotational eigenstates. It is required that a molecule should have a permanent electric dipole moment for it to be rotational transition active. The general selection rule is:

$$\begin{matrix}\Delta J = J'' - J' = \pm 1 \\ \vec{\mu}_0 \neq 0\end{matrix}, \qquad (2.22)$$

where, the double and single primes represent respectively the upper and lower levels in transition. In infrared laser spectroscopy, the rotational transition is rarely taken but only appears

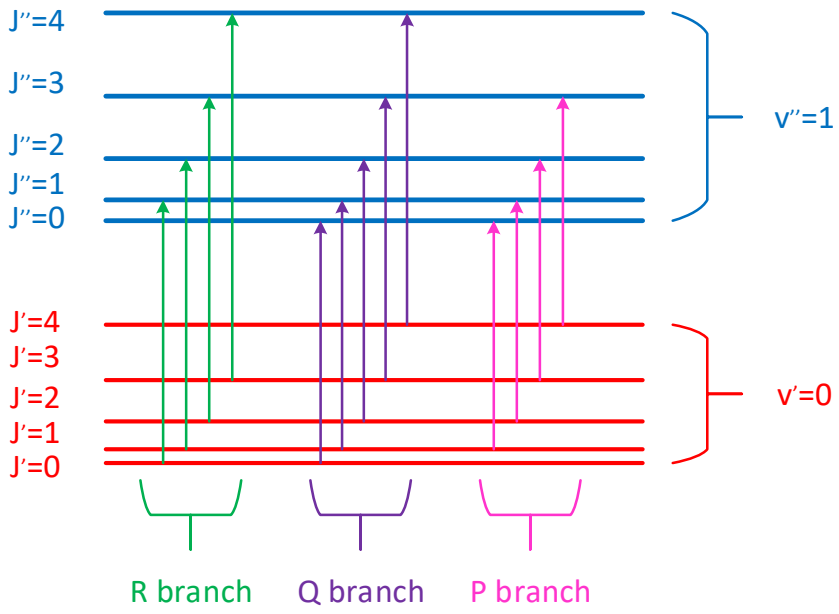

Fig. 2.5 Energy diagram for ro-vibrational transitions. The R-, Q- and P-branch denote the transitions with $\Delta J = 1,\ 0$ and -1, respectively.

accompanying the prevalently adopted vibrational transitions, which requires:

$$\begin{matrix} \Delta v = v'' - v' = \pm 1 \\ \Delta J = J'' - J' = \pm 1 \\ \left(\frac{d\vec{\mu}}{dQ_i}\right)_{Q_i=0} \neq 0 \end{matrix}, \qquad (2.23)$$

where, Q_i is the displacement of nuclei in the normal coordinate. For the ro-vibrational transition to occur, the derivative of the molecular dipole moment with respect to the nuclear motion during vibration should not be zero. Accompanying the vibrational transition, there is also associated change in rotational eigenstates, in which the quantum number of J can either plus or minus one ($\Delta J = 1$ or $\Delta J = -1$), resulting in the so-called R- and P-branch in the spectrum, as shown in Fig. 2.5. The vibrational selection rule of $\Delta v = \pm 1$ is strict only for the simple harmonic oscillator model. Due to the realistic anharmonicity of inter-nucleus potential and the coupling between vibrational modes, overtone and combination band transitions are ubiquitous in infrared

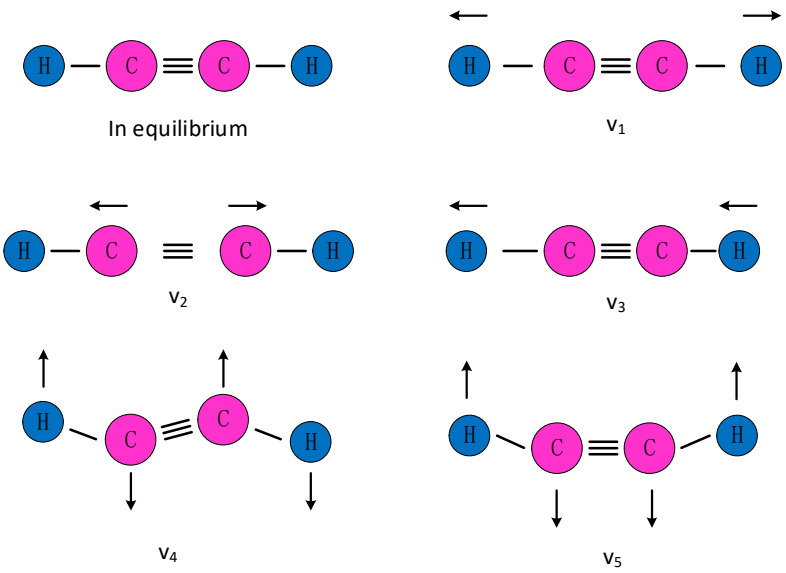

Fig. 2.6 Normal modes of vibration for acetylene. The v_4 and v_5 modes are doubly degenerate, with the molecules in the other two orthogonal modes moving perpendicular to the plane.

spectroscopy. As an example, the strong absorption lines of acetylene at the communication band originates from the $v_1 + v_3$ combination band as shown in Fig. 2.6, where all the five vibrational modes are presented.

The transition lines of $v_1 + v_3$ band of pure acetylene at atmospheric pressure from the wavenumber range of 6460 to 6640 cm^{-1} (corresponding to wavelength range of 1506 to 1548 nm) are plotted in Fig. 2.7. There are two distinct groups of transition lines, one is from the odd rotational level, as already annotated, and the other is from the even rotational levels, whose strength is about one third of the odd groups. This distinction originates from the nuclear spin statistics of the two hydrogen atoms in the acetylene molecule, which requires the total molecular population number among all the odd and even rotational levels to be 3:1 [24].

For homodiatomic molecules, such as hydrogen, neither is there a permanent molecular dipole nor

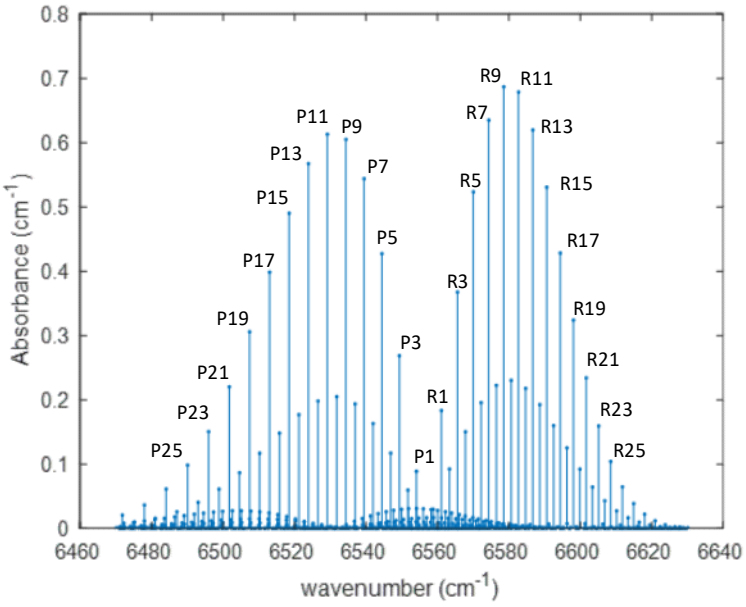

Fig. 2.7 Position of the transition lines and their absorption coefficients of the $v_1 + v_3$ band for pure acetylene at atmospheric pressure in the wavenumber range of 6460 to 6640 cm^{-1}.

a non-zero derivation of the dipole during vibration. Therefore the hydrogen molecule is infrared absorption forbidden. However, there are still the mechanism of scattering for it to interact with light. The distribution of electrons within the molecule will be perturbed by the external electric field, then the molecule is said to be polarized with the generation of an induced electric dipole moment $\vec{\mu}_{ind} = \vec{\alpha} \cdot \vec{E}$, where $\vec{\alpha}$ is the molecular polarizability tensor [98]. In a classical view, this induced electric dipole oscillates with time and thus emits light in a quite similar way as an antenna. While quantum mechanically, the parameter for evaluation of the strength of scattering, just like the transition dipole in absorption process, is the transition polarizability, defined as $\langle \psi_m | \hat{\alpha} | \psi_n \rangle$ and the scattering probability is proportional to the square of it. There are also selection rules for Raman transition. For the pure rotational Raman scattering, it is required that:

$$\Delta J = J'' - J' = \pm 2, \qquad (2.24)$$

where, the transitions with $\Delta J = +2$ and $\Delta J = -2$ are known as the anti-Stokes and Stokes

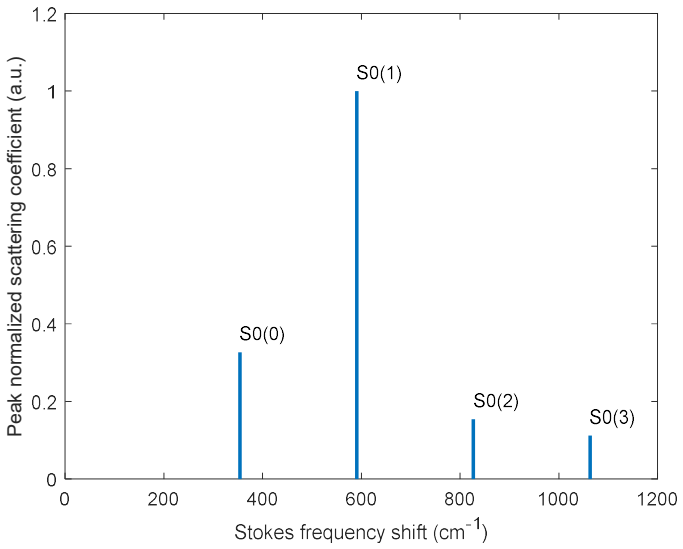

Fig 2.8 Positions and the relative forward scattering coefficient of the Stokes beams generated in pure rotational Raman scattering of hydrogen. The number in the bracket denotes the lower rotational level of transition.

rotational Raman scattering respectively. The energy of rotational levels are proportional to $J(J+1)$ as indicated in Equ. (2.14), so the frequency shift of the Stokes beams from the pump beam is proportional to $4J'+6$. Shown in Fig. 2.8 is the pure rotational Raman transition lines of hydrogen.

For the vibrational Raman transition, apart from the selection rule, there is an additional requirement on a non-vanishing derivative of molecular polarizability during vibration as:

$$\begin{matrix} \Delta v = v'' - v' = \pm 1 \\ \Delta J = J'' - J' = 0, \pm 2 \\ \left(\frac{d\alpha}{dQ_i}\right)_{Q_i=0} \neq 0 \end{matrix}, \qquad (2.25)$$

Different from its counterpart of electric dipole transition, the Raman scattering allows pure vibrational transition with $\Delta J = 0$. It should be mentioned that, if both the Δv and ΔJ are zero, the scattering process can still happen, which is known as the Rayleigh scattering.

2.3. Lineshape and broadening effects

For the absorption spectroscopy, the larger the absorption coefficient $\alpha(\upsilon)$, the larger the signal amplitude, as demonstrated in Equ. (1.2). The amplitude of absorption coefficient depends not only on the transition dipole $\vec{\mu}_{td}$, but also on the lineshape function $f_{shape}(\nu)$ as [97]:

$$\alpha(\nu) \propto g(T)\vec{\mu}_{td}^2 f_{shape}(\nu)N, \qquad (2.26)$$

where, $g(T)$ is the factor accounting for the molecular population among the energy eigenstates and is soly determined by temperature, N is the trace molecular density. The severer the broadening effect, the smaller the amplitude of f_{shape} at the line center ν_0, although the spectral integral over the whole transition line is a constant, i.e., the broader the linewidth, the smaller the peak absorption. Typical broadening effects are natural broadening, collisional broadening, Doppler broadening and the transit time broadening. The last one is usually covered by the Doppler

broadening and only show up in the Doppler-free spectroscopy. However, as will be shown in Chapter 6, its broadening effect can be comparable with the Doppler one in nanofiber case due to its unconventionally narrow mode field.

The natural broadening originates from the limited lifetime of the upper energy level, which through the time-energy uncertainty principle results in a finite width of the transition line. Without intermolecular interactions, the number of molecules decays exponentially from the upper to the lower energy level with the decay constant equal to the spontaneous emission rate A_s. This exponential decay over time results in a Lorentzian lineshape function in spectrum (frequency domain) with the half width half maximum (HWHM) linewidth being $(4\pi)^{-1}A_s$. However, usually the natural linewidth is too thin to be seen in infrared spectrosocpy which is dominated by either the collisional or the Doppler broadening effects in high or low pressure range, respectively.

The interaction between one molecule and the light beam can be perturbed by other molecules in presence. If the light-molecule interaction process is interrupted by the molecular collision, the linewidth will be broadened due to the reduced coherent time. The higher the molecular density, the higher the collisional frequency and thus the severer the broadening effect. In addition, the distance between molecules are decreased with increased molecular density, making the influence of intermolecular potential nonnegligible for the internal energy eigenstates. So the energy gap between the eigenstates will be modified, which results in a shift in transition line. The pure collisional broadening effect is homogeneous (independent of molecular velocity and position) and can be described by a Lorentzian lineshape, just like the natural broadening effect, as:

$$f_{col}(\nu) = \frac{1}{\pi}\frac{\Gamma_{col}}{\Gamma_{col}^2 + (\nu - \nu_0)^2}, \ with\ \Gamma_{col} = \gamma p, \qquad (2.27)$$

where, γ is the collisional broadening coefficient, p is the pressure, Γ_{col} is the HWHM linewidth of the collisional broadening.

In the low pressure range, the collisional broadening effect is suppressed, making the linewidth

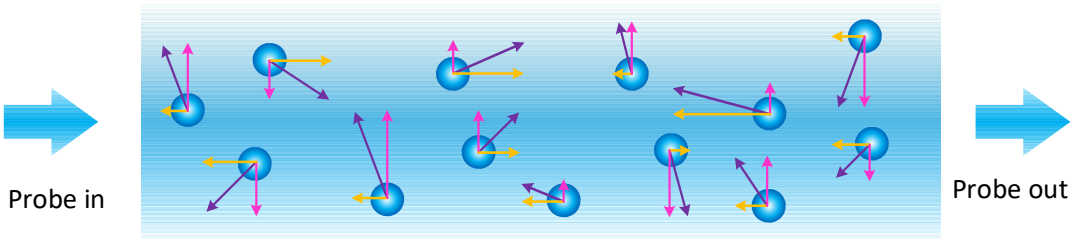

Fig. 2.10 Illustration of the random thermal motion of the gas molecules within the mode field of a light beam. The magenta, yellow and purple represents the transversal, longitudinal and total velocity of the molecule with the length representing the magnitude. The bluish padding represents the intensity distribution for the propagating probe beam.

Doppler-limited, by which molecules with different velocity components along the light beam experience different frequency of absorption. Due to the velocity selectivity, the Doppler broadening is inhomogeneous and follows the one-dimensional Maxwell-Boltzmann distribution as:

$$f_{dop}(\nu) = \left(\frac{ln2}{\pi\Gamma_{dop}^2}\right)^{\frac{1}{2}} exp\left(-(\nu-\nu_0)^2\frac{ln2}{\Gamma_{dop}^2}\right),\ with\ \Gamma_{dop} = \nu_0\left(\frac{2N_A kTln2}{Mc^2}\right)^{\frac{1}{2}}, \qquad (2.28)$$

where, Γ_{dop} is the HWHM linewidth of the Doppler broadening, N_A is the Avogadro constant, k is Boltzmann constant, M is molecular mass. The Voigt lineshape, which is a convolution between the Lorentzian and Gaussian profile, can be used to describe the overall lineshape for the infrared absorption spectroscopy. A comparison between Lorentzian, Gaussian and Voigt lineshape can be seen in Fig. 2.9, where the HWHM linewidth of Lorentzian and Gaussian functions are set equal and the Voigt lineshape is a direct convolution of these two functions.

In nanofiber-based spectroscopy, the transit time broadening may not be omitted which originates from the limited time of the molecule staying within the optical mode field. As shown in Fig. 2.10,

both the Doppler and the transit time broadening effects originate from the random thermal motion of the gas molecule, whose velocity magnitudes (represented as the length of purple arrow) statistically follow the Maxwell-Boltzmann distribution. The longitudinal motion (yellow arrow) of the molecules with different velocity leads to the Doppler broadening, while the transverse motion (magenta arrow) makes the molecule fly through the optical field eventually and thus results in an unavoidably limited interaction time. For a fixed environmental temperature, the molecular velocity follows a constant distribution. So, the narrower the beam diameter, the shorter the light-matter interaction time. For nanofibers, the region of evanescent field is only about one micron wide, which means the interaction time is quite limited in room temperature.

Different from the Doppler broadening, the transit time effect is homogeneous. Although molecules with different transversal velocity has different linewidth, they share the same line center of transition. The faster the transverse velocity of the molecule, the shorter the interaction time with the light beam and thus the severer the transit time broadening. The issue of transit time broadening may become critical in nanofiber-based spectroscopy and will be systematically discussed in Chapter 5.

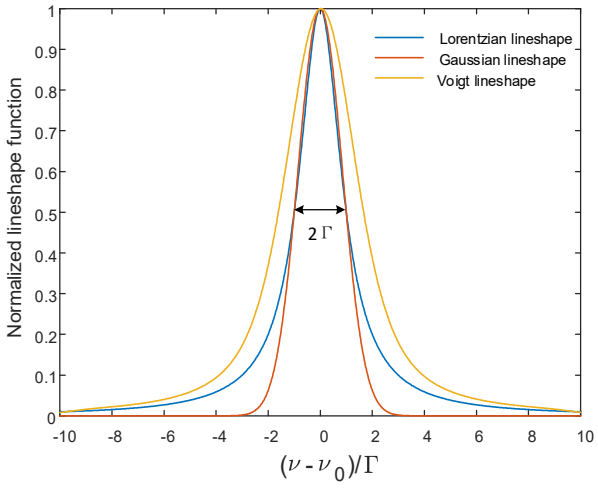

Fig. 2.9 Comparison between the normalized Lorentzian, Gaussian and Voigt lineshape functions.

2.4. Wavelength modulation spectroscopy

In laser spectroscopy, modulation is generally required, which can shift the operating frequency towards a higher-frequency band to achieve lower noise level and thus higher sensitivity. The principle of wavelength modulation spectroscopy (WMS) is that the wavelength of the laser beam is sinusoidally modulated at a high frequency with its central position slowly swept across the absorption line of the molecules. The instant wavelength ν can be expressed as:

$$\nu = \bar{\nu} + m \cdot \Gamma_{lor} \cos(2\pi\nu_m t), \qquad (2.29)$$

where, $\bar{\nu}$ is the central wavelength, which is swept at low rate, m is the modulation depth, Γ_{lor} is the linewidth of Lorentzian lineshape and ν_m is the modulation frequency. Different from the intensity modulation, as it is the lineshape that the WMS method measures, any spectrum independent absorbance will not contribute to the signal [99]. The optimal frequency of wavelength modulation depends on the system response. In photothermal scheme, it should not exceeds the heat generation or thermal relaxation time. The optimal amplitude of wavelength modulation is about 2 times of the linewidth of absorption and for a Lorentzian shape the value equals to 2.2. The detected signal contains a group of harmonics, which makes the lock-in amplifier necessary for discriminating a certain one out. The waveforms of the first four orders of harmonics with different detuning are shown in Fig. 2.11.

Although the first-harmonic has the largest signal amplitude, which is defined as the peak-to-peak value of the waveform, it is quite sensitive to the linear baseline drift, which results in large background signal. Because, mathematically, a linearly increasing curve has a non-zero first-order derivative, but other orders of derivative are vanishing. In addition, all the odd-harmonics have their maximum signal position away from the center of absorption line, which is undesirable [100]. So, commonly, the second-harmonic is preferred in WMS. To obtain the full WMS waveform, the central wavelength needs to sweep across the whole transition line. It should be mentioned that WMS method is not always the first choice in improving the signal-to-noise ratio. Compared with

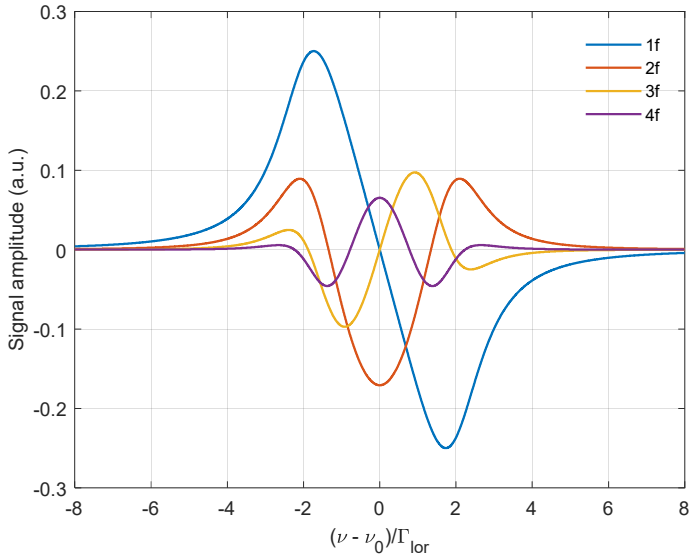

Fig. 2.11 First four orders of harmonics of Lorentzian lineshape with the same modulation depth of $m = 2$.

the intensity modulation, it is quite inconvenient for the WMS method to recover the real lineshape. So, the WMS method is generally adopted in cases of high-performance trace gas sensing but is not suitable for investigation of the details of spectrum, such as molecular lineshape measurement.

2.5. Optical nanofiber

A variety of methods have been used to fabricate the optical nanofiber, but all of them are based on the same principle of heating and tapering [73]. The taper-drawn nanofiber consists of three parts, i.e., two SMF pigtails, two transition regions and a waist with a sub-wavelength diameter as shown in Fig. 2.12. For low loss transmission, the transition region should be as smooth as possible so that no radiation mode is excited (the so-called adiabatic condition). The calculation of mode field for nanofiber has been well established. The nanofiber can only support one propagating mode, i.e., the fundamental HE_{11} mode, when the V-number satisfies [74]:

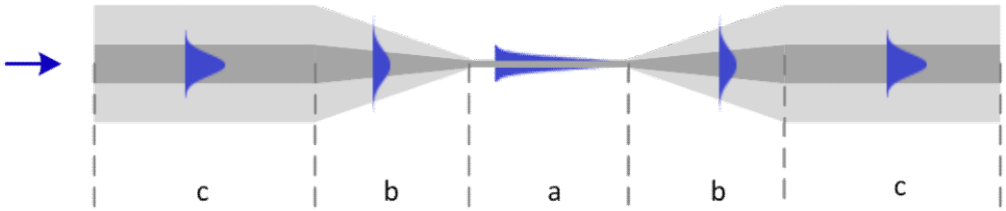

Fig. 2.12 A typical geometric structure of an optical nanofiber. The segment *a* is the waist zone for light-matter interaction, segment *b* is the transition region for low loss mode conversion and segment *c* is the SMF pigtail for optical connection.

$$V = k\rho\sqrt{n_1^2 + n_2^2} < V_c = 2.405, \qquad (2.30)$$

where, $k = 2\pi\lambda_0^{-1}$ is the wavenumber of the light beam in vacuum, ρ is the radius of nanofiber, n_1 and n_2 are the refractive index of silica core and air cladding respectively, V_c is the cut-off V-number. For incident light beam with wavelength of 1550 nm, the silica nanofiber will be single-mode when its diameter is less than about 1140 nm. The propagating constant β can be calculated from the eigenfunction as:

$$\frac{J_0(h\rho)}{haJ_1(h\rho)} = -\frac{n_1^2 + n_2^2}{2n_1^2}\frac{K_1'(q\rho)}{qaK_1(q\rho)} + \frac{1}{(h\rho)^2} - \sqrt{\left(\frac{n_1^2 - n_2^2}{2n_1^2}\frac{K_1'(q\rho)}{q\rho K_1(q\rho)}\right)^2 + \frac{\beta^2}{n_1^2k^2}\left(\frac{1}{(h\rho)^2} + \frac{1}{(q\rho)^2}\right)^2}, \qquad (2.31)$$

where, $h = (n_1^2k^2 - \beta^2)^{1/2}$ and $q = (\beta^2 - n_2^2k^2)^{1/2}$, The J_n and K_n are respectively the Bessel functions of first kind and the modified Bessel functions of second kind. Commonly, it is the electric field rather than the magnetic field in the light beam that interacts most strongly with the molecules. So , we may hereby just focus on the electric one. The x-, y- and z-directional components of the electric field inside the nanofiber ($r < \rho$) are given by:

$$E_x = -i\frac{\beta}{2\mathrm{h}}[(1-s)J_0(\mathrm{hr})\cos\varphi_0 - (1+s)J_2(\mathrm{hr})\cos(2\varphi-\varphi_0)]$$
$$E_y = -i\frac{\beta}{2\mathrm{h}}[(1-s)J_0(\mathrm{hr})\sin\varphi_0 - (1+s)J_2(\mathrm{hr})\sin(2\varphi-\varphi_0)]' \qquad (2.32)$$
$$E_z = J_1(\mathrm{hr})\cos(\varphi-\varphi_0)$$

For the evanescent field ($r > \rho$), the three components of electric field are given by:

$$E_x = -i\frac{\beta}{2q}\frac{J_1(\mathrm{h}\rho)}{K_1(q\rho)}[(1-s)K_0(qr)\cos\varphi_0 - (1+s)K_2(qr)\cos(2\varphi-\varphi_0)]$$
$$E_y = -i\frac{\beta}{2q}\frac{J_1(\mathrm{h}\rho)}{K_1(q\rho)}[(1-s)K_0(qr)\sin\varphi_0 - (1+s)K_2(qr)\sin(2\varphi-\varphi_0)], \qquad (2.33)$$
$$E_z = \frac{J_1(\mathrm{h}\rho)}{K_1(q\rho)}K_1(qr)\cos(\varphi-\varphi_0)$$

where, φ_0 is the azimuthal angle of the polarization and the parameter of s is give as:

$$s = \left[\frac{1}{(q\rho)^2} + \frac{1}{(\mathrm{h}\rho)^2}\right]\cdot\left[\frac{J_1'(\mathrm{h}\rho)}{\mathrm{h}\rho J_1(\mathrm{h}\rho)} + \frac{K_1'(q\rho)}{q\rho K_1(q\rho)}\right]^{-1}, \qquad (2.34)$$

For absorption spectroscopy as well as molecular trapping, the light-matter interaction strength is

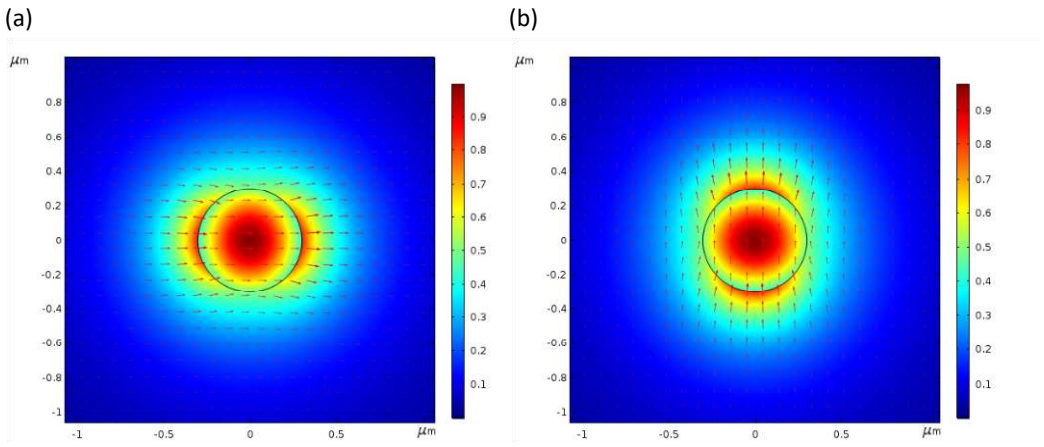

Fig. 2.13 The peak normalized z-directional Poynting vector (color surface) and transverse electric field (red arrows) of the fundamental modes (a) HE_{11}^{x} and (b) HE_{11}^{y} for light beam with wavelength of 1550 nm propagating along a 600-nm-diameter silica nanofiber.

determined by the evanescent field that extends outside the nanofiber. For a linearly polarized incident light beam with wavelength of 1550 nm along a 600-nm-diameter silica nanofiber, the z-directional Poynting vector (energy flux) as well as the transverse electric fields of the two fundamental modes HE_{11}^{x} and HE_{11}^{y} are shown in Fig. 2.13.

For light-matter interaction on the nanofiber platform, the larger the portion of evanescent field, the better the interaction efficiency. Thinner diameter appeals to more evanescent field, but may reduce the light intensity, which is undesirable for nonlinear light-matter interaction as well as photothermal/photoacoustic spectroscopy. Shown in Fig. 2.14 are the portion of evanescent field and the mode field area for light beam with wavelength of 1550 nm in nanofiber of different diameters. As seen, with reduced diameter, there will be higher portion of evanescent field, while the mode field area does not keep decreasing monotonically but soars up when the diameter of nanofiber is less than about 500 nm. This phenomenon originates from the weaker ability of mode

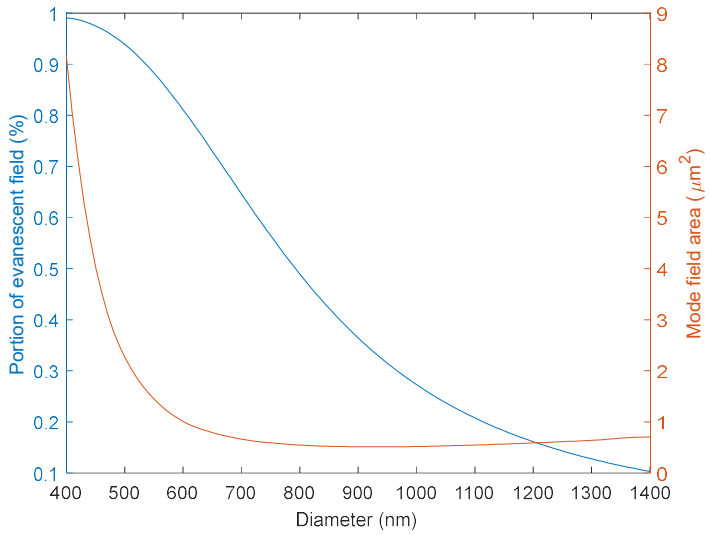

Fig. 2.14 The portion of power in the evanescent field and mode field area for light beam with wavelength of 1550 nm propagating along silica nanofiber with different diameters.

confinement for thinner nanofiber and will result in much reduced intensity of the evanescent field. There should be an optimized diameter where a balance between the portion of power in the evanescent field and the mode field area can be achieved, depending on the specific application.

2.6 Summary

The basics of molecular spectroscopy are given. The separation of the molecular motion into electronic, vibrational and rotational modes bring great convenience for the near-infrared spectroscopy, in which only the ro-vibrational transition is involved. Line broadening effects are annoying for spectroscopic gas sensing, because it not only reduces the peak absorption, but also make the discrete transition lines overlapping with each other and thus hard to discern. The technique of WMS is demonstrated, which is a common but powerful method to increase the SNR in spectroscopy. Finally, the optical nanofiber is introduced as well as its potential advantages for spectroscopic gas sensing.

Chapter 3 Nanofiber based photothermal spectroscopy and the enhancement effect

In this chapter, the photothermal spectroscopy based on nanofiber is presented. Firstly, the basic principle of nanofiber based photothermal spectroscopy is described. A simulation-based comparison of photothermal phase modulation efficiency between the platforms of nanofiber and the commercial HC-1550-02 fiber under the same pumping condition clearly demonstrates the enhancement effect. Secondly, the PT phase modulation coefficients for nanofiber with different diameter are experimentally measured and the optimal size of nanofiber for most efficient PT phase modulation is predicted. Then, experiments of trace acetylene detection based on the nanofiber enhanced photothermal interferometry spectroscopy are implemented. Finally, based on numerical simulations, it is anticipated that higher enhancement can be achieved in nano-waveguides made of materials with larger thermo-optic and thermal expansion coefficients.

3.1. Mechanism of enhancement effect in nanofiber based photothermal spectroscopy

Photothermal interferometry (PTI) spectroscopy has long been proven a highly sensitive method for trace gas sensing [101]. The typical scheme for PTI spectroscopy is that a pump beam with its wavelength matching an absorption line of the trace gas is used to excite the trace molecules into their higher energy level, following which the relaxation process will release the absorbed energy into heat and modify the refractive index (RI) of the surroundings, as shown in Fig. 3.1(a). Then the phase of a probe beam propagating through the heated region with wavelength away from the molecular transition lines will be modulated as:

$$\frac{d\phi}{dz} = \frac{2\pi}{\lambda_{probe}} \Delta n \propto \frac{2\pi}{\lambda_{probe}} \eta \alpha_0 c I_{pump}, \qquad (3.1)$$

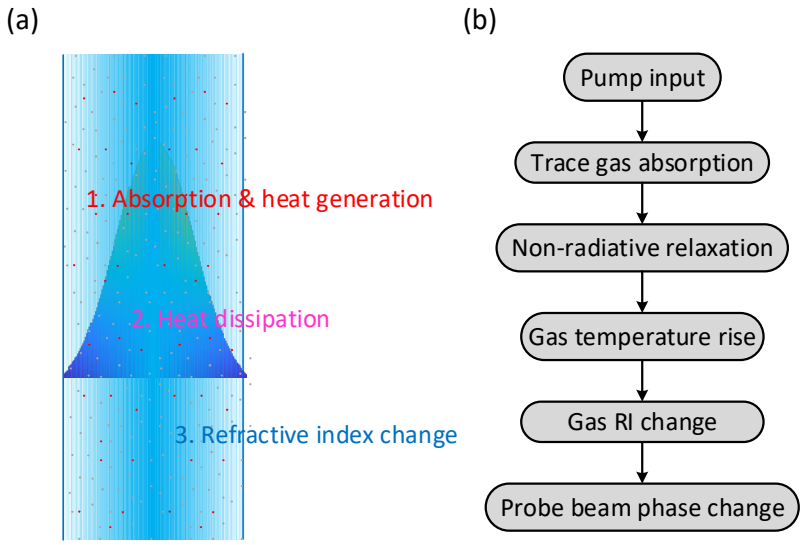

Fig. 3.1 Principle of PTI spectroscopy. (a) Illustration of the pump induced RI change, (b) The main steps in PTI spectroscopy.

where, Δn is the RI change, λ_{probe} is the wavelength of probe beam, η is the thermo-optic coefficient of air, α_0 is the absorption coefficient of 100 % concentration of the target gas, c is the gas concentration, I_{pump} is the intensity of the pump beam. By demodulating the amplitude of phase perturbation, the concentration of trace gas can then be retrieved, as shown in Fig. 3.1(b).

The traditional free-space PTI spectroscopy has already achieved excellent sensitivity down to parts-per-billion (ppb) level using high-power pump laser [102]. In recent years, our group proposed and demonstrated HC-PBG fiber enhanced PTI spectroscopy method for high-sensitivity trace gas detection [33, 103, 104]. By virtue of the small mode field area and thus the high pump intensity as well as the long interaction length, this HC-PBG fiber enhanced PTI spectroscopy method is able to achieve ppb level trace gas sensing with only milliwatt pump level at the near-infrared optical communication band, where the strength of combination band/ overtone transition is much weaker than the mid-infrared. However, both the traditional free-space and the newly proposed HC-PBG fiber enhanced PTI spectroscopy are based on the RI change of air, whose thermo-optic coefficient

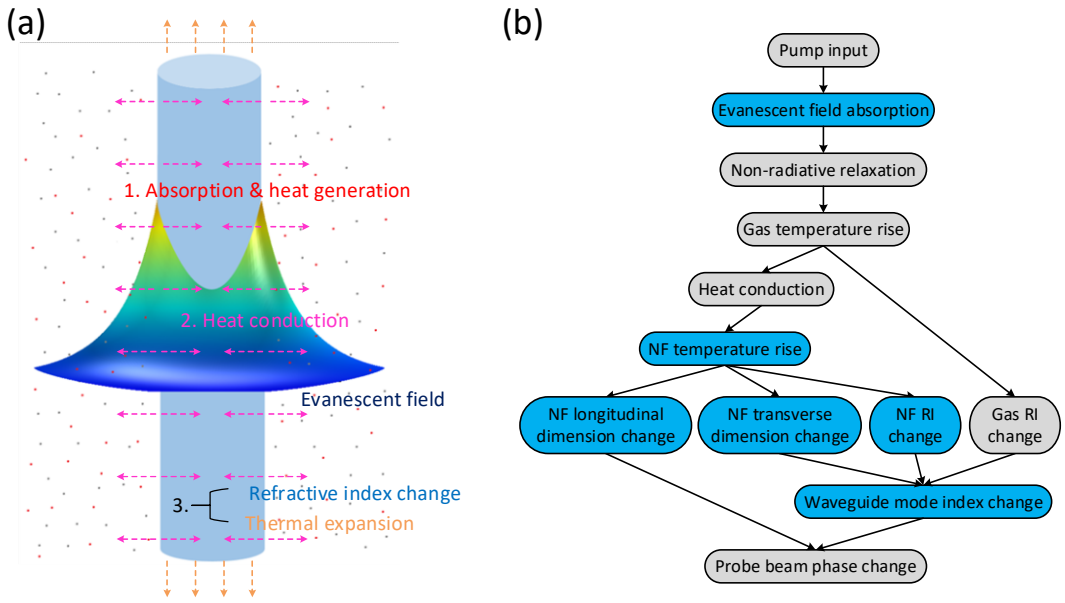

Fig. 3.2 Principle of nanofiber enhanced PTI spectroscopy. (a) Illustration of the pump induced physical changes and (b) Main processes and effects in nanofiber enhanced PTI spectroscopy. The grey filled diagrams represent the processes in common for both the conventional free-space PTI and the nanofiber enhanced PTI, while the blue filled diagrams are the unique processes for the latter one.

is relatively low compared with the solid materials. The novel nanofiber enhanced PTI spectroscopy is intended to achieve higher PT phase modulation efficiency taking advantages of higher light intensity as well as the larger thermo-optic coefficient of the waveguide.

The basic principle of nanofiber enhanced PTI spectroscopy is shown in Fig. 3.2(a). The trace molecules surrounding the nanofiber absorb the pump light through its evanescent field and then release the energy into heat. Then, due to heat conduction, the temperature of silica nanofiber will also increase, which results in change of both the RI and the dimension of nanofiber through the thermo-optic and thermal expansion effects. All of the three factors as RI change of air, RI change of silica and the dimension change of nanofiber contribute in the overall phase modulation. Fig.

3.2(b) summarizes the main processes for nanofiber enhanced PTI spectroscopy method. In the next section, the detailed description of calculation of PT phase modulation efficiency will be presented.

3.2. Method of numerical simulation

The numerical simulation is performed with the aid of the commercial finite element method (FEM) software Comsol Multiphysics and can be divided into three steps. The first step is to get the mode field of the pump beam, which can be calculated using the electromagnetic mode analysis module. The second step is to get the evolution of temperature distribution under the time-dependent pump power, which is assumed to be in the sinusoidal pattern in all the simulations. The third step is to calculate the degree of thermal expansion of the nanofiber and the effective mode index change under the temperature fluctuation.

The evolution of temperature distribution in both the air and nanofiber is governed by the heat transfer equation [105], as:

$$\begin{aligned} \rho_a C_a \frac{dT}{dt} + \nabla \cdot (-k_a \nabla T) + \rho_a C_a \vec{u}_a \cdot \nabla T = Q(r,\theta,t) \\ \rho_s C_s \frac{dT}{dt} + \nabla \cdot (-k_s \nabla T) = 0 \end{aligned}, \qquad (3.2)$$

where, the upper and lower equations in Equ.(3.2) describe the heat transfer in the surrounding air and in the nanofiber, respectively. The ρ, C, k and $\vec{u}$ are respectively the density, heat capacity, thermal conductivity and velocity field, with the subscripts a and s representing the air and silica material respectively. The heat source $Q(r,\theta,t)$ only exists in air and is related with the evanescent field as:

$$Q(r,\theta,t) = \alpha(c) P_{pump} A_{eff}^{-1} I_{ne}(r,\theta) g(t), \qquad (3.3)$$

where, α is the absorption coefficient of the surroundings and is proportional to the concentration of trace acetylene c, P_{pump} is the power of incident pump and is assumed to be a constant along

propagation as long as the nanofiber is made with low loss, A_{eff}^{-1} is the effective mode field area, $I_{ne}(r,\theta)$ is the normalized intensity distribution of the evanescent field of the pump beam, $g(t)$ is the time-dependent power modulation function for the pump beam. The refractive index distribution is determined by the instant temperature, as:

$$\begin{matrix} n_a(r,\theta,t) = [T_a(r,\theta,t) - T_0]\dfrac{dn_a}{dT} + n_a(T_0) \\ n_s(r,\theta,t) = [T_s(r,\theta,t) - T_0]\dfrac{dn_s}{dT} + n_s(T_0) \end{matrix}, \qquad (3.4)$$

where, the dn_a/dT and dn_s/dT are respectively the thermo-optic coefficients of air and silica material, and approximately equal to -0.9 and $9 \times 10^{-6}\,K^{-1}$ at room temperature. Although the transverse dimension is also changed due to temperature modulation through the thermal expansion effect, its influence in determining the mode index has been checked to be much smaller than the refractive index change. Hence, the modification of mode index n_{mo} can be regarded as solely RI dependent as:

$$\Delta n_{mo}(t) = n_{mo}\left[n_a(r,\theta,t), n_s(r,\theta,t), \lambda_{probe}, S(r,\theta)\right] - n_{eff}(T_0), \qquad (3.5)$$

where, $S(r,\theta)$ is the geometrical shape of the nanofiber. Both of the Equ.(3.2) and (3.5) can be numerically solved with the FEM by Comsol. In addition to the mode index change, the contribution to the phase modulation from longitudinal dimension change of the nanofiber cannot be neglected, which is caused by thermal expansion effect as:

$$\Delta L(t) = L(t) - L_0 = L_0 e_s \Delta T_s(t), \qquad (3.6)$$

where, L_0 is the length of nanofiber and e_s is the thermal expansion coefficient of silica. Then the overall phase modulation will be the combination of effective mode index change and the longitudinal dimension change as:

$$\Delta\varphi(t) = \frac{2\pi}{\lambda_{probe}} L_0\left[\Delta n_{mo}(t) + \overline{n}_{eff} e_s \Delta T_s(t)\right] = \frac{2\pi}{\lambda_{probe}} L_0(\Delta n_{to} + \Delta n_{te}), \qquad (3.7)$$

It would be convenient hereby to define the first and the second term in Equ.(3.7) as the effective RI modulation due to thermo-optic and thermal expansion effects denoted as Δn_{to} and Δn_{te}, respectively, while the summation of them can be defined as the total effective RI modulation and denoted as Δn_{tt}.

To quantitatively evaluate the enhancement of PT effect on the nanofiber platform, the simulations are performed under the conditions of 1% acetylene in air with absorption coefficient $\alpha = 1.05\ cm^{-1}$ at $\lambda_{pump} = 1532.83\ nm$, corresponding to the P(13) transition line of acetylene ($J' = 12 \rightarrow J'' = 13$ for $v_1 + v_3$ vibrational combination band). There are several reasons for choosing the P(13) transition line. First, it is one of the several strongest absorption lines in the near-infrared band, as can be seen in Fig. 2.7. Second, there are basically no or little other absorption lines with week strength in its two wings, which results in a clear absorption profile when the pump wavelength is swept across it. Third, there are powerful pump sources with narrow linewidth, such as, DFB laser combined with EDFA, as well as mature optical apparatus near the target wavelength, which greatly enhances the performance of the system. For the selected transition line, the absorbed pump power $P_{absorbed}$ for the trace acetylene will be $1.05P_{pump}\ cm^{-1} \cdot ppm^{-1}$. As an example, for a 100 mW pump beam transmitting through a one meter absorption path in trace acetylene with concentration of 100 ppm, the overall absorbed pump power that contributes to the photothermal effect will be 1.05 mW. In our simulation, the pump power P_{pump} is assumed to be $40\ mW$ with an intensity modulation function of $g(t) = 2^{-1}[1 + sin(2\pi ft)]$. The wavelength of probe beam λ_{probe} is chosen to be $1553\ nm$, where the acetylene is transparent for the probe beam.

A comparison of the resulting temperature distribution between a 800 nm-diameter nanofiber and HC-1550-02 fiber under pump modulation frequency $f_p = 50\ kHz$ is shown in Fig. 3.3. The optical modulation frequency, at which the signal-to-noise ratio should be the highest, may not the 50 kHz. However, the parameter of $50\ kHz$ in simulation is a reasonable choice for comparison, in consideration of the previous work related to photothermal spectroscopic acetylene detection, where tens of kilohertz modulation frequencies are used basically [33, 61, 62]. It also worth

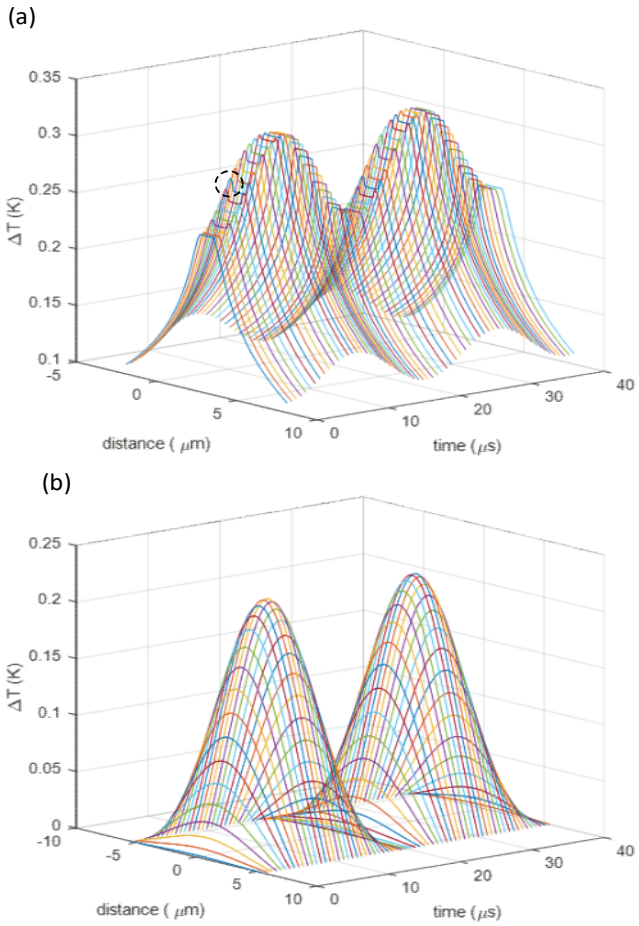

Fig. 3.3 Temperature distribution under the same pumping condition of $50\,kHz$ intensity modulation for the cases of (a) 800 nm-diameter nanofiber and (b) HC-1550-02 fiber. The core diameter of the hollow fiber is $10.5\,\mu m$. The mode field diameter at the pump and probe wavelength are the same and equals to $6\,\mu m$.

mentioning that higher modulation frequency is generally beneficial to lowing the system noise, but the amplitude of photothermal signal is also reduced due to the less heating and cooling time in one period. In the time slots of 0 to 10 μs and 20 to 30 μs, there are tiny temperature spikes close to the nanofiber, as is marked by the dashed circle in Fig. 3.3(a). The ting spikes appearing in the pump on stage originates from the evanescent field heating and heat sink effect of the silica nanofiber. Due to the positive differential temperature between the air and the surface of nanofiber, the heat flows into the nanofiber and increases its temperature. The temperature modulation amplitude at the center

of the nanofiber and HC-1550-02 fiber are 88 and 194 mK respectively. This temperature fluctuation will cause modulation in the mode index. For the HC-1550-02 fiber, this can be calculated with the perturbation method [106], as:

$$\Delta n_{mi} = \frac{\iint \Delta n E^2 ds}{\iint E^2 ds} = \frac{\iint \frac{dn}{dT} \Delta T E^2 ds}{\iint E^2 ds}, \qquad (3.8)$$

where, the E is approximately in Gaussian shape for the fundamental mode of the hollow core fiber. However, for the nanofiber case, it is more precise and convenient by the numerical method offered by the mode analysis module in Comsol to calculate the mode index change, as described in Equ. (3.5). The amplitude of mode index modulation can be defined as the difference in mode index at

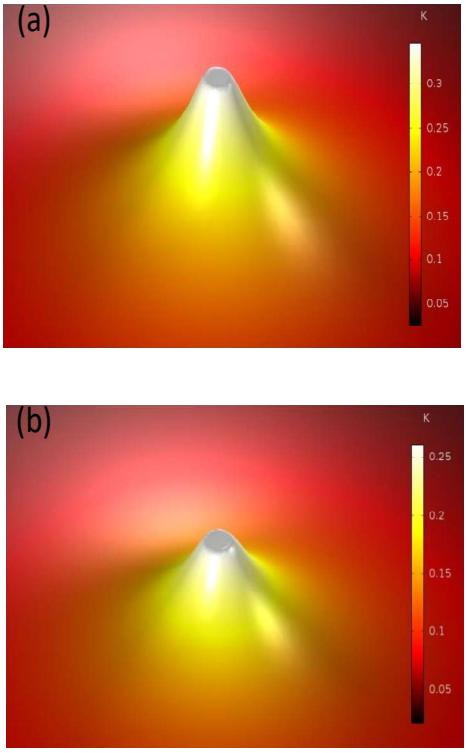

Fig. 3.4 The temperature distribution for the nanofiber case at the time point of (a) 30 μs and (b) 40 μs, at which the mean temperature are the highest and lowest, respectively.

the time of 30 and 40 μs, where the mean temperature is the highest and lowest respectively. Shown in Fig. 3.4, are the temperature distribution for the nanofiber case at these two time points. The mode index modulation amplitude for the nanofiber and HC-1550-02 cases are then calculated to be $\Delta n_{to} = 3.8 \times 10^{-7}$ and -1.05×10^{-7} respectively. While for the nanofiber case, apart from the mode index modulation, there is also contribution to the phase shift from the thermal expansion effect, whose amplitude is calculated to be $\Delta n_{te} = 3.9 \times 10^{-8}$. Then the total effective RI modulation amplitude for the nanofiber case is calculated to be $\Delta n_{tt} = 4.19 \times 10^{-7}$, according to the Equ. (3.7). As seen, compared with the HC-PBG fiber, the PT efficiency of 800 nm-diameter nanofiber is about 4 times higher under the conditions of $f_p = 50\ kHz$ and $\lambda_{probe} = 1553\ nm$. o normalize the factors of pump level and the trace acetylene concentration, it is better to define the normalized effective RI modulation coefficients as η_{to}, η_{te} and η_{tt}, in which both of the pump power and the acetylene concentration are divided from the Δn_{to}, Δn_{te} and Δn_{tt}, respectively. Then, the dimension of those normalized effective RI modulation coefficients will be $ppm^{-1} \cdot W^{-1}$. The η_{to}, η_{te} and η_{tt} in the abovementioned nanofiber case are then calculated to be 9.5×10^{-4}, 0.98×10^{-4} and 10.5×10^{-4} cm $\cdot W^{-1}$, respectively.

Following the method introduced above, a group of simulations with different diameter of the nanofiber ranging from 1200 to 400 nm are performed. It is found that the η of nanofiber enhanced PTI highly depends on the diameter of the nanofiber, as shown in Fig. 3.5(a). For the diameters larger than 750 nm, the effective RI modulation coefficient due to thermo-optic effect η_{to} (depicted as the dot dashed line) increases with decreasing diameter and reaches its peak value around 750 nm. However, for the further reduced diameters, the η_{to} drops rapidly and even becomes negative for diameters less than 550 nm. While for the thermal expansion effect originated effective RI modulation η_{te} (depicted as the dashed line), it basically increases monotonically with reduced diameter in the range from 1200 nm to 400 nm. The total effective RI modulation coefficient η_{tt}, which is the sum of η_{to} and η_{te}, has the largest value around 700 nm for $\lambda_{probe} = 1553\ nm$. So, for the nanofiber enhanced PTI operating in optical communication band, the optimal performance can be achieved in nanofiber with diameter of about 700 nm.

To explain the variation of effective RI modulation coefficients with different diameter, a group of simulations are performed, in which the fraction of the evanescent field for the light beams as well as the peak normalized ratio of surface pump intensity over the cross-sectional area of the nanofiber are calculated, as presented in Fig. 3.5(b). The evanescent field of pump beam serves as the heat

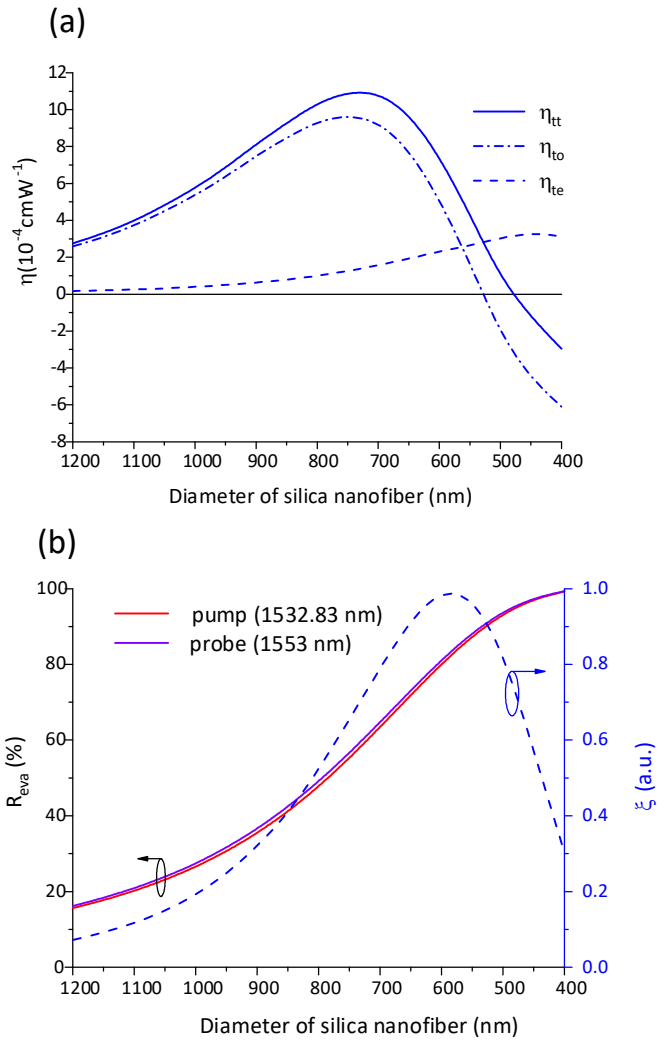

Fig. 3.5 Numerical result for nanofiber enhanced PTI with 1553 nm probe beam. (a) Effective RI modulation coefficient for nanofibers of different diameter. (b) Portion of the evanescent fields (R_{eva}) and the relative value of the surface pump intensity over cross-sectional area of the nanofiber (ξ).

source, while the silica nanofiber is the substance to be heated with the required energy proportional to its cross-sectional area. When the diameter of nanofiber is reduced, the cross-sectional area keeps decreasing which favors the heating process, as there will be less volume of silica material to heat. However, if the diameter is excessively reduced, the surface intensity and thus the power density of heating drops rapidly due to the largely expanded mode field area that reduces the temperature modulation efficiency. In addition, with reduced diameter, there will also be more exposed mode field for the probe beam, which experiences the negative RI modulation of the air and thus counteracts the positive RI modulation experienced by the other part of probe beam that remains in the core of nanofiber. The overall mode index modulation amplitude is then compromised by the competitive effect between the core field and evanescent field of the probe. For diameters less than about 550 nm, the evanescent field of the probe dominates over the core field and reverse the sign of η_{to}, as seen in Fig. 3.5(a).

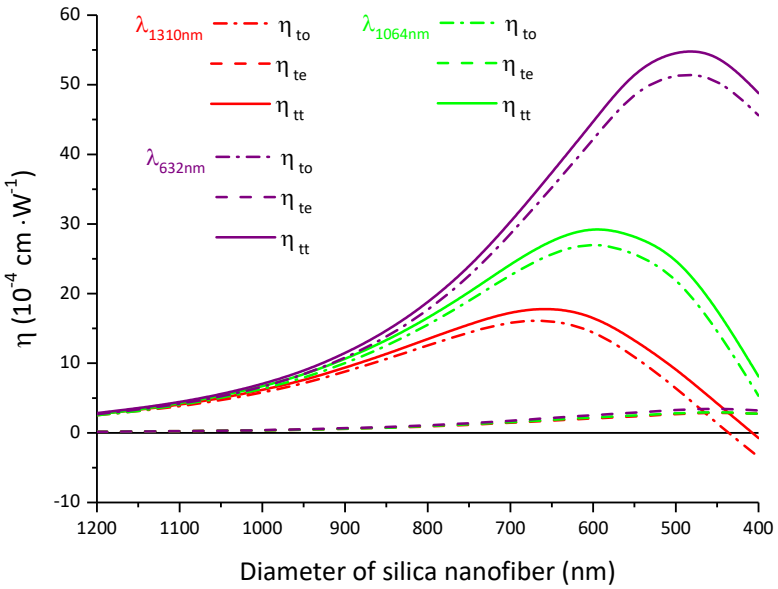

Fig. 3.6 Numerical result of effective RI modulation coefficients for nanofiber enhanced PTI with the different wavelength of probe beam.

To relieve the counteracting effects between the core and evanescent parts of the probe beam, the fraction of its evanescent field should be reduced which can be achieved by adopting probe beam with shorter wavelength. This strategy is then verified by a group of numerical simulations, as shown in Fig. 3.6. By reducing the wavelength of the probe, not only does the optimal diameter move to thinner diameter, but also the peak effective RI modulation coefficient is much improved. For the scheme with 632 nm probe beam, there is an additional five times improvement in PT phase modulation amplitude compared with 1553 nm probe beam.

3.3. Experimental calibration of normalized effective RI modulation coefficients

The nanofibers are fabricated from the standard single mode fiber(SMF) with the flame brushing technique [73] using the homemade fiber taper machine in our group. Pure hydrogen generated from the water electrolysis works as the source of flame. The hydrogen flame heats and softens the silica fiber with two stepping motors pulling and tapering it meanwhile. The samples are all made with the same waist-length of about 12 mm, determined by the flame scanning range of the taper machine. After fabrication, each sample is sealed in a glass gas cell for robust packaging as well as prevention from dust pollution. There are two holes drilled and installed with gas valve, so that the gas samples can be filled in or flushed out. The two pigtails are left outside for optical connection.

To calibrate the overall effective RI modulation coefficient η_{tt} for a piece of nanofiber, the 3x3 Sagnac interferometer system is used [107], which is more convenient for plug and play compared with the MZI system, especially when there are multiply samples to be calibrated. The 3x3 Sagnac interferometer system is passively stabilized and do not require an active quadrature-point locking apparatus. The setup of the 3x3 Sagnac system is shown in Fig. 3.7 [103]. A laser diode with a center wavelength of 1553 nm and 3 db bandwidth of 1.2 nm works as the broadband probe source, so that the interference noise due to the backward Rayleigh scattering can be well suppressed. The polarization controller is used to optimize the polarization state for highest signal amplitude. After

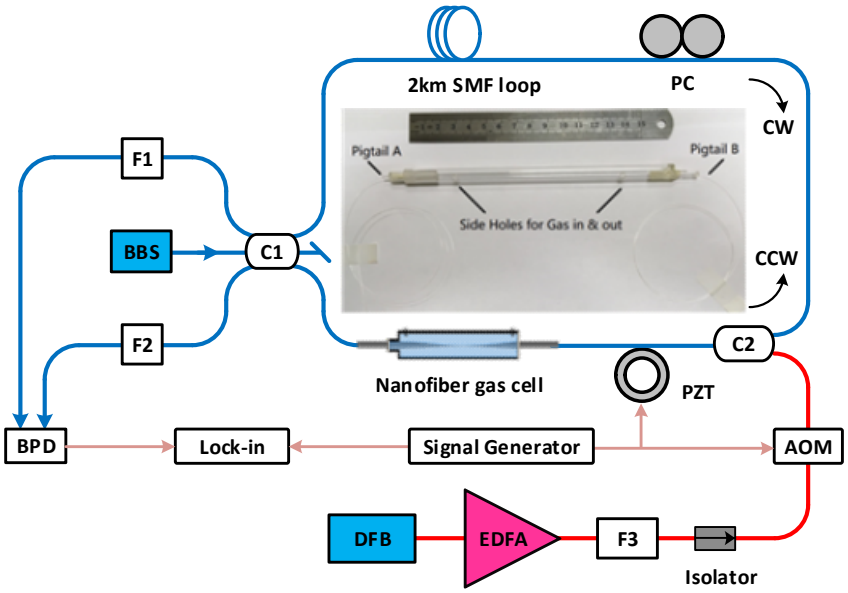

Fig. 3.7 The setup of 3x3 Sagnac system for calibration of η_{tt}. BBS: broadband source; C1: 3x3 coupler; PC: polarization controller; C2: 5:95 coupler; PZT: piezoelectric fiber stretcher; F1, F2 and F3: optical filters; BPD: balanced photodetector; Lock-in: lock-in amplifier; DFB: distributed feedback laser; EDFA: erbium doped fiber amplifier; AOM: acousto-optic modulator. The inset shows the image of the gas cell with sealed nanofiber.

going through the loop, the clockwise (CW) and counterclockwise (CCW) probe beam recombine and are then detected by the balanced photodetector (BPD) with the signal demodulated by a lock-in amplifier. The optical filter F1 and F2 are used to eliminate the pump light. The pump beam is offered by a distributed feedback (DFB) laser centering at 1532.8 nm and is then amplified by an erbium doped fiber amplifier (EDFA). The optical filter F3 is for elimination of the amplified spontaneous emission (ESA). Before injected into the probe loop through the 95% port of the coupler C2, the pump beam is intensity modulated by the acousto-optic modulator (AOM) with the pattern as $g(t) = 2^{-1}[1 + sin(2\pi ft)]$. The peak and mean power injected into the nanofiber is kept at 40 and 20 mW respectively.

An example of the calibration process for a 800 nm-diameter and 12 mm-long nanofiber is given as

follow. Firstly, the signal for pump beam tuned to 1532.8 and 1533.0 nm with pure nitrogen filled in the gas cell are recorded and denoted as o_1 and o_2, respectively. Then inflate 0.75 % acetylene balanced by nitrogen into the gas cell, and measure the signal still at these two wavelength and denoted as o_3 and o_4, respectively. In the ideal case, there should not be photothermal signal when the pump is tuned off the absorption line to 1533.0 nm, which means both the o_2 and o_4 should be zero. However, due to the pump absorption of nanofiber itself and the adsorbed aerosol on the surface of the nanofiber, there is a background absorption that results in non-zero o_2 and o_4. This background photothermal signal should be subtracted and the pure PT signal will be:

$$s_{PT} = (o_3 - o_4) - (o_1 - o_2), \qquad (3.9)$$

where, both the Kerr effect and the inequality of pump power for the on- and off-line wavelength are compensated by Equ.(3.9). Then a sinusoidal wave of the same frequency from the signal generator is used to drive the piezoelectric fiber stretcher (PZT). Tune the amplitude of the electric driving signal until the detected optical signal equals to s_{PT} and record the electric amplitude as A_{PT}. Then the real amplitude of phase modulation corresponding to the s_{PT} measured above is calibrated by PTZ to be:

$$\Psi_{PT} = \frac{A_{PT}}{A_\pi} \cdot \pi, \qquad (3.10)$$

where, A_π is the amplitude of the electric signal when the phase modulation amplitude reaches π rad, which can be readily discerned from the oscilloscope due to its unique waveform [108]. In the experiment for a 800 nm-diameter, 12 mm-long nanofiber under 50 kHz sinusoidal intensity modulation with 40 mW peak pump power, the measured values for o_1, o_2, o_3, o_4, s_{PT}, A_{PT}, A_π are 10.44, 10.42, 13.23, 10.04, 3.17, 22.8 and 5.8×10^3 mV respectively. Then the Ψ_{PT} is calculated to be 12.4 mrad, resulting in a total effective RI modulation coefficient as:

$$\eta_{tt} = \frac{1.24 \times 10^{-2}\ rad \cdot 1553\ nm}{0.04W \cdot 0.75\% \cdot 1.05\ cm^{-1} \cdot 2\pi\ rad \cdot 12\ mm} = 8.1 \times 10^{-4}\ cm \cdot W^{-1}, \qquad (3.11)$$

Table 3.1 Experimentally measured and numerically simulated values of total effective RI modulation coefficient η_{tt} for nanofibers of different diameter.

Diameters (nm)	η_{tt}^{exp} $(cm \cdot W^{-1})$	η_{tt}^{num} $(cm \cdot W^{-1})$
1120	2.5×10^{-4}	3.5×10^{-4}
1060	3.8×10^{-4}	4.6×10^{-4}
900	6.2×10^{-4}	8.1×10^{-4}
800	8.1×10^{-4}	10.5×10^{-4}
670	5.0×10^{-4}	9.8×10^{-4}

Following the method fully described above, the η_{tt} for nanofibers of different diameter are listed in Table 3.1, with the theoretical values by simulation also given. The deviation of experimental values from the numerical ones are within 30 %. There could be three reasons for the smaller experimental results. First, due to the background absorption of nanofiber, its temperature cannot be assumed as room temperature but should be higher. Then through thermal diffusion, the necessary is much heated which results in less air density as well as the number of light-absorbing acetylene molecules. Second, the scattering loss at the surface of nanofibers are neglected in the simulation. Third, the diameter is measured at the middlemost position, which is the thinnest. The diameter at other positions within the waist region is little bit higher.

The modulation frequency also has an impact on the PT signal due to a quite straightforward reason that the longer the heating time, the larger the temperature and thus the RI modulation amplitude. Both the numerical and the experimental results, as shown in Fig. 3.8 where the experiment is performed with the same piece of 800 nm-diameter nanofiber, demonstrate that the signal amplitude can be improved at the low frequency range. However, the noise are generally also increased in lower frequency band. So, there should be a balance between the signal amplitude and the noise level in choosing the modulation frequency, so that the highest signal-to-noise ratio (SNR) can be achieved.

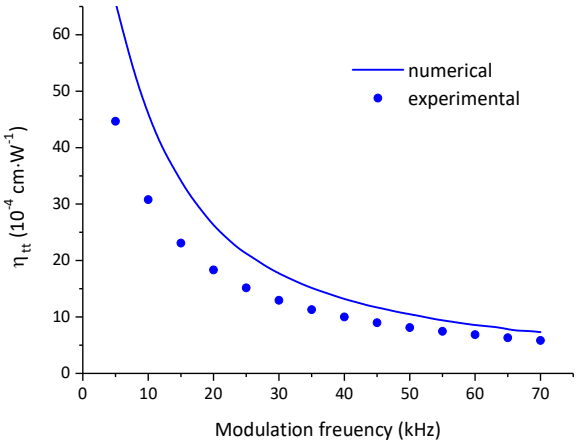

Fig. 3.8 Numerical and experimental result of the amplitude of PT signal with different modulation frequency.

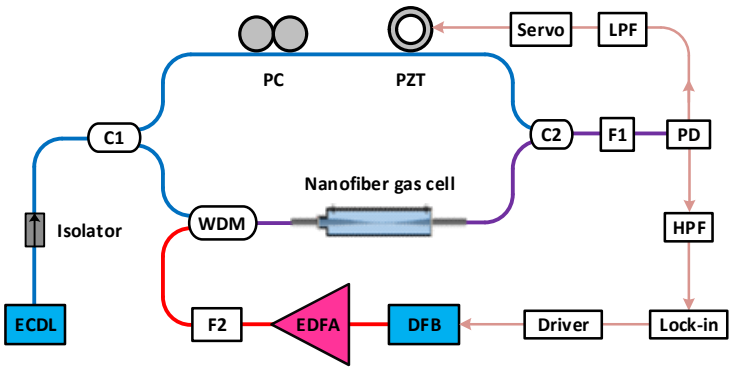

Fig. 3.9 Experimental setup of MZI for trace acetylene sensing. ECDL: external cavity diode laser, C1, C2: optical couplers; F1, F2: optical filters; PD: photodetector; LPF and HPF: low- and high-pass electric filter; WDM: wavelength division multiplexer.

3.4. Trace acetylene sensing

Having verified the enhancement effect of PT in the well-designed nanofiber both theoretically and experimentally, the trace acetylene sensing experiment is then performed based on the wavelength

modulation spectroscopy (WMS) still with the 800 nm-diameter and 12 mm-long sample. The experimental setup is now a MZI as shown in Fig. 3.9, which has a relatively higher phase detection sensitivity compared with the 3x3 Sagnac system in our lab [109].

The source for probe light is an external cavity diode laser (ECDL) with 300 kHz linewidth, 1557 nm wavelength and 1 mW output power. The probe light is split into two beams at the coupler C1 with the upper beam for phase locking through the PZT and the lower beam for phase detection. The optical filter F1 centers at 1557 nm to eliminate the pump light. The detected signal of probe beam is divided into two parts, one is for the servo controller to lock the interferometer at the quadrature point and the other is sent to the lock-in amplifier for second-harmonics demodulation. The pump beam centers at the P(13) line of acetylene (1532.8 nm) and is from the DFB laser which is wavelength modulated at 31 kHz through the injection current driven by the lock-in amplifier. The reason for choosing the 31 kHz pump modulation frequency is that its second harmonics is at 62 kHz where the PZT has its lowest noise level. The wavelength modulation depth is selected to be ~ 2.2 times the linewidth of P(13) transition line. Apart from the fast wavelength modulation, the pump beam is also simultaneously ramped across the absorption line with low rate from 1532.74 nm to 1532.92 nm, corresponding to a detuning range of ± 90 pm with respect to the line center. Shown in Fig. 3.10(a) is the second harmonics output for different concentration of acetylene as 450, 525, 600 and 675 ppm balanced by nitrogen under 50 mW pump. It should be mentioned that there is a relatively large background signal as well as a certain degree of distortion in the output waveform which could originate from the absorption of the adsorbed dust on the surface of nanofiber. In addition, the asymmetric waveform with respect to zero detuning should originate from the spectrum dependent absorption of either the nanofiber itself or the particles attached on its surface. The PT signal is defined as the peak-to-peak value of the output waveform and can be found to be basically linear with the acetylene concentration, as shown in Fig. 3.10(b).

The results of second harmonic output and linearity of the PT signal under different pump power with fixed concentration of 750 ppm acetylene are shown in Fig. 3.11(a) and (b), respectively.

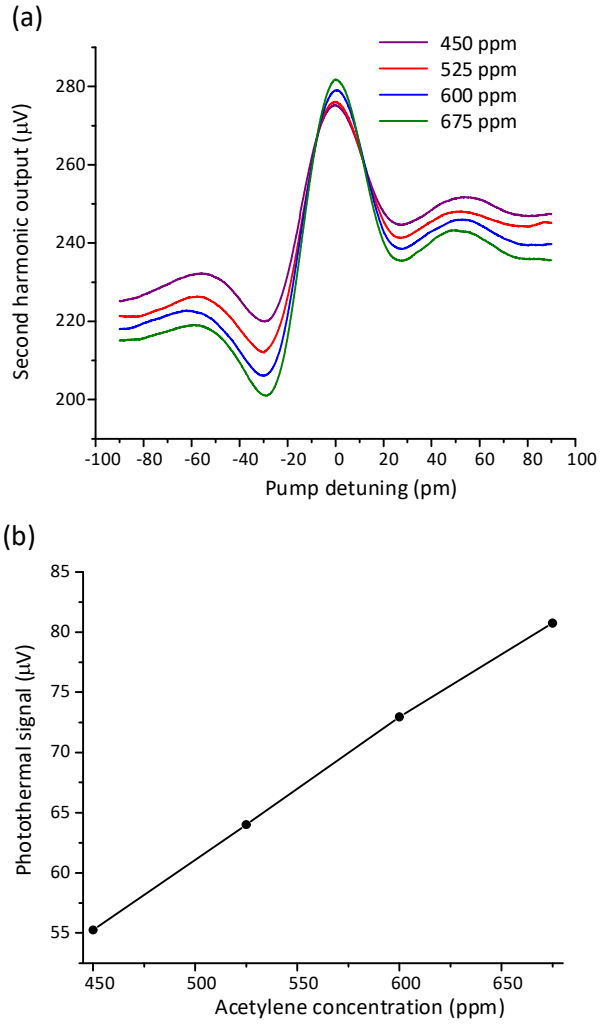

Fig. 3.10 Experimental result of nanofiber based trace acetylene sensing with different concentration. (a) Second harmonic output with fixed pump power of 50 mW. (b) Linearity of the PT signal with different concentration.

Shown in Fig. 3.11(b) is also the result of the noise level, which is determined as the standard deviation of the second harmonic output over a period of one minute with the center wavelength of pump beam tuned 90 pm away from the line center and a fixed pump power of 88 mW. As seen, not only the PT signal but also its background signal are proportional to the pump level, which further verified our supposition that it is the substance attached on the surface of nanofiber causes the relatively large background PT signal. The background absorption from the nanofiber itself should

not be spectrum dependent within the amplitude of wavelength modulation, so it is readily subtracted in the peak-to-peak value. However, the spectrum-independent absorption may not be guaranteed for the various kinds of aerosol or particles adsorbed on the surface of the nanofiber. Ideally, is better to fabricate the nanofiber in a cleanroom and seal it immediately into a cell with dust-filtering apparatus at the inlet. As to the noise level, although it also increases with the pump power, the slope is lower than the signal, which means the SNR can be effectively improved with higher pump power. The trace acetylene detection limit for this 800 nm-diameter and 12 mm-long nanofiber is evaluated by the experimental result achieved with 88 mW pump and 750 ppm acetylene, in which the signal, noise, SNR and noise equivalent detection limit are found to be 156 μV, 123 nV, 1270 and 600 ppb respectively.

The direct heating of the nanofiber itself is actually an annoying problem, especially when the absorption is spectrum dependent. First, it makes the wavelength sweeping process quadrature but not optional. If there is no background absorption like in the scheme of free space or hollow-core fiber, the pump can be fixed at the center of absorption line and the measured photothermal signal is still proportional to the gas concentration. However, when there is background photothermal signal, as in the nanofiber case here, the pump wavelength should always sweep across the absorption line and take the peak-to-peak value as the real photothermal signal so that to substrate the background level. This sweeping process is time consuming, especially for high precision requirement, where larger averaging time is needed. Second, it results in excessive temperature rise of both the nanofiber and the ambient air, which reduces the air density and thus the number of light-absorbing molecules. This effect will be exaggerated when higher pump power is used. As to the stability and possibility of real-time measurement, the prevention of pollution to the nanofiber should be the key point. A good protection needs to eliminate both the dust and aerosols contained in the sample gas, which can result in both transmission degradation and higher background photothermal signal. The stability of the system depends on the temperature fluctuation, environmental vibration and the ability of quadrature point locking in the interferometer. The real application needs further investigation.

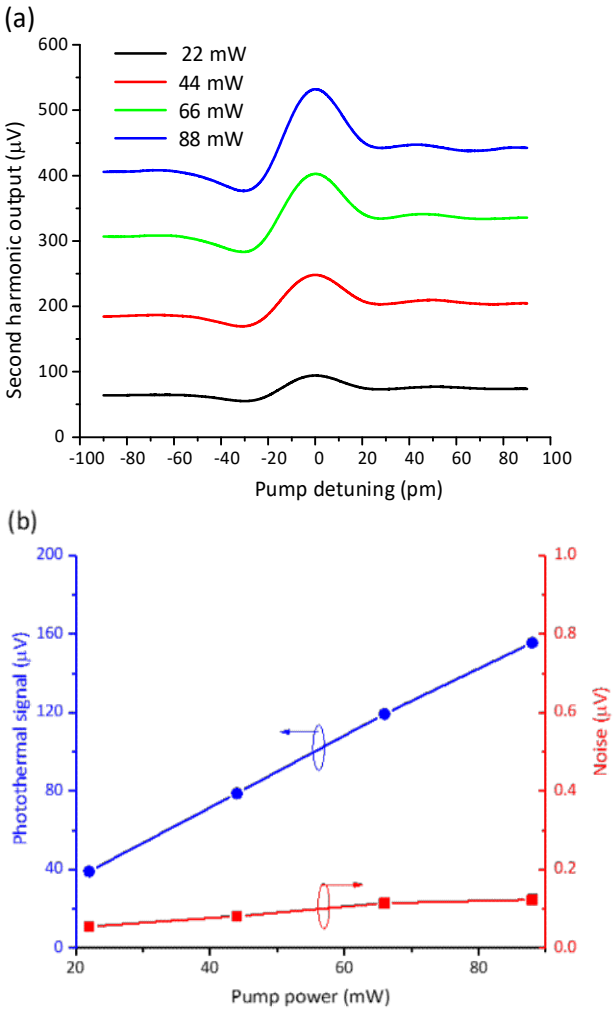

Fig. 3.11 Experimental result of nanofiber based trace acetylene detection with different pump power. (a) Second harmonic output under different pump level with fixed acetylene concentration of 750 ppm. (b) PT signal and noise level with different pump power.

3.5. Further enhancement

The nanofiber enhanced PTI spectroscopy has been demonstrated both numerically and theoretically in the previous four sections. However, there could be further tremendous enhancement by switching to nano-waveguides made of materials with large thermo-optic or thermal expansion

Table 3.2 Thermal and optical parameters relevant to the PTI spectroscopy for air, silica, CYTOP and silicon.

Properties	Air	Silica	CYTOP	Silicon
Transparent window /μm	UV to IR	0.2~2.2 [110]	NIR [111]	1.1~6.5 [110]
Refractive index	1.0003 [112]	1.445 [113]	1.345 [114]	3.45 [115]
Density $/\mathrm{Kg \cdot m^{-3}}$	1.205 [110]	2203 [110]	2030 [116]	2330 [110]
Heat capacity $/\mathrm{J \cdot Kg^{-1}K^{-1}}$	1005 [110]	703 [110]	861 [116]	714 [110]
Thermal conductivity $/\mathrm{W \cdot m^{-1}K^{-1}}$	0.026 [110]	1.38 [110]	0.12 [116]	140 [110]
Thermo-optic coefficient $/10^{-6}\ \mathrm{K^{-1}}$	-0.91 [101]	9 [113]	-50 [117]	175 [115]
Thermal expansion coefficient $/10^{-7}\ \mathrm{K^{-1}}$	NA	4.0 [118]	740 [117]	26 [110]

coefficients, such as polymer and semiconductor material. The thermal and optical parameters for two promising materials, i.e., the cyclic transparent optical polymer (CYTOP) and the silicon, are listed in Table 3.2, with those for air and silica also listed for comparison.

As seen from Table 3.2, the thermal expansion coefficient of CYTOP and the thermo-optic coefficient of silicon are several orders of magnitude larger than the silica. It is anticipated that optical nano-waveguides made from these two materials can achieve orders of magnitude higher effective RI modulation coefficients than the silica nanofiber not to say the traditional free-space scheme. This idea is theoretically verified by numerical simulation with nano-waveguide made of CYTOP and silicon as shown in Fig. 3.12(a) and (b) respectively. In the simulation with CYTOP, all the pumping parameters are kept the same as those in the simulation with silica. While in the simulation for silicon nano-waveguide, there is only one change that the pump beam centers at 3.03 μm, corresponding to the R(9) absorption line, where the absorption coefficient is about 20 times larger than the P(13) line. For the nanofiber made of CYTOP, the dominant effective RI

modulation comes from the positive thermal expansion effect but not the negative thermo-optic effect. The η_{te} increases first but then drops with reduced diameter of the CYTOP nanofiber when it is less than about 500 nm. This phenomenon is still caused by the variation of ξ as has been demonstrated in the silica nanofiber case. The total effective RI modulation coefficient η_{tt} for the CYTOP nanofiber drops with reduced wavelength of the probe, which is different from the silica nanofiber. The reason is that the shorter the wavelength of the probe beam, the larger the portion of the probe beam remains inside the CYTOP material, whose thermo-optic coefficient is much larger than the air, and hence the more negative RI modulation will be experienced by the probe beam. As the negative thermo-optic effect counteracts the dominant positive thermal expansion effect, probe beam with longer wavelength is preferred whose more exposed evanescent field in air results in less negative η_{to} and thus larger positive η_{tt}. Numerical results for silicon nano-waveguide with different size are shown in Fig. 3.12(b). The waveguide has a fixed height-width ratio of 2 and is supported by a silica wedge with the width of contact area fixed to 20 nm to suppress the heat flow from the silicon waveguide to the silica substrate. The amplitudes of η_{to}, η_{te} and η_{tt} with the reduced size of the nano-waveguide follows the same trend as in silica nanofiber case due to the same reason and will not be re-explained here. Due to the much larger thermo-optic coefficient of silicon material as well as the larger absorption coefficient of acetylene at 3.03 μm, the PT RI modulation efficiency can be about 800 and 8000 times larger than the silica nanofiber and HC-1550-02 fiber, respectively. On the other hand, the tremendously enhanced PT effect in silicon nano-waveguide for trace gas sensing appeals well to the emerging research of spectroscopic detection of trace molecules on chip, which has the attractive prospect of integrating the laser source, sensing element and photodetector compactly on a piece of photonic chip.

3.6 Summary

The nanofiber enhanced PTI spectroscopy is demonstrated. The numerical simulation with silica nanofiber demonstrated the higher enhancement of the PT phase modulation amplitude compared with the HC-1550-02 fiber. The results of numerical simulation for the silica nanofiber also work as

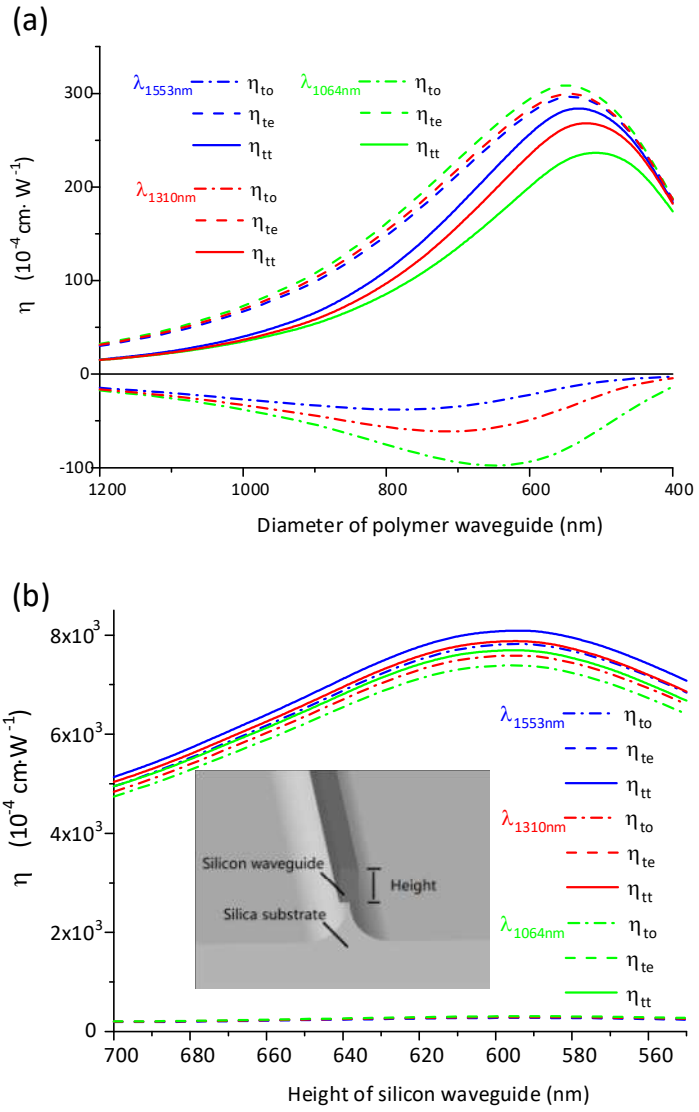

Fig. 3.12 Numerical result of effective RI modulation coefficients for nano-waveguide made of (a) CYTOP and (b) silicon with different size of the waveguide and different wavelength of probe beam. Insert: geometric dimension of the silicon nano-waveguide [119].

the guidance in determining the optimal diameter of nanofiber. The experimentally measured effective RI modulation coefficients for silica nanofibers with different diameters verified the theory of nanofiber enhanced PTI spectroscopy. The trace acetylene sensing experiment is performed with a 800 nm-diameter and 12 mm-long silica nanofiber. A noise equivalent detection limit of 600 ppb is achieved with 88 mW pump power. Based on the numerical simulation, it is anticipated that by

switching to nano-waveguides made of materials with much larger thermo-optic or thermal expansion coefficients, such as CYTOP and silicon, further tremendous enhancement in PT phase modulation efficiency can be achieved.

Chapter 4 Nanofiber enhanced stimulated Raman spectroscopy for high sensitivity hydrogen sensing

Homodiatomic molecules, such as hydrogen, oxygen and nitrogen, are infrared transition forbidden and thus has basically no absorbance throughout the whole infrared band. The only effective method of spectroscopic detection may be the Raman scattering, which is intrinsically a nonlinear process and thus inclined to higher light intensity. In this chapter, the highly efficient stimulated Raman scattering (SRS) on the nanofiber platform and its application in high sensitivity trace hydrogen detection will be demonstrate. Firstly, a qualitative demonstration of the advantage of nanofiber based Raman interaction in comparison with the traditional free space as well as the newly developed HC-PBG fiber counterparts will be given. Then a series of systematic trace hydrogen sensing experiments are performed. The experimental results clearly manifest the nanofiber based SRS a highly sensitive and fast-response method for trace hydrogen detection. Finally a theoretical simulation is performed which explains the polarization dependent amplitude of the Raman signal and serves as the guidance for further improvement of the experimental system for more stable operation.

4.1 Introduction of nanofiber enhanced SRS

4.1.1 Basics of Raman spectroscopy

Raman spectroscopy has long been used for substance detection as well as spectroscopic imaging due to its ability to distinguish different vibrational or rotational motions that are uniquely associated with a specific type of molecule. For the trace gas molecule detection applications, there are typically two kinds of Raman scattering used, one is the spontaneous Raman scattering and the other is SRS as depicted in Fig. 4.1(a) and (b), respectively.

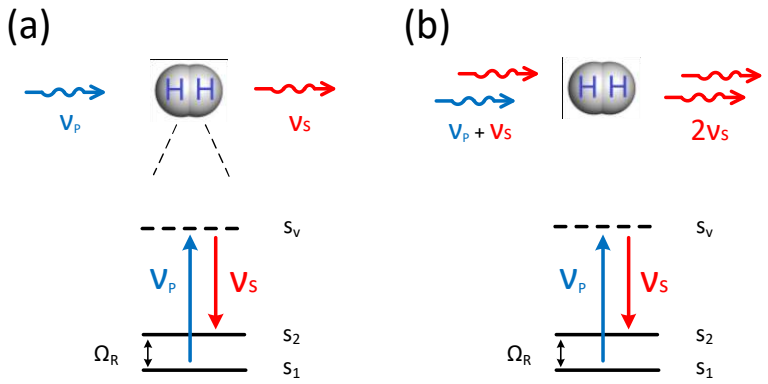

Fig. 4.1 A comparison between the processes of (a) spontaneous Raman scattering and (b) stimulated Raman scattering. The ν_p and ν_s are the optical frequencies of the pump and Stoke beams. The s_1, s_2 and s_v represent the lower, upper and virtual states of transition, respectively. The energy separation between the lower and upper states corresponds to an Raman shift of Ω_R.

The spontaneous Raman scattering is much weaker but is also simpler in realization compared with the SRS as only one pump beam is required. A bunch of Raman transitions can be simultaneously excited by the pump light, which makes the spontaneous Raman scattering quite convenient in obtaining the whole Raman spectrum of the substance under test. In addition, by measuring the ratio between the perpendicularly and parallelly polarized scattering components with respect to the polarization direction of the incident pump beam, the information of molecular symmetry can then be retrieved. The HC-PBF based spontaneous Raman scattering for trace gas detection has been reported [58-60]. Compared with the free space setup, the HC-PBF can substantially improve the Stokes signal due to the much longer interaction path as well as the larger Stokes photon collecting angel. However, for a certain transition line, the sensitivity of spontaneous Raman is limited, not only by the relatively small scattering efficiency but also by the less freedom in choosing modulation method, which, as illustrated in Section 2.4, can greatly enhance the SNR and thus sensitivity.

In order to improve the Raman scattering efficiency, method of SRS can be adopted, in which two beams of light called as pump and Stokes with their frequency difference matching the Ω_R are

injected into the sample simultaneously. The pump photons are converted into Stokes photons mediated by the molecular Raman transition with the differential energy left inside the molecule. Hence there will be a spectra-dependent gain or loss in the transmitted power of the Stokes or pump beam, which phenomena are known as the stimulated Raman gain (SRG) and stimulated Raman loss (SRL), respectively. Compared with the SRL, it is the relatively low-power Stokes beam that is detected in the gain method, so the SRS spectroscopy are commonly implemented based on the technique of SRG. The HC-PBF based SRS spectroscopy have been reported [64, 66]. The interaction between the molecules and the light beam with high intensity over long path is guaranteed by the HC-PBF fiber, resulting in much higher SRS signal compared with free space setup. However, the HC-PBF fiber based SRS spectroscopy has some inevitable drawbacks, such as the relatively large coupling loss between the HC-PBF fiber and the SMF transmission line [120], the difficulty in gas infusion [121] and the additional mode interference noise from the cladding modes [57]. Those problem are absent in nanofiber based SRS due to the adiabatic transition of the taper with low loss, the exposed evanescent field for convenient light-matter interaction and the single-mode operation.

4.1.2 Principle of nanofiber enhanced SRS

The detection scheme is based on seeded SRS but not noise-initiated SRS, so there is no threshold for SRS to happen. The SRG for the Stokes beam is proportional to the intensity of the pump beam, which under the assumption of constant pump intensity for trace Raman-active molecule can be expressed as [122]:

$$\frac{\Delta I_s}{I_{s0}} \sim g I_p L \propto \alpha A^{-1} P_p N L, \qquad (4.1)$$

where, g is the Raman gain factor; ΔI_s, I_{s0} and I_p are the increased Stokes beam intensity after transmission, initial Stokes beam intensity and pump beam intensity, respectively; L is the length of interaction; α is the fraction of the light power that can interact with the gas molecules and is

assumed to be the same for pump and Stokes beam; A is the mode field area of pump beam; P_p is the incident pump power; N is the molecular density. As seen, for the fixed pump level and interaction length, the SRS efficiency is directly proportional to the factor of αA^{-1}.

A comparison of α and A^{-1} among the cases of free space, HC-PBG fiber and nanofiber assuming a fixed interaction length of $1\,cm$ should contribute to a more concrete understanding. In the following, we only focus on the SRG technique with the case of S_{00} rotational Raman transition of hydrogen molecule, which has a Raman shift of $354.4\ cm^{-1}$. The notation of S_{00} may be described in detail that the symbol of 'S' means the difference in rotational quantum number $\Delta J = 2$, the first subscript represents the difference in vibrational quantum number and the second represents the initial rotational level. There is generally no need to give the initial vibrational level, as it is basically always the v_0 level governed by the Maxwell Boltzmann distribution. Then the notation of S_{00} represents the pure rotational Raman transition from $J' = 0$ to $J'' = 2$. For the free space Gaussian beam, it Rayleigh length can be regarded as the interaction length, in which the pump beam propagates without suffering from excessive divergence, as depicted in Fig. 4.2(a). The $1\,cm$ Rayleigh length corresponds to a waist diameter d_0 of > 100 μm at the near infrared band,

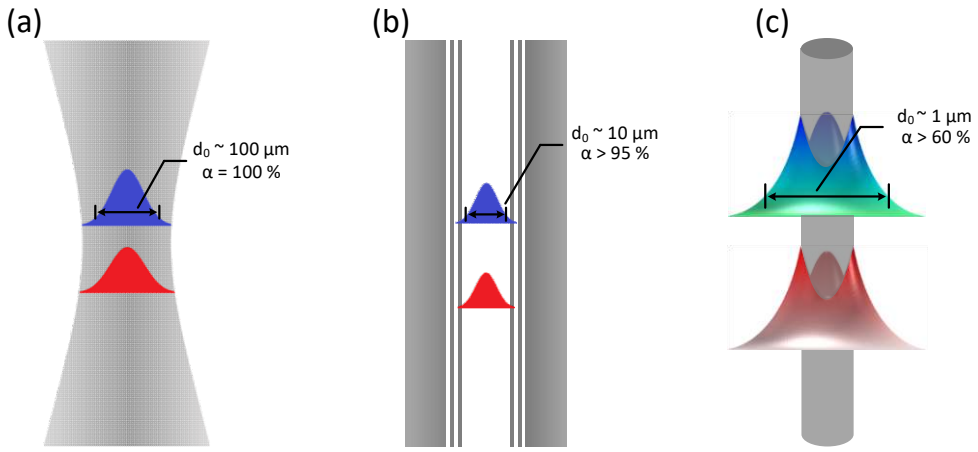

Fig. 4.2 Illustration of the SR spectroscopy in (a) free space Gaussian beam, (b) HC-PBG fiber, (c) optical nanofiber.

according to the relation as [123]:

$$d_0 = 2\sqrt{\frac{\lambda z_R}{\pi}}, \qquad (4.2)$$

where, z_R is the Rayleigh length. For the case of HC-PBG fiber shown in Fig. 4.2(b), both the pump and Stokes beams can be strongly confined in the central air hole with mode field diameters (MFD) of $\sim$10 μm and less than 5 percent of power leaked into the silica cladding [124]. So, compared with the free space, the HC-PBG fiber can offer at least two orders of improvement in Raman efficiency. It should be mentioned that although only a small portion of the light resides inside the cladding, it can still excite the Raman scattering of the silica material, which has a broad spectrum extending to $\sim$1000 cm^{-1} and may bring significant background signal from silica for the HC-PBG fiber based method, especially for the measurement of rotational Raman scattering, which has smaller Raman shift and thus overlaps with that from silica [58]. However, this problem may only exist in the scheme based on spontaneous Raman but not in the SRS one, because the wavelength modulation method can be readily adopted in the latter one to distinguish the sharp Raman line of gas molecules from even the overwhelming background, as will be demonstrated in detail later for the experimental part for nanofiber based SRS. For the nanofiber case, the MFD is further reduced. With properly chosen diameter of the nanofiber according to the wavelength of light beams adopted, the fraction of evanescent field can be over 60 % with the MFD less than 1 μm as shown in Fig. 4.2(c), resulting in another 2 orders of enhancement in Raman efficiency.

For the case of nanofiber, a balance between the portion of evanescent field and the light intensity which is inversely proportional to the mode field area should be taken into consideration for optimal Raman efficiency. Shown in Fig. 4.3 is a demonstration of the diameter dependent strength of SRS in nanofiber with different wavelength of pump beam as well as a demonstration of the much higher Raman efficiency in nanofiber over the state-of-the-art HC-PBG fibers. For a fixed set of pump and Stokes beams, a reduction in the diameter of nanofiber is always in favor of larger portion of evanescent field α. However, for much reduced diameter, the nanofiber would be too thin to

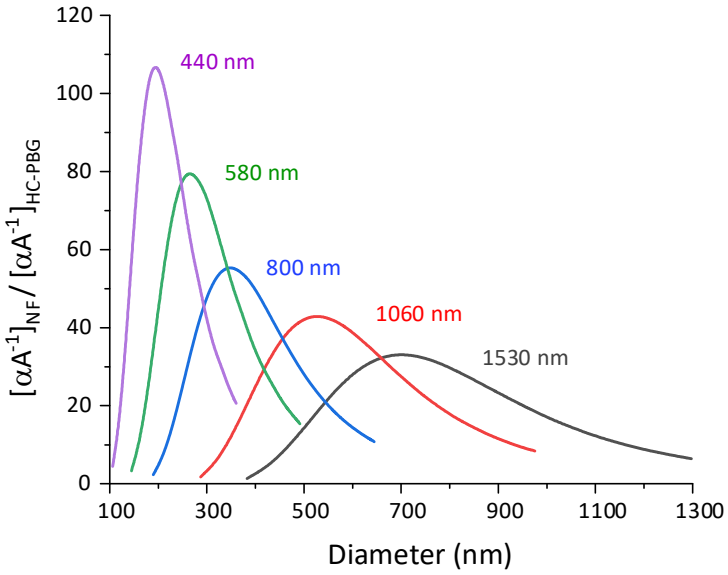

Fig. 4.3 Illustration of the enhancement of SRS efficiency in nanofiber over the HC-PBG fibers. The marked wavelength are for the pump beams and the corresponding wavelength of Stokes beams are all $354.4\ cm^{-1}$ longer to match the S_{00} transition. The αA^{-1} of HC-PBG fibers at those wavelength are calculated based on the datasheet of the HC-1550-02, 1060-02, 800-02, 580-02, and 440-02 from NKT Photonics with the MFDs of 9, 7.5, 5.5, 5.3 and 4 μm, respectively.

constrain the mode field and there will be a rapid increase in MFA A and hence a sharp drop in light intensity. So the Raman efficiency in nanofiber rapidly decrease for diameters less that the optimal one. The mode field areas of nanofibers are calculated using the Electromagnetic Waves module in Comsol Multiphysics, while the ones of hollow-core PBG fibers are obtained from the datasheets released by NKT Photonics. The αA^{-1} of light beams propagating along the nanofiber are much larger in the visible band than in the NIR band, due to the more tightly confined evanescent field and thus smaller A for shorter wavelength. However, in consideration of the commercialized high performance laser source and abundant optical components in the communication band as well as the advantages of fiber-optic sensing, experiments of nanofiber enhanced SRS spectroscopy are

still performed in telecom band.

4.2 Experiments of nanofiber enhanced SRS for trace hydrogen sensing

The silica nanofiber is still fabricated from the standard SMF (Corning SMF-28) using the flame brushing technique. The nanofiber has a diameter of about 700 nm and a waist length of 48 mm. The total transmission loss is less than 0.3 db. After fabrication, the nanofiber is immediately sealed into a gas cell, which has two vents installed with valves for gas inlet and outlet. The two pigtails of the nanofiber are left outside the gas cell for optical connection. The experimental setup is based on the method of SRG, as shown in Fig. 4.4.

The pump and Stokes beams are offered by the DFB laser and ECDL with their central wavelength of ~1532.83 and 1620.76 nm, respectively. The FWHM linewidth of pump and Stokes laser are 5 MHz and 300 kHz respectively, which are substantially less than the linewidth of SRS gain profile of the trace hydrogen of ~300 MHz. The differential frequency matches the S_{00} rotational Raman

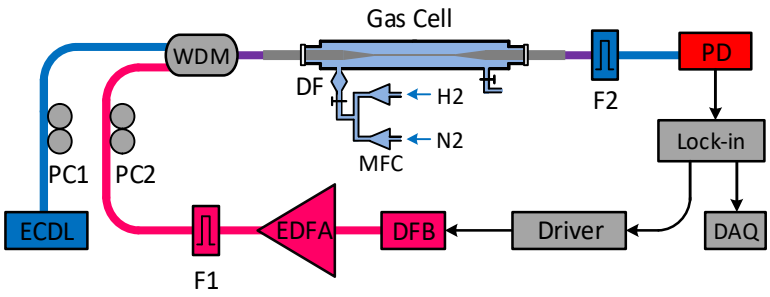

Fig. 4.4 Experimental setup of nanofiber enhanced SRS spectroscopy for hydrogen detection. F1, F2: optical filters; PC1, PC2: polarization controllers; DF: dust filter, which is used to eliminate the possible particles present in the gas mixture and prevent them from pollute the nanofiber sample; MFC: mass flow controller.

transition of hydrogen. Accompanying the slow ramp of the central wavelength of the pump beam across the transition line, there is also a fast sinusoidal wavelength modulation, which is quite necessary for distinguishing the sharp Raman transition line of hydrogen from the broad silica background, as depicted in Fig. 4.5. It should be mentioned that the silica background is a severe problem in the HC-PBG fiber enhanced spontaneous Raman scattering for trace gas sensing. Although there is only a small portion of the guided pump power residing inside the silica cladding, the meters long interaction path still results in considerable background signal from silica, which can totally submerge the Raman signal from the trace gas with low Raman shift. Inserting a pinhole between the output end face of the HC-PBG fiber and the photodetector can effectively reduce the background level, but it also attenuates the Raman signal from trace gas a lot [60]. However, the method of nanofiber enhanced SRS combined with WMS used here can effectively eliminate the background without a compromise in signal amplitude. The technique of WMS can also be used in HC-PBG fiber based SRS to eliminate the background Raman signal from the silica lattice cladding and hence to improve the SNR.

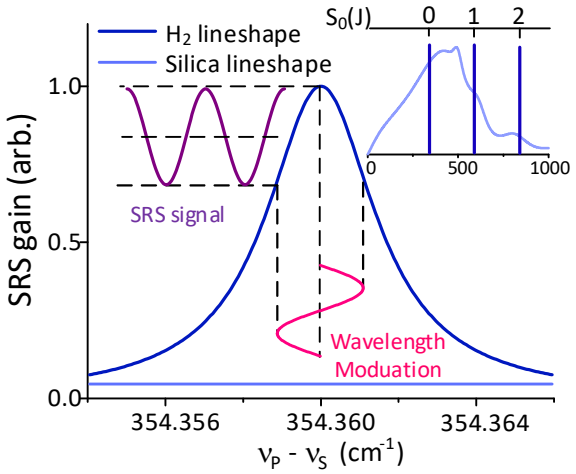

Fig. 4.5 The technique of wavelength modulation for the pump beam to distinguish out the sharp Raman transition line of hydrogen. Inset: other rotational Raman transition lines of hydrogen and the Raman spectrum of silica in a broader spectra range.

The optical filter F2 centers at the wavelength of Stokes beam to eliminate the pump light. The detected Stokes signal is then sent to the lock-in amplifier for second harmonic demodulation. Two polarization controllers are used to adjust and optimize the polarization states for both the pump and Stokes beams to achieve the largest amplitude of SRG signal. Gas samples with different concentration of hydrogen are obtained by mixing pure hydrogen and nitrogen through the mass

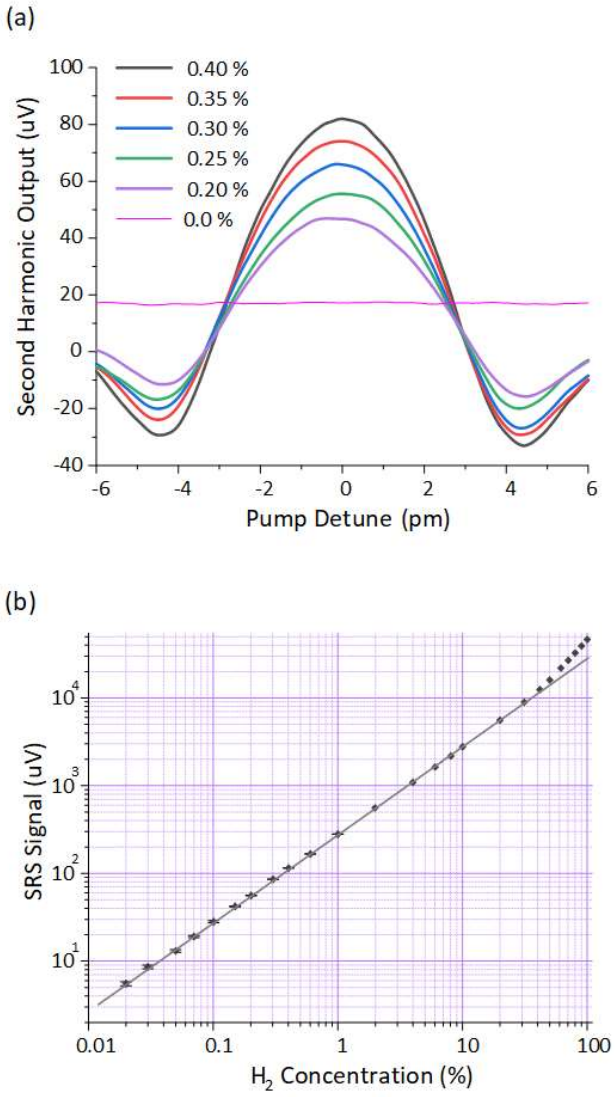

Fig. 4.6 Experimental results of (a) the second harmonic output and (b) SRS signal with different hydrogen concentration.

flow controllers (MFC). The smaller the flux of hydrogen, the lower its concentration. The dust filter (DF) installed at the inlet is for prevention of the possible particles mixed in the gas sample from contaminating the nanofiber. All the experiments are performed under atmospheric pressure.

The second harmonic output from the lock-in amplifier, whose time constant and roll-off are fixed respectively to be 10 s and 18 dB/Oct, for different concentration of trace hydrogen balanced by nitrogen under the same pump level of 305 mW are shown in Fig. 4.6(a). The wavelength of the pump beam is swept in a range of ± 6 pm with respect to 1532.83 nm at which the frequency difference between pump and Stokes beams matches the Raman shift of S_{00} transition. The peak-to-peak value of the second harmonic output is defined as the SRS signal, which is found to be linear with the hydrogen concentration not only in the range of 0.2 % to 0.4 % but also in a much larger range extended to about 50 %, as shown in Fig. 4.6(b). The deviation of the SRS signal from linearity in the higher concentration range originates from the reduced intermolecular collisional broadening effect which results in larger SRS gain coefficient. The noise level is evaluated as the standard deviation of the second harmonic output when the pump laser is swept across the transition line in the atmosphere of pure nitrogen, depicted as the pink line in Fig. 4.6(a). For a transmitted probe power of 0.38 mW, the noise is measured to be 0.25 μV. Compared with the measured SRS signal of 115 μV for the 0.4 % hydrogen, the SNR and noise equivalent lower detection limit are evaluated to be 460 and 8.7 ppm, respectively. In consideration of the 100 % upper limit of detection, a dynamic range as high as 5 orders has been achieved under a 305 mW pump power.

The linearity between the pump power and SRS signal is verified, as shown in Fig. 4.7(a). The SRS signal is measured under fixed hydrogen concentration of 0.4 % with the pump level varied from 115 mW to 305 mW. The noise level are also evaluated under each pump power. It is found that the amplitude of signal is proportional to the pump power but the noise is increasing at a shallower slope, so increasing the pump power should be an effective method to achieve higher SNR. The stability and ultimate sensitivity of current system is evaluated by analysis of Allan deviation. The pump wavelength is fixed at the line center with pure nitrogen inflated into the gas cell. The second

harmonic output of the lock-in with 100 ms time constant are recorded for two hours for analysis of Allan deviation. As shown in Fig. 4.7(b), the ultimate detection limit of 3 ppm can be achieved for an integration time of 260 s, beyond which the drift of the system makes further averaging no sense. The drift could originate from the variation of polarization states of both the pump and Stokes beams. The polarization sensitivity will be demonstration theoretically in later section as well as its possible solutions.

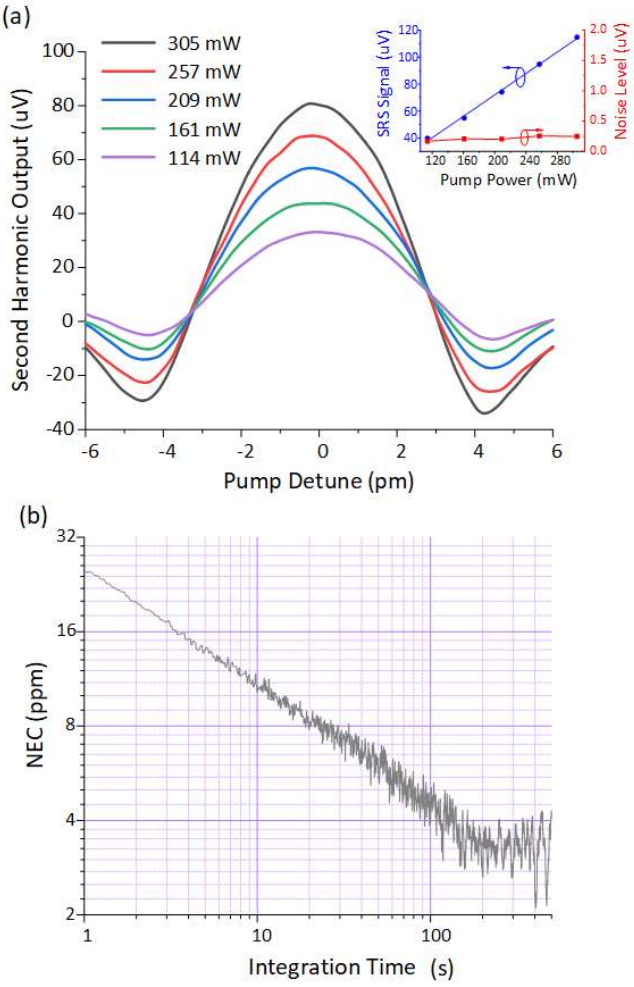

Fig. 4.7 Experimental results of (a) the second harmonic output under different pump level (b) Allan deviation analysis for evaluation of the noise equivalent lower limit of detection.

Another advantage of nanofiber based light-matter interaction is the easy accessibility to the evanescent field of the light beam which is exposed outside the silica core. It is expected that this nanofiber based hydrogen sensor should have fast responsibility. To measure the response time, the pump wavelength is fixed at the 1532.83 nm, whose differential frequency with respect to the Stokes beam corresponds to the center of S_{00} rotational transition. Then gas samples with hydrogen concentration of 0, 2, 4 and 0 %, which is obtained by adjusting the flux of hydrogen through the MFC with the one for nitrogen fixed meanwhile, are inflated into the gas cell successively. The detected SRS signal is shown in Fig. 4.8.

The response time (at which the signal reaches $1 - e^{-1}$ or e^{-1} for the inflation or recovery process) is measured to be less than 10 s, which is only limited by the size of the gas cell and the length of the gas pipe. A comparison of performance in regards of the lower limit of detection (LOD), Upper limit of detection (HOD) and response time can be found in Table 4.1. It can be found that the nanofiber one may be the most all-round technique. For the metallic coating based method, the larger response time results from the relative slow rate of chemical reaction. While for the hollow-core fiber based method, the small central core with diameter of several micrometers and meters-long fiber to be filled limited the response time when gases are loaded from the two ends.

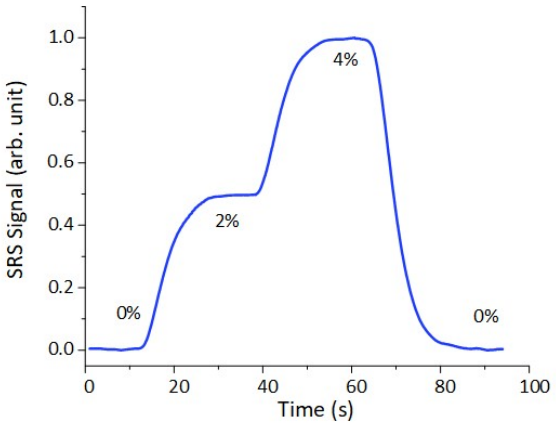

Fig. 4.8 Experimental results of response time measurement.

It is found in experiments that the SRS signal is polarization dependent, so two polarization controllers are used to optimize the polarization states as shown in Fig. 4.4. The slow drift of polarization states are always present due to the inevitable fluctuations in ambient temperature as

Table 4.1 A comparison of the performance in hydrogen sensing between the existing techniques and the nanofiber one in this work.

Techniques	Functional material	Sensing elements	LOD (ppm)	UOD (ppm)	Response time
MZI [125]	Palladium	Coated SMF	2	10^2	< 8 min
LPG [126]	Palladium	Coated LPG	5×10^2	1.6×10^5	< 7 min
FBG [93]	Palladium	Coated FBG	10^3	4×10^4	< 7 min
FPI [127]	Palladium	Coated FPI	32	5×10^4	< 70 s
SPR [128]	Palladium	Coated MMF	8×10^3	10^6	< 5 min
EWA [129]	Palladium	Coated MMF	2×10^3	6×10^3	< 60 s
SRSTL [130]	None	Thermal lens tube	9	5×10^5	N. A.
SRSPA [130]	None	Acoustic tube	4.6	5.6×10^4	N. A.
SR [59]	None	NKT HC-580-02 fiber	4.7	5×10^4	< 3 min*
SRG [64]	None	NKT HC-1550-02 fiber	17	10^6	< 4 h*
This Work	None	Silica nanofiber	3	10^6	< 10 s

LOD, lower limit of detection; UOD, upper limit of detection; MZ, Mach-Zehnder interferometer; LPG, long period grating; FBG, fiber Bragg grating; FPI, Fabry-Perot interferometer; SPR, surface plasma resonance; EWA, evanescent wave absorption; SRSTL, stimulated Raman scattering based on thermal-lens; SRSPA, stimulated Raman scattering based on photo-acoustic; SR, spontaneous Raman scattering; SRG, stimulated Raman gain spectroscopy. MMF, multimode optical fiber * The response time is obtained according to the dynamics of gas flow under the condition of 1 bar differential pressure between the two side holes [131].

well as the vibrations. This drift may be the main reason for a limited upper integration time of only 260 s. In the next section, this problem will be studied.

4.3 Polarization dependent SRS

The polarization sensitivity in the stimulated rotational Raman scattering has long been known. For the plane wave in free space, the ratio of rotational SRS gain for hydrogen among counter-directional circularly, parallelly, orthogonally and co-directional circularly polarized configuration is 6:4:3:1 [132]. While for the nanofiber case, due to the presence of the transverse components, the linearly or circularly polarized incident beams will not be purely transverse and thus the ratio of SRS gain among each polarization configuration is expected to be reduced, which may help suppress the polarization sensitivity. The imaginary part of the nonlinear polarization density could be expressed as [133]:

$$\vec{P}_{\omega_S}^{Im} = -A_c E_p^2 (E_s \vec{v}_s + E_{so} \vec{v}_{so}), with \begin{cases} A_c = \dfrac{2\pi^2 \varepsilon_0^2 n_p (J+1)(J+2)\gamma_{00}^2 \Delta N}{15 n_s (2J+1)(2J+3) h\Gamma} \\ \vec{v}_i = 3\vec{e}_p^*\left[\vec{e}_p \cdot \vec{e}_i\right] + 3\vec{e}_i\left[\vec{e}_p^* \cdot \vec{e}_p\right] - 2\vec{e}_p\left[\vec{e}_p^* \cdot \vec{e}_i\right] \end{cases}, (4.3)$$

where, ω_S is the angular frequency of the Stokes beam; E_p and E_s are the optical field amplitudes of incident pump and Stokes beams respectively; E_{so} is the field amplitude of the other fundamental mode generated from the Raman interaction and is orthogonal to the one excited by incident Stokes beam; ε_0 is the vacuum permittivity; n_p and n_s are respectively the RI of pump and Stokes beams in air; J is the rotational quantum number of the initial state and thus equals zero for S_{00} Raman transition; γ_{00} is the off-diagonal element in the polarizability matrix of the hydrogen molecule; ΔN is the differential molecular density between $J = 2$ and $J = 0$ levels and is temperature dependent; h is the Planck constant; Γ is the HWHM linewidth and is concentration dependent; $\vec{e}_p$, $\vec{e}_s$ and $\vec{e}_{so}$ are respectively the normalized vector fields of the pump and two degenerate Stokes beams. The polarization dependent gain originates from the term of $\vec{v}_i$, which has different value for different polarization configuration of pump and Stokes and is the largest when both the $\vec{e}_p$ and $\vec{e}_i$ are circularly polarized but with opposite direction. Getting the

polarization density into the wave propagation equation for Stokes beams, a coupled wave equation is obtained as:

$$\begin{cases} \dfrac{\partial E_s}{\partial z} = \dfrac{\omega_s^2}{2\beta_s \varepsilon_0 c_0^2}\left(c_{s,s}E_s + c_{so,s}E_{so}\right)E_p^2 A_c \\ \dfrac{\partial E_{so}}{\partial z} = \dfrac{\omega_s^2}{2\beta_s \varepsilon_0 c_0^2}\left(c_{s,so}E_s + c_{so,so}E_{so}\right)E_p^2 A_c \end{cases}, with\ c_{i,j} = \frac{\int_\rho^\infty (\vec{v}_i \cdot \vec{e}_j^*)ds}{\int |\vec{e}_j|^2 ds}, (4.4)$$

where, β_s is the propagation constant of Stokes beam, c_0 is the vacuum light speed; A_c is a factor as defined in Equ. (4.3); ρ is the radius of nanofiber. The wavelength of the pump and Stokes beams are selected to be 1532.8 and 1620.7 nm respectively, which matches the experimental parameters as in previous section. The simulation result is shown in Fig. 4.9:

The dimension of the gain coefficient is $cm^{-1} \cdot W^{-1} \cdot ppm^{-1}$, means the incremental power of the output Stokes beam over the input one, per centimeter long nanofiber, per watts of incident pump

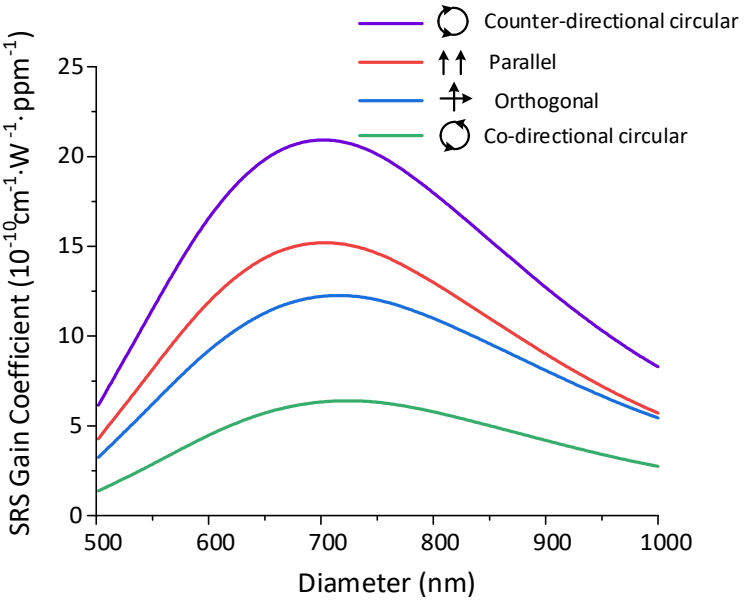

Fig. 4.9 Theoretically calculated result of the normalized SRS gain for various value of nanofiber diameter with four different configurations of the polarization states of pump and Stokes beams.

power, which is assumed to be a constant along propagation, per ppm hydrogen surrounding the nanofiber. It is found that the ratio of gain between the four different polarization states are diameter dependent and are 3:2.1:2:1, 3.3:2.4:1.9:1 and 5.6:3.8:2.8:1 for diameters of 1000, 700 and 400 nm, respectively. It can be seen, for larger diameter the polarization dependence of SRS gain is less, while with reduced diameter, the situation gets worse. For the nanofiber of 400 nm diameter, the ratio are quite close to 6:4:3:1 as in the free space case. This is quite reasonable as the thinner the nanofiber, the closer its mode field property approaches the free space one. The overall polarization states of the guided modes in the nanofiber can neither be a pure linearly nor circularly polarized state, but is a mixed one. This fact, to a certain degree, helps to relief the polarization dependent gain. For the 700 nm-diameter nanofiber, although the polarization sensitivity is about two times reduced compared with free space, the slow drift of polarization states of pump or Stokes beams can still cause a variation in the signal amplitude as large as 300 % at most, as is observed in experiments when the polarization states of both the pump and Stokes beams are adjusted by the two polarization controllers. So, for real application, besides the nanofiber degradation should be prevented, both the power and polarization states of the pump and Stokes laser are required to be kept stable.

It is worth mentioning that the nanofiber itself should not be the source of polarization drift. Nanofibers tapered from the circularly symmetric standard SMF with waist of centimeters long can preserve the polarization state of the input light beam, as long as it is pull straightly. Actually, even an obvious bending in the nanofiber still has a limited influence on the polarization of the propagating light beam [134].

The dominant stress in a bending fiber is the longitudinal one denoted as σ_z, which has respectively a tensile and a compressive effect on the outer ($x > 0$) and inner side ($x < 0$) of the bent cylinder, as shown in Fig. 4.10(a). However, due to the odd-function property of the σ_z, it does not modify the effective RI of the guided fundamental mode, but contribute to the bending induced birefringence through the Poisson effect that a longitudinal strain is always accompanied with

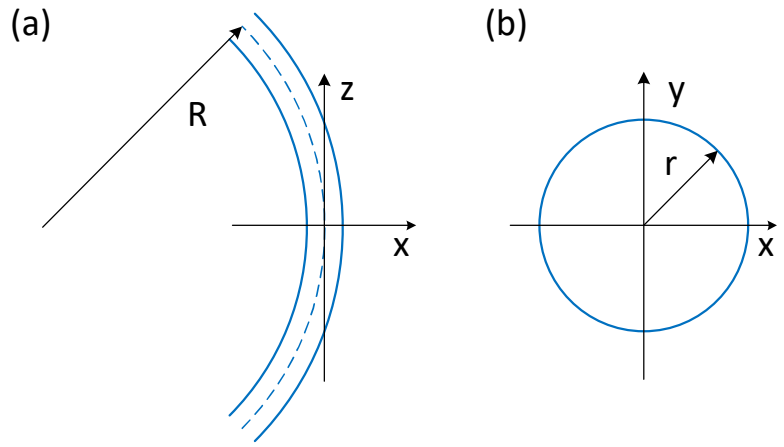

Fig. 4.10 Geometric deformation of bent nanofiber in the (a) top view and (b) front view.

transverse ones as σ_y and σ_z. For a bended fiber, its cross section, as shown in Fig. 4.10(b), tends to contract and expand in the outer and inner parts, respectively. The quadruple symmetric y-directional transverse strain σ_y has no contribution to the birefringence for the same reason as σ_z. However, the σ_x is an even function across the section and finally modifies the refractive index. The resulting birefringence due to bending is expressed as [134]:

$$\Delta n_{eff} = \frac{1}{4R^2} n_{eff} n_s^3 (p_{11} - p_{12})(1+\nu) r^2, \qquad (4.5)$$

where, R is the radius of curvature, n_s is the RI of silica, p_{11} and p_{12} are the strain optic coefficients and equal to 0.11 and 0.25 respectively, ν is the Poisson ratio and equals 0.15 for fused silica, r is the cross-sectional radius of nanofiber. For a 700 nm-diameter nanofiber operating at 1.55 μm and bent in a curvature of 1 cm, the Δn_{eff} is calculated to be only 1.5×10^{-10}, which is basically negligible. However, for the bare SMF curved with the same radius of 1 cm, the Δn_{eff} is 6.7×10^{-6}.

Although the polarization is barely changed during propagation along the nanofiber even under severe curvature, the polarization of the relatively long SMF link still cannot be guaranteed. There

may be two possible solutions, one is to use a polarization scrambler to perturb the polarization state of the pump or Stokes beam so that the polarization dependent gain can be averaged out, and the other is to replace the circular shaped nanofiber with a highly-birefringent (Hi-Bi) one. However, if the second method is adopted, all the optical components in the system should also be replaced with the polarization maintaining counterparts. Although the nanofiber is not sensitive to the stress birefringence, it does sensitive to the shape birefringence, which is just the opposite to the weakly guiding SMF. As an example, for the given 1 % core ellipticity of a 700 nm-diameter nanofiber and SMF, the Δn_{eff} of the two orthogonally polarized fundamental modes for a 1.55 um propagating light beam are 6.1×10^{-4} and 7.8×10^{-8}, respectively. Based on the shape birefringence sensitivity, Hi-Bi microfibers have been successively fabricated from either a polarization maintaining fiber or a non-circular SMF with parts of the cross section cut away using the femtosecond laser or ablated by CO2 laser [135, 136].

4.4 Summary

The nanofiber enhanced SRS for high-sensitivity and fast-response hydrogen sensing is demonstrated. The high-sensitivity originates from the large SRS gain as well as the single-mode operation of the nanofiber. With a piece of 48 mm long and 700 nm-diameter silica nanofiber, the trace hydrogen detection limit as low as 3 ppm is achieved. Benefit from the exposed evanescent field, the response time of the nanofiber hydrogen sensor is as short as several second, which can be further reduced by more compact design of the gas cell. The problem of polarization sensitivity is investigated, which will cause long-term drift of the system. It is anticipated that by using the polarization scrambler to average out each polarization states or by replacing both the nanofiber and optical link with hi-bi ones, the problem of polarization drift may be solved.

Chapter 5 Line broadening effects in nanofiber based spectroscopy

In this chapter, the transit time broadening effect is studied, which may not be an important issue in free space but does become prominent in the nanofiber based spectroscopy. At first, a qualitative description from the view of a single molecule is given. Then, the quantitative treatment by the density matrix method is demonstrated. The theory is verified by the experiments of nanofiber based absorption spectroscopy of pure acetylene. The conclusion is made that for trace acetylene detection at the atmospheric pressure, the transit time broadening in the nanofiber is of the same order as the Doppler broadening and is negligible compared with the dominant collisional broadening. However, the situation becomes quite different for the nanofiber based stimulated Raman spectroscopy.

5.1 A qualitative description – based on the classical oscillator

Intuitively, the transit time broadening can be an analogy of the time-bandwidth product in the optical pulses or the delay-bandwidth product in the communications, in both of which the shorter the duration of a signal the larger the bandwidth in frequency domain. In a classical view, the molecule inside the light beam could be viewed as a forced oscillator driven by the optical field [97], as:

$$\ddot{x} + \gamma\dot{x} + \omega_0^2 x = c_f E_0 e^{i\omega t}, \qquad (5.1)$$

where, x is the displacement of electron or nucleus within the molecule, γ is the damping constant, ω_0 is the natural frequency of transition, c_f is the force constant and E is the amplitude of the optical field. This forced oscillation with damping has the well-established solution in the form as $x = x_0(\omega)e^{i\omega t}$, where the $x_0(\omega)$ is the amplitude of oscillation. The magnitude of the real and imaginary part of the complex amplitude $x_0(\omega)$ in response to the different driving

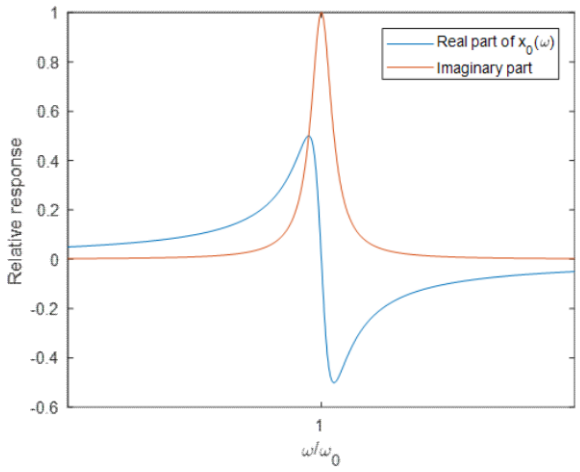

Fig. 5.1 Real and imaginary part of the complex amplitude of a damped oscillator under different driving frequency.

frequency are depicted as the blue and orange line in Fig. 5.1 respectively.

For the absorption spectroscopy, the real part, which is responsible for the dispersion, can be just dropped, and the remaining imaginary part is then expressed as:

$$x_0''(\omega) = \frac{\gamma\omega \cdot c_f E_0}{(\omega_0^2 - \omega^2)^2 + \gamma^2\omega^2}, \qquad (5.2)$$

As seen in Equ. (5.2), the response is related to both the damping constant and the detuning of the incident light relative to the center of transition line. For a molecule with transverse velocity v_{tr} traversing through the waist of a Gaussian beam which has a spatial field distribution of $E_G = E_0 e^{-r^2 \cdot w^{-2}}$, it will feel a time dependent amplitude of the driven field as:

$$E = E_0 e^{-\frac{v_{tr}^2}{w^2}t^2}, \qquad (5.3)$$

where, the distance r in Gaussian field is just replaced by $v_{tr}t$. Then the constant field amplitude E_0 in Equ. (5.1) should be substituted by Equ. (5.3). However, this new form of field amplitude

cannot be directly solved, which makes the Fourier series expansion necessary, where the time dependent driving electric field is decomposed into a series of single frequency signal with frequency of ω_{tr} and amplitude of $exp\left(-\frac{w^2}{4v_{tr}^2}\omega_{tr}^2\right)$, as:

$$E = \frac{E_0 w}{2\sqrt{\pi}v_{tr}} \int exp\left(-\frac{w^2}{4v_{tr}^2}\omega_{tr}^2\right) e^{i\omega_{tr}t}\, d\omega_{tr}, \qquad (5.4)$$

Then the response of the single molecule driven by the optical field, taking into consideration the transversal movement through the mode field can be written as:

$$x_0''(\omega) = \frac{E_0 w}{2\sqrt{\pi}v_{tr}} \int \frac{c_f \gamma(\omega + \omega_{tr})\, exp\left(-\frac{w^2\omega_{tr}^2}{4v_{tr}^2}\right)}{[\omega_0^2 - (\omega + \omega_{tr})^2]^2 + \gamma^2(\omega + \omega_{tr})^2} d\omega_{tr}, \qquad (5.5)$$

The absorption line shape function $\psi(\omega)$ is just proportional to the $x_0''(\omega)E_0^{-1}c_f^{-1}$ as given in Equ. (5.5). It can be seen that the above equation is nothing but just a convolution between the Lorentzian and the Gaussian line shapes, which describes the collisional/natural broadening and the transit time broadening in the Gaussian field, respectively. Considering the fact that the optical frequency ω and ω_0 are basically much larger than these two broadening factors γ and $v_{tr}w^{-1}$, the line shape function is then simplified as:

$$\psi(\omega) = \frac{w}{8\sqrt{\pi}v_{tr}\omega_0} \int \frac{c_f \gamma\, exp\left(-\frac{w^2\omega_{tr}^2}{4v_{tr}^2}\right)}{[\omega_0 - \omega - \omega_{tr}]^2 + \gamma^2} d\omega_{tr}, \qquad (5.6)$$

It should be mentioned that the Gaussian shape in the integral above originates from the limited time of light-matter interaction for the molecule traversing the waist of the Gaussian beam, rather than from the Doppler effect. Moreover, what we are discussing is the lineshape of a single molecule and it is unreasonable to talk about the Doppler broadening, which naturally is a description of the behavior of an ensemble of molecules with a range of velocity distribution in the direction of light propagation. The convolution above can be much simplified under two conditions, i.e., the collisional broadening dominant and the transit time broadening dominant, for both of which, the

two line shapes are decoupled. When the collisional broadening dominates, i.e., $\gamma \gg v_{tr}w^{-1}$, the Lorentzian shape is regarded as a factor and thus can be extracted out of the integral, leaving a simple integration of the Gaussian, as:

$$\psi(\omega) = \frac{1}{4\omega_0} \cdot \frac{\gamma}{(\omega_0 - \omega)^2 + \gamma^2}, \qquad (5.7)$$

which is actually the same as described by Equ. (5.2). For the other case where transit time broadening dominates, i.e., $\gamma \ll v_{tr}w^{-1}$, the Equ. (5.6) can then be expressed as:

$$\psi(\omega) = \frac{\sqrt{\pi}w}{4\omega_0 v_{tr}} \cdot exp\left(-\frac{w^2}{4v_{tr}^2}(\omega_0 - \omega)^2\right), \qquad (5.8)$$

An illustration of the pure transit time broadening effect experienced by a molecule which has a constant transverse velocity of $300\, m \cdot s^{-1}$ and traverses through the one-dimensional Gaussian beam with different waist diameter is shown in Fig. 5.2. As seen, the narrower the beam diameter, the wider the linewidth. For a single molecule traversing the one-dimensional Gaussian beam with negligible collisional broadening, the expression for the transit time linewidth can be expressed as:

$$\Gamma_{tr} = \frac{v_{tr}}{\pi w}\sqrt{0.5\, ln\, 2}, \qquad (5.9)$$

where, Γ_{tr} is the HWHM linewidth in Hz, which is proportional to the transverse velocity of the molecule as well as the inverse of the mode field diameter. Although it is the case of Gaussian beam based on which the transit time effect is discussed, the degree of transit time broadening for arbitrarily shaped mode field, including the evanescent one, is enough to be estimated. For the gas molecules probed by the light beam with mode field diameter of d, at which the intensity drops to e^{-2} of the maximum, the pure Γ_{tr} is around $0.5v_{mp}d^{-1}$, where v_{mp} is the most probable velocity.

The method based on the classical model works well for the case of singe molecule. However, when there are bunch of molecules present, the classical model would not be as simple as its first sight.

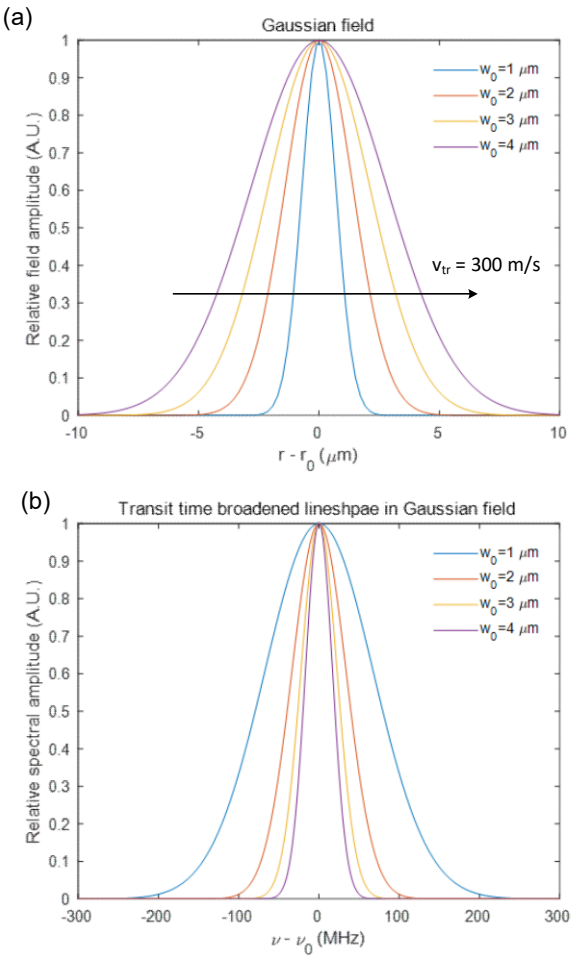

Fig. 5.2. Illustration of transit time broadening effect for a molecule traversing through the optical field with different mode field diameter.

In the next section, the more capable density matrix method is adopted, so that the collisional, Doppler and transit time broadening effects can be systematically included.

5.2 A quantitative treatment – based on density matrix method

A two-level system, as shown in Fig. 5.3, is used to describe the absorption. A specific case can be the $P(13)$ line of the $v_1 + v_3$ vibrational transition at 1532.83 nm. If there is no optical field, the

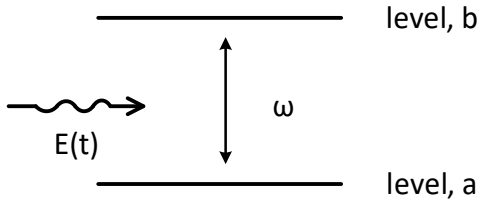

Fig. 5.3. Illustration of a molecular two-level system.

molecules are unperturbed and stay in either the lower level $|\psi_a\rangle$ or the upper level $|\psi_b\rangle$, definitely, with the population determined by MB statistics. While the presence of the optical field, with $\omega = \hbar^{-1}(E_b - E_a)$, perturbs the molecular Hamiltonian and results in a superposition of the two eigenstates. According to Equ. (2.19), the total wave function is then a linear combination of these two eigenstates with time dependent coefficients as:

$$\Psi = a(t)|\psi_a\rangle\, exp(-i\omega_a t) + b(t)|\psi_b\rangle\, exp(-i\omega_b t)\,, \qquad (5.10)$$

where, the normalization requires that $aa^* + bb^* = 1$ and the angular frequency ω_a and ω_b equals $E_a\hbar^{-1}$ and $E_b\hbar^{-1}$, respectively. Then the density matrix can be expressed as:

$$\rho = \begin{bmatrix} \rho_{aa} & \rho_{ab} \\ \rho_{ba} & \rho_{bb} \end{bmatrix} = \begin{bmatrix} aa^* & ab^*\, exp[-i(\omega_a - \omega_b)t] \\ ba^*\, exp[-i(\omega_b - \omega_a)t] & bb^* \end{bmatrix}, \qquad (5.11)$$

where, the diagonal terms aa^* and bb^* are the probability that the molecule is found to be in the lower and upper level, respectively. The evolution of ρ, taking into consideration of the molecular movement, is governed by the equation of motion as [137]:

$$i\hbar\left(\frac{d}{dt} + \vec{v}\cdot\nabla\right)\rho = \left[\hat{H}_0 + \hat{V}, \rho\right] + i\hbar R(\rho - \rho_0), \qquad (5.12)$$

where, $\vec{v}$ is the molecular velocity, $\hat{H}_0$ is the unperturbed molecular Hamiltonian, $\hat{V}$ is the perturbation from optical field, R is the relaxation rate, ρ_0 is the unperturbed diagonal density

matrix, with the off-diagonal elements representing the relative population between the two levels. It is the first order perturbation of the off-diagonal elements $\rho_{ab}^{(1)}$ and $\rho_{ba}^{(1)}$ that is responsible for the linear absorption. Actually, the two off-diagonal elements are a complex conjugation pair, so only one of them needs to be handled. Therefore only the $\rho_{ab}^{(1)}$ is of concern, which could be expressed as:

$$\left(\frac{d}{dt}+\vec{v}\cdot\nabla\right)\rho_{ab}^{(1)}=-(\gamma_{ab}+i\omega_{ab})\rho_{ab}^{(1)}-(i\hbar)^{-1}\vec{\mu}_{ab}\vec{E}n_{ab}F(\vec{v}), \qquad (5.13)$$

where, γ_{ab} is the collisional dephasing rate and is proportional to pressure, $\vec{\mu}_{ab}$ is the transition dipole, $\vec{E}$ is the two dimensional mode field, n_{ab} is the differential population density between upper and lower levels, $F(\vec{v})$ is the MB velocity distribution function. According to the rotating wave approximation, the above equation is then simplified as:

$$\vec{v}_{tr}\cdot\nabla_{tr}\rho_{ab}^{(1)}=i\left(\omega_p-\omega_{ab}-k_z v_z\right)\rho_{ab}^{(1)}-\gamma_{ab}\rho_{ab}^{(1)}-(i\hbar)^{-1}\vec{\mu}_{ab}\vec{E}n_{ab}F(\vec{v}), \qquad (5.13)$$

where, ω_p is the angular frequency of the incident probe beam, $\vec{v}_{tr}$ is the transversal velocity, k_z is the wave vector of the z-directional propagating probe beam. In the optical field with a detune of $\omega_p-\omega_{ab}$, for each group of molecules with a specific velocity of $\left(v_x,v_y,v_z\right)$, there will be a unique spatial distribution of $\rho_{ab}^{(1)}$, the integration of whose multiplication with the optical field over the mode field area is proportional to the power attenuation of the propagating beam. The partial differential equation above can be numerically solved using, such as the finite difference method or the finite element method, with the boundary condition as zero $\rho_{ab}^{(1)}$ at the surface of nanofiber. For a single molecule, its velocity and direction is unpredictable, but the velocity distribution for the whole molecular system follows the MB distribution indicated as $F(\vec{v})$ in Equ.(5.13). The dephasing rate γ_{ab} is related with the pressure in bar p as:

$$\gamma_{ab}=2\pi\zeta p, \qquad (5.14)$$

where ζ is the self-collisional broadening coefficient and equals to $4.3\ GHz \cdot bar^{-1}$ for the P(13) line of acetylene.

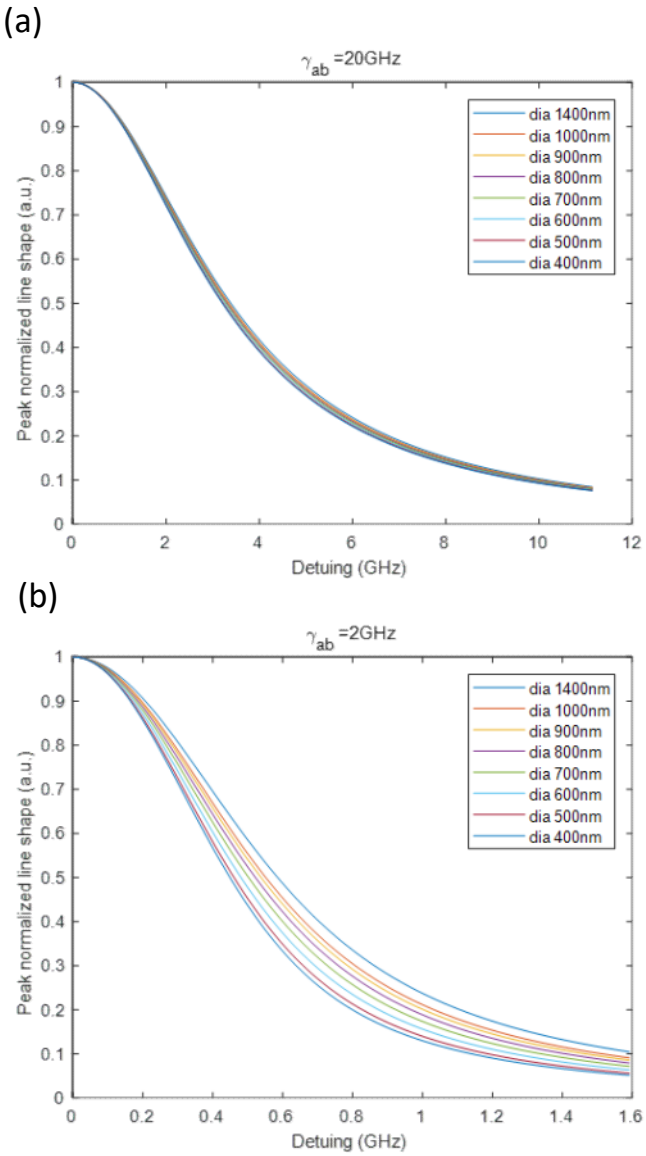

Fig. 5.4. Simulated line shape function for nanofibers of different diameters with collisional dephasing rate of (a) 20 GHz and (b) 2 GHz, respectively.

A series of simulations are performed on silica nanofiber with diameters ranging from 400 to 1400 nm in pure acetylene atmosphere at the room temperature. As shown in Fig. 5.4 are the results of line shape functions with $\gamma_{ab} = 20\ GHz$ and $2\ GHz$, corresponding to a pressure of 741 and 74.1 mbar, respectively.

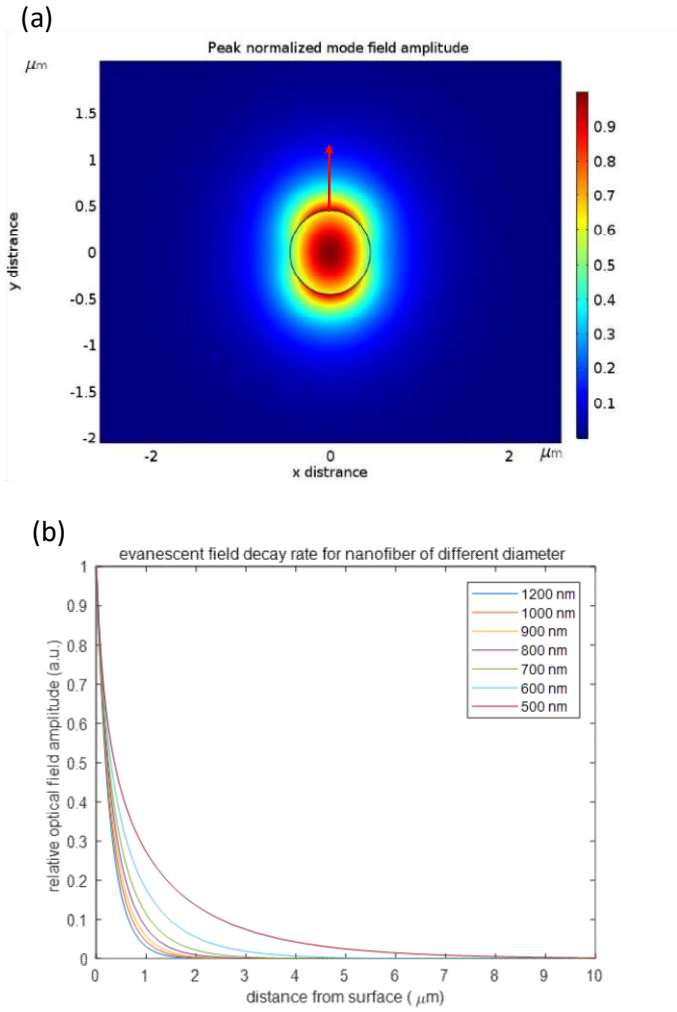

Fig. 5.5 Illustration of the different decay rate of the evanescent field associated with the silica nanofiber of different diameter. The curves in (b) is the normalized amplitude of the optical field along the arrow in (a).

It is seen from Fig. 5.4 (a) that for the relatively larger pressure range, the collisional broadening effect dominates, and the line shape is basically a Lorentzian with barely seen diameter dependent linewidth. However, when the pressure drops to 74.1 mbar, the line shape function for nanofibers with different diameter deviate from each other, as shown in Fig. 5.4 (b). The line width decreases with reduced diameter, which is reasonable and can be demonstrated with the aid of Fig. 5.5.

As seen in Fig. 5.5(b), the larger the diameter of the nanofiber, the tighter the evanescent field is attached to the surface. In the more tightly confined evanescent field, a molecule with constant velocity approaching or leaving the silica surface will then feel a faster change of the electric field, which results in a broader line shape. According to Equ. (2.28), for the P(13) line of acetylene at room temperature, the HWHM Doppler linewidth Γ_{dop} is calculated to be about 240 MHz. The collisional broadening can be suppressed by reducing the pressure. The pure Doppler broadening effect is only determined by the z-directional molecular movement and should not depends on the geometric configuration. So the change of line shape function with different diameter of the nanofiber is solely caused by the transit time effect. The collisional broadening free lineshape is investigated under the pressure of 10^{-5} bar, on which condition the inter-molecular collisional

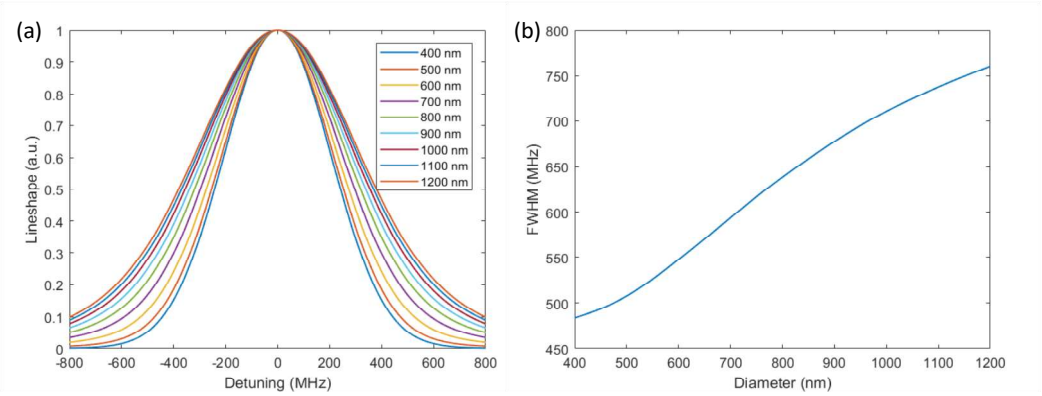

Fig. 5.6 (a) The lineshape and (b) FWHM linewidth of the collisional broadening free case for nanofibers with different diameters.

broadening is negligible. The simulated lineshape and the full-width-half-maximum (FWHM) linewidth for nanofibers of different diameters are shown in Fig. 5.6.

If it is supposed that the transit time effect is basically negligible for the 400 nm-diameter nanofiber, then the ratio between the contributions from the Doppler and the transit time effect is evaluated to be about 3:1 for a 1000-nm silica nano/microfiber. So, for the nanofiber based absorption spectroscopy as well as the photothermal and photoacoustic ones, the transit time effect is negligible in ambient conditions. The pure transit time broadened lineshape can be obtained by setting the z-

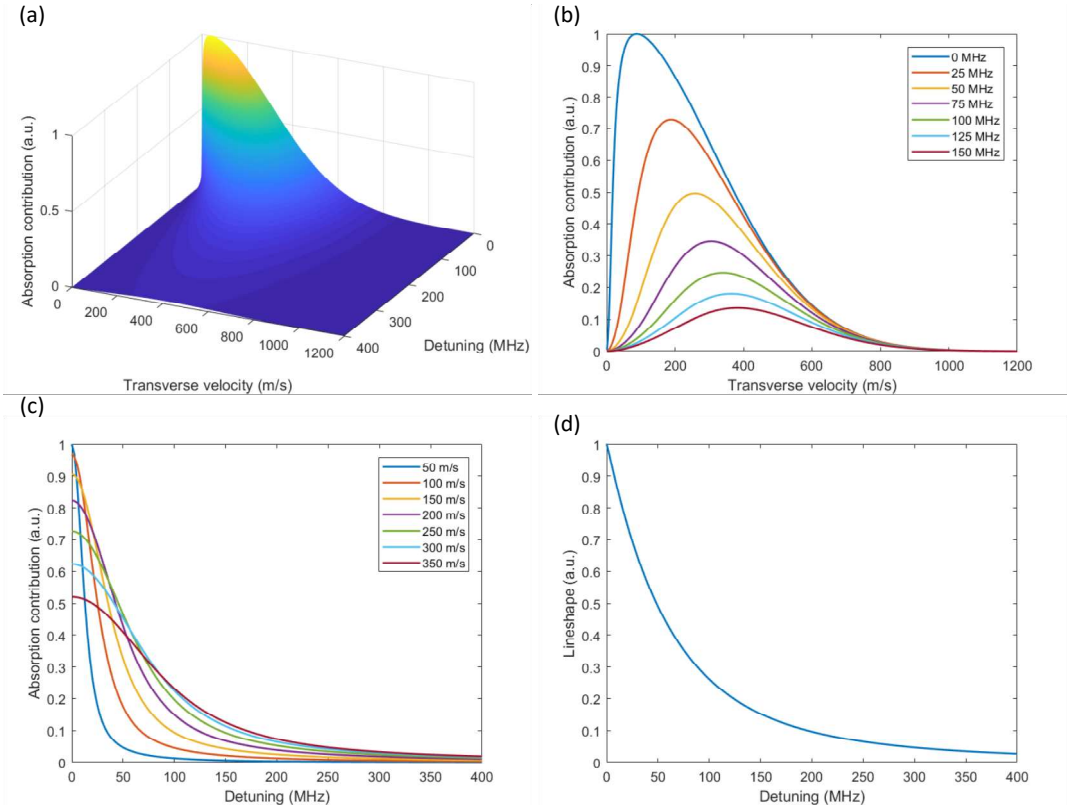

Fig. 5.7 Simulation results of the pure transit time broadening for a 700-nm-diameter nanofiber. (a) Peak normalized relative absorption contribution for different transverse velocity and detuning, (b) Slices of (a) with different detuning, (c) Slices of (a) with different velocity, (d) Pure transit time broadened line shape for an ensemble of molecules.

directional molecular velocity as zero. Each transverse molecular velocity sub-group $v_{tr} = \sqrt{v_x^2 + v_y^2}$ will has different distribution of $\rho_{ab}^{(1)}$ as well as different contribution to the total attenuation to the guided probe beam. Shown in Fig. 5.7(a) is the peak normalized relative absorption contribution from different transverse molecular velocity sub group with varied detuning relative to the center of the transition line. The larger transverse velocity groups contribute more to the absorption for larger detuning relative to the center of transition line, as shown in Fig. 5.7(b) and 5.7(c). The overall lineshape due to the pure transit time broadening for the 700-nm-diameter nanofiber is shown in Fig. 5.7(d).

The linewidth of transit time broadening is reduced for thinner nanofiber due to the enlarged mode field and thus the increased light-matter interaction time. The simulated lineshape and FWHM linewidth of the pure transit time broadening for nanofibers of different diameter is shown in Fig. 5.8(a) and 5.8(b), respectively.

The sharp lineshape of the transit time broadening is quite different from the typical Lorentzian or Gaussian functions, and was experimentally observed by Hendrickson, et al in the experiments of

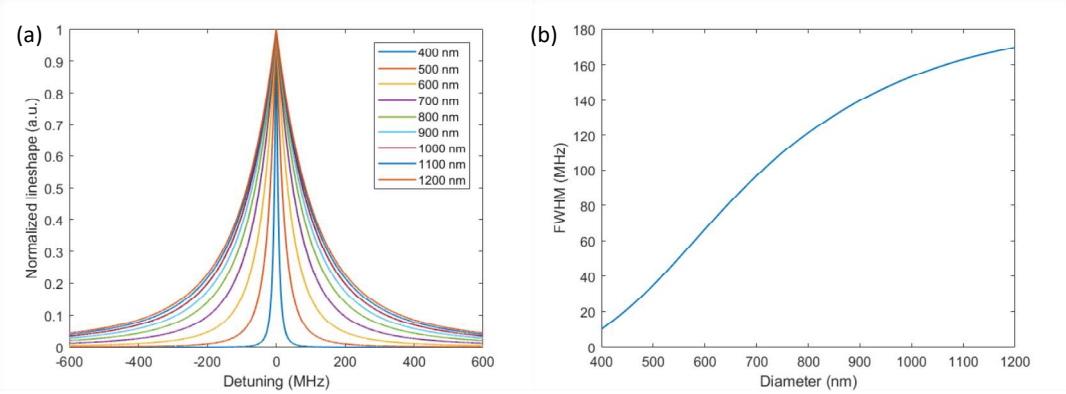

Fig. 5.8 Simulation results of (a) lineshape and (b) FWHM linewidth of pure transit time broadening for different diameter of nanofiber.

nanofiber based two photon absorption, which is of Doppler free so that the pure transit time broadened lineshape can be directly observed [138].

5.3. Experimental measurement of linewidth of acetylene

The above simulation is verified by experiments based on measurement of the P(13) line of acetylene at 1532.83 nm. The experimental setup is shown as Fig. (5.9). A single frequency, narrow linewidth (< 5 MHz) probe beam is offer by the DFB. An optical attenuator is used to prevent saturation of the photodetectors. It is then split into two beams with power ratio of 1:1 by the optical coupler C1. The upper beam is for measurement of absorption. Intensity modulation with frequency of 30 kHz is used to improve the SNR and thus the precision of measurement. After probing the acetylene gas sample, it is detected by the photodetector PD1, with the signal demodulated by the lock-in amplifier afterwards. The signal generator (SG) is used to generate the driving signal for AOM and offer the reference frequency for the lock-in amplifier. Accompanying the intensity modulation, the central wavelength of DFB is slowly swept across the P(13) line so that the whole

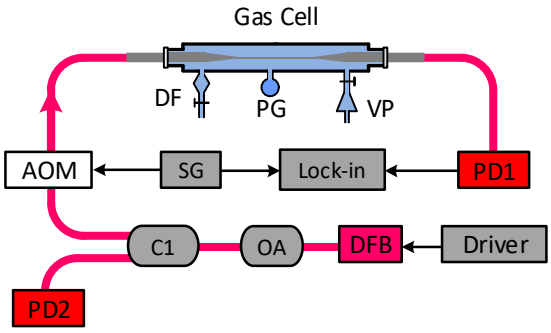

Fig. 5.9 Experimental setup for measurement of the line shape of pure acetylene with different pressure. C1: 1:1 optical coupler; PD1: photodetector 1 for signal detection; PD2: photodetector 2 for signal normalization. OA: optical attenuator, typically 10 db; VP: vacuum pump; PG: pressure gage.

line shape can be obtained. The lower beam is used to monitor the spectrum dependent output power of the DFB. The absorption signal dividing this reference one helps eliminate the non-uniform spectrum background. Pure acetylene is inflated into the gas cell through the dust filter, which is actually not necessary but does help eliminate any potential pollutant and thus make the system more reliable. A mechanical vacuum pump (VP) is used to change the pressure inside the gas cell, which is monitored by a pressure gage (PG). The lowest pressure that can be achieve in this system is about 0.2 kPa. For a 1020nm-diameter nanofiber, the measured absorption profile with different acetylene pressure can be seen in Fig. 5.10.

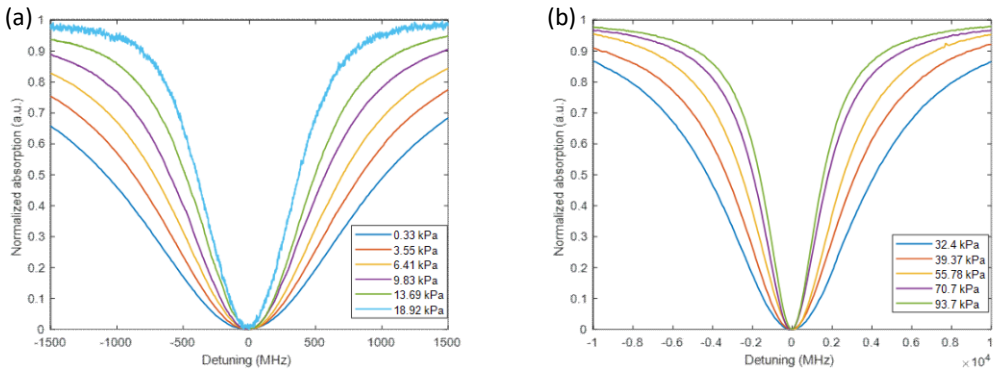

Fig. 5.10 The experimentally measured normalized absorption profile for a 1020 nm-diameter optical nanofiber in the (a) lower and (b) higher pressure range.

The experimentally measured results of the linewidth of acetylene with 1020, 770 and 580 nm-diameter nano/microfiber under different pressure in shown in Fig. 5.11. For comparison, the results of linewidth measurement in free space based on a collimator pair with beam diameter of 0.5 mm is also presented. As seen, in the higher pressure range (30 kPa), the linewidth will be collisional broadening dominant which is proportional to the pressure and there will be no difference between cases of nano/microfiber and free space. While in the lower pressure range, the linewidth will be Doppler and transit time broadening limited. For the free space case, there is generally no transit time effect due to the orders of larger size of the beam waist. So the difference in linewidth between

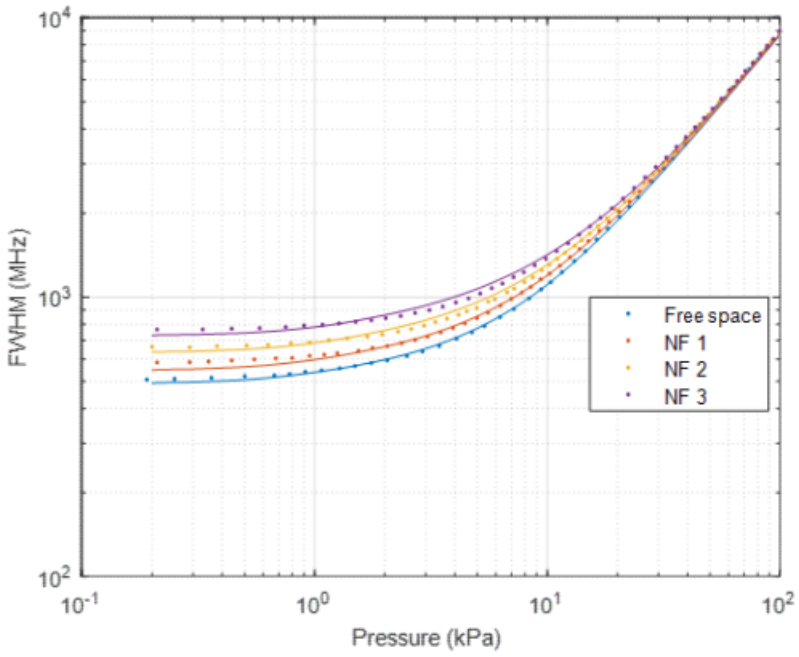

Fig. 5.11 The experimentally measured (dots) and simulated (solid lines) linewidth of P(13) line of acetylene in cases of 1020 , 770 and 580 nm-diameter nanofiber and free space. NF1, NF2 and NF3 are nanofibers with diameter of 580 , 770 and 1020 nm.

the cases of nanofiber and free space setup in lower pressure range, should originate from the transit time effect.

The Doppler broadening can be much alleviated using the Doppler-free saturation absorption spectroscopy (DFS) [139-141]. Generally, a pair of counter propagating light, i.e., pump and probe beams, with same frequency is adopted in DFS. These two beams will act on the same groups of molecules with the molecular longitudinal velocity approaching to zero when the optical frequency is turned to the line center. Then the high power pump causes saturation for the probe beam which is indicated as a reduction of absorbance around the line center. However, the DFS is not capable to reduce the transit time effect. The most straightforward method to alleviate the transit time broadening is by expanding the mode field area [142]. However, this method is contradictory with

Table 5.1 Collisional broadened linewidth in air for the relatively strong transition lines of common gas molecules around telecom band [143].

Molecule	Line position (nm)	Line strength ($\frac{cm^{-1}}{molecule \cdot cm^{-2}}$)	$\Gamma^{H}_{col,air,atm}$ (GHz)
C_2H_2	1532.83	1.04×10^{-20}	2.31
H_2O	1364.69	1.86×10^{-20}	2.83
HF	1304.53	5.50×10^{-20}	2.52
HCN	1528.04	7.06×10^{-21}	3.23
NH_3	1501.75	4.15×10^{-21}	3.05
CH_4	1650.96	1.52×10^{-21}	1.92
H_2S	1578.13	1.40×10^{-22}	2.48
CO_2	1432.04	6.03×10^{-23}	2.26
N_2O	1517.12	2.38×10^{-23}	2.32
CO	1568.03	2.16×10^{-23}	1.80
NO	1358.90	9.76×10^{-25}	1.68

one of the most important advantage of using nanofiber, i.e., the high intensity due to the constrained evanescent field. Fortunately, the absorption coefficient of common gas species at atmospheric pressure in telecom band is mainly determined by the collisional broadening, whose magnitude is orders higher than the transit time effect associated with the nanofiber.

Listed in Table 5.1 are the collisional broadened linewidth of the relatively strong transition lines of some common molecule at the telecom band. As seen, the collisional linewidth for the trace molecules in air at atmospheric pressure is of several gigahertz, which is about one order higher than the Doppler effect, not to say the transit time effect. However, the situation may not be the same for the stimulated Raman spectroscopy on the nanofiber platform especially for the hydrogen molecules.

5.4 Transit time effect in SRS of hydrogen

In the previous chapter, the nanofiber enhanced SRS for high-sensitivity hydrogen sensing has been

demonstrated under atmospheric pressure. There are some unique properties of hydrogen making its pressure dependent SRS linewidth more complex compared with the absorption spectroscopy of acetylene, as introduced above. First, hydrogen is the lightest molecules, which means its thermal velocity is the highest. Compared with the acetylene, the hydrogen is 3.6 times faster in mean velocity. So, the pure transit time broadening Γ_{tr}^{H} for hydrogen may be just roughly scaled up and thus estimated to be 150 MHz for a 700 nm-diameter nanofiber.

However, this faster thermal velocity does not result in higher Doppler broadening. Different from the absorption spectroscopy, in which the molecule only interacts with one beam of light, there are two beams of light adopted in SRS and it is the differential wave vector between the pump and Stokes that the Raman active molecule feels. Then, the HWHM Doppler linewidth in forward SRS is expressed as [144]:

$$\Gamma_{dop}^{H} = \frac{\nu_p - \nu_s}{c}\left(\frac{2N_A kTln2}{M}\right)^{\frac{1}{2}}, \qquad (5.15)$$

Where, ν_p and ν_s are respectively the optical frequency of pump and Stokes. For the S_{00} rotational Raman transition of hydrogen at room temperature, the Γ_{dop}^{H} is calculated to be about 46 MHz, which is about 5 times less that the P(13) line of hydrogen.

In addition to the character of high thermal velocity, the rotational Raman transition of hydrogen is of very low self-collisional broadening coefficient ζ_{col}, which is only $42\ MHz \cdot bar^{-1}$ resulting in a narrow collisional linewidth Γ_{col}^{H} of 42 MHz at the atmospheric pressure. Actually, the Doppler broadening for hydrogen is much suppressed when the pressure is larger than $0.1\ bar$, due to the Dicke narrowing effect. A analytical expression for the combination of Doppler and collisional broadening is as [145]:

$$\Gamma_{cd}^{H} = \frac{4\pi^2 \nu_R^2 D_0}{p} + \zeta_{col} p, \qquad (5.16)$$

where, ν_R is the differential wavenumber between pump and Stokes beam, and equals to

$354\ cm^{-1}$ for S_{00} Raman transition for hydrogen; D_0 is the self-diffusion coefficient and is $1.19\ cm^2 \cdot bar \cdot s^{-1}$ at room temperature. So, the combination of Doppler and collisional broadening linewidth Γ_{cd}^{H} is evaluated to be $48\ MHz$, which is about three times less than the pure transit time broadening Γ_{tr}^{H} in a 700 nm-diameter nanofiber. So, different from the absorption spectroscopy, the transit time effect is not negligible but the dominant broadening factor in SRS. A preliminary experiment with a 700 nm-diameter nanofiber indicates that the linewidth is increased to $119\ MHz$ under atmospheric pressure.

5.5 Summary

The transit time broadening in nanofiber is investigated. Due to the tightly confined mode field associated with the nanofiber, the molecules traverse the evanescent field fast with limited light-matter interaction time. It is found that the transit time effect diminishes with reduced diameter of the nanofiber. Generally, for the direct absorption spectroscopy based on optical nanofiber, the transit time broadening is at least three times less than the Doppler broadening in the near-infrared. As the collisional broadening dominates over the Doppler effect at atmospheric pressure for the common infrared-active molecules in this band, the transit time effect can be neglected for practical sensing application. However, the situation is much different for the SRS of hydrogen in nanofiber. The combination of faster molecular velocity, intrinsically low collisional broadening and the suppressed Doppler effect for the rotational Raman transition makes the transit time effect the dominant broadening factor on the nanofiber platform even at the atmospheric pressure.

Chapter 6 Transient birefringence induced by photothermal dynamics in nanofiber

In this chapter, the transient birefringence originating from the photothermal dynamics in nanofiber is studied. In the first section, the mechanism of the photothermal dynamics induced transient birefringence in nanofiber is described. Then the theory is verified by the numerical simulation. Based on the theory, an application of all-optical fast polarization switching is demonstrated. Presented at last is the discussions about methods of enhancement of the switching time.

6.1 Mechanism of the photothermal dynamics induced transient birefringence in nanofiber

In chapter 3, the nanofiber enhanced PTI spectroscopy was studied, where the energy absorbed by the surrounding trace molecules from the evanescent field of the pump beam will be released into heat which then results in a temperature rise of the waveguide and thus modulates the phase of the propagating beam. The experiments were performed with modulation frequency of tens of kilohertz to achieve the optimal SNR and thus the sensitivity. However, the relatively low modulation frequency makes the transient phenomena associated with heat generation as well as the thermal conduction inaccessible. Actually, the heat is generated in the surrounding air, while the dominant phase modulation originates from the heated silica. The linearly polarized fundamental mode of the pump has a two-fold rotational symmetric intensity distribution, which means the heat source and thus the initial temperature rise are not circularly symmetric, as shown in Fig. 6.1. This non-circular temperature distribution will then result in birefringence through the thermo-optic effect. Due to the negative thermo-optic coefficient of air, the change of temperature and RI are on the contrary. So, the direction where the overall intensity of the pump is higher corresponds to the fast axis, while the other corresponds to slow axis, as shown in Fig. 6.1(b).

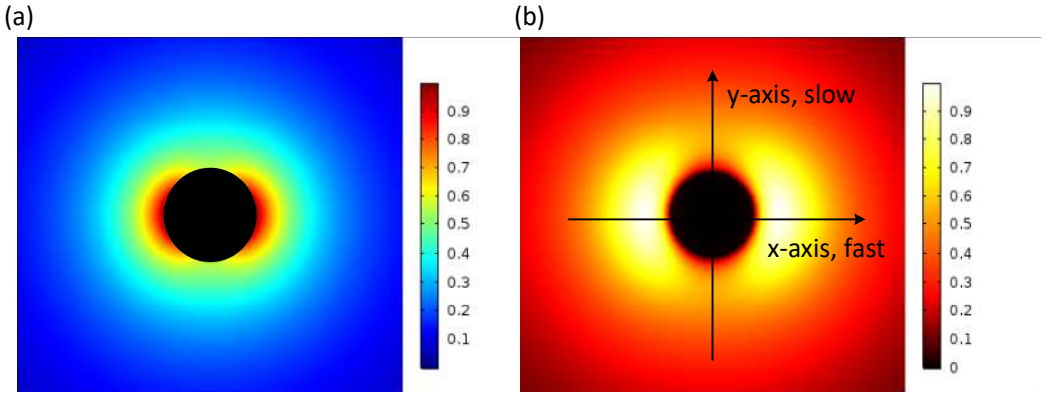

Fig. 6.1 Illustration of the mechanism of the photothermal dynamics induced transient birefringence in nanofiber. (a) The normalized intensity distribution of the $HE_{11,x}$ fundamental mode, where the mode field inside the silica has been omitted. (b) The unevenly distributed whole temperature field caused by the two-fold rotational symmetric heat source. The mean RI along the x-direction is lower than the y-direction, resulting in a fast and slow axis.

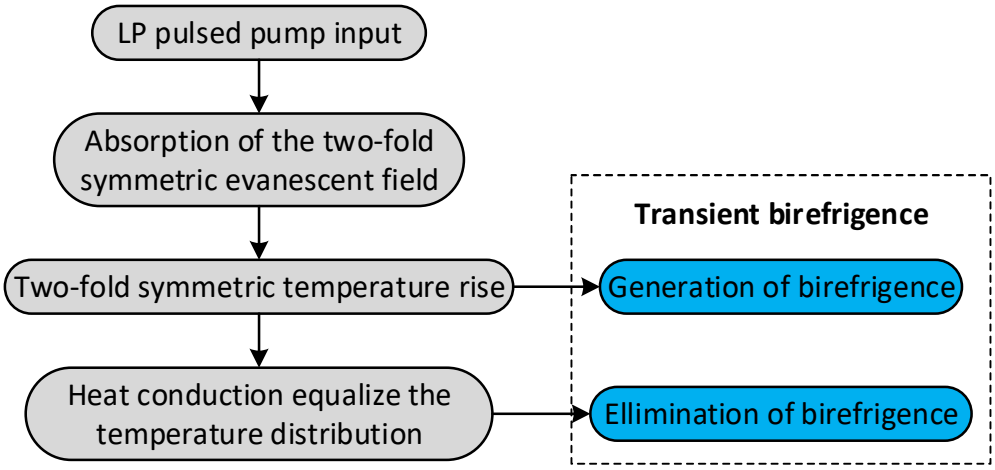

Fig. 6.2 Diagram of the main steps of generation of transient birefringence induced by the dynamic PT in nanofiber.

As the thermal conduction is inevitable, the temperature gradient tends to be smoothed gradually, which then results in a decrease in the birefringence. So, intuitively, the dynamic photothermal induced birefringence can only exist in the pulsed mode. It can be speculated that the rising time of the birefringence is limited by the thermal relaxation (heat generation) rate of the molecule. The magnitude of the birefringence should be determined by the maximum differential temperature between the two axes. While the falling time is limited by the rate of heat conduction. The diagram for the main processes in the transient birefringence induced by the dynamic PT in nanofiber is shown in Fig. 6.2. In the next section, series of numerical simulations are performed to verify the theory of transient birefringence following the same methodology as given in section 2 of chapter 3 but with a moderate modification to fit the pulsed mode of operation.

6.2 Numerical simulations for the transient birefringence in nanofiber

There are still three main steps to get the transient birefringence due to the PT effect in the nanofiber. First, the fundamental mode of the pump is calculated whose evanescent field serves as the heat source. Then the temperature evolution is obtained by solving the heat transfer equation for pulsed pump excitation. But different from the simulations in chapter 3 where the low-frequency sinusoidal modulation makes the thermal relaxation process not necessary, the temperature evolution under pulsed mode as adopted here is highly dependent on the relaxation time. The heat source Q in Equ. (3.2) should then be modified as:

$$Q(r,\theta,t) = \alpha A_{eff}^{-1} I_{ne}(r,\theta) \int P_{pump}(t') h(t-t') \cdot dt', \qquad (6.1)$$

where, the convolution above is the heat generation function, $P_{pump}(t)$ is the time dependent power of the pulsed pump, $h(t)$ is the thermal relaxation function, which can be expressed as:

$$h(t) = \tau_v^{-1} e^{-\frac{t}{\tau_v}}, \qquad (6.2)$$

where, τ_v is the vibrational relaxation or heat generation time and equals to $74\,ns$ for the

acetylene under room temperature and atmospheric pressure [146]. It should be mentioned that the τ_v is inversely proportional to the pressure with fixed temperature. For the rectangular shaped pump with width of t_w, the heat generation function $S(t)$ has a simple analytical expression as:

$$S(t) = \begin{cases} P_{pump}\left[1 - exp\left(-\frac{t}{\tau_v}\right)\right], & for\ 0 \le t \le t_w \\ P_{pump}\left[1 - exp\left(-\frac{t_w}{\tau_v}\right)\right] exp\left(-\frac{t - t_w}{\tau_v}\right), & for\ t > t_w \end{cases}, \qquad (6.3)$$

An illustration of $S(t)$ for a rectangular shaped pump with the unitary pump power and a fixed pulse width of 10 ns, but different relaxation time τ_v is shown in Fig. 6.3.

As seen in Fig. 6.3, the faster the thermal relaxation, the more concentrated in time for the heat source. Generally, the transient birefringence prefers a faster thermal relaxation, so that the nonuniform temperature distribution can be established without suffering much from the heat conduction process, which tends to eliminate the nonuniformity in temperature distribution as time

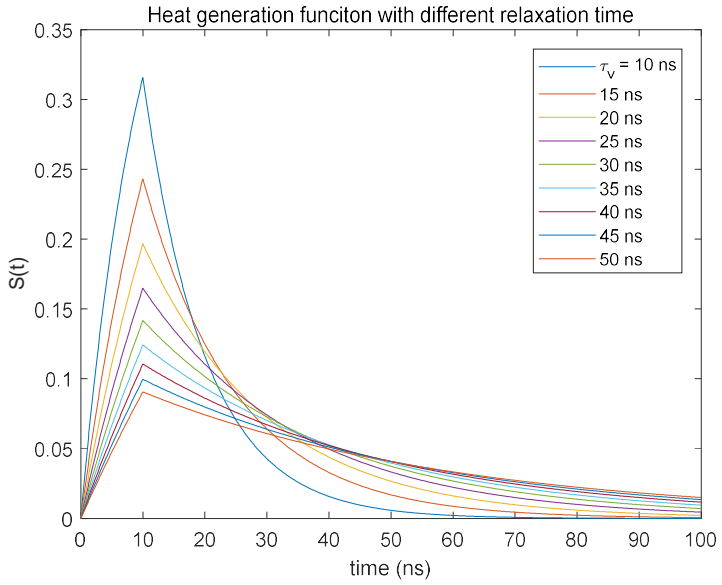

Fig. 6.3 Response of the heat generation function $S(t)$ with time under different thermal relaxation time τ_v.

goes by.

With this modified heat source, the RI evolution can be gotten from the change of temperature distribution along time, from which a pair of non-degenerate fundamental modes are resulted. In the following part of this section, the simulation will be performed by assuming the heating gas as pure acetylene with its P(13) line at 1532.83 nm adopted for optical excitation. The pump beam has a rectangular time domain waveform with a fixed pulse energy of 5 nJ but variable pulse width and an accommodated peak power. The nanofiber is assumed to have a waist diameter of 600 nm with negligible propagation loss. The linearly polarized pump beam will only excite one of the degenerate HE_{11} mode. Considering the pure acetylene used here, the absorption coefficient α in Equ. (6.1) should only be determined by the pressure. However, because the collisional broadening is the dominant one for the relatively high pressure range as will be adopted here, the increase in absorbance due to the presence of more absorbing molecules is just neutralize by the decrease in absorption cross section per molecule, which results in an basically unchanged absorption coefficient with pressure of $0.57\ cm^{-1}$. However, although the absorption coefficient and thus the power of heating source is unchanged, the higher pressure still appeals to higher birefringence due to the faster heat releasing speed.

The first series of simulations is conducted with pure acetylene of 10 bar. The pulse width is assumed to be 10 ns and thus the pulse power is set to $0.5\ W$, corresponding to a pulse energy of $5\ nJ$. The distribution of the change of temperature ΔT at the time points of 5 , 10, 15, 20, 30 and 40 ns are shown in Fig. 6.4.

It should be mentioned that the simulation of temperature evolution has excluded the silica core, which is represented by the transparent circle in the center. The interface between the acetylene and silica is just assumed to be of constant temperature, making the silica core working as a simple heat sink. This simplification is valid considering such a short piece of time of concern that there is no enough time for the silica core to be heated up. A rough estimation is enough to demonstrated this

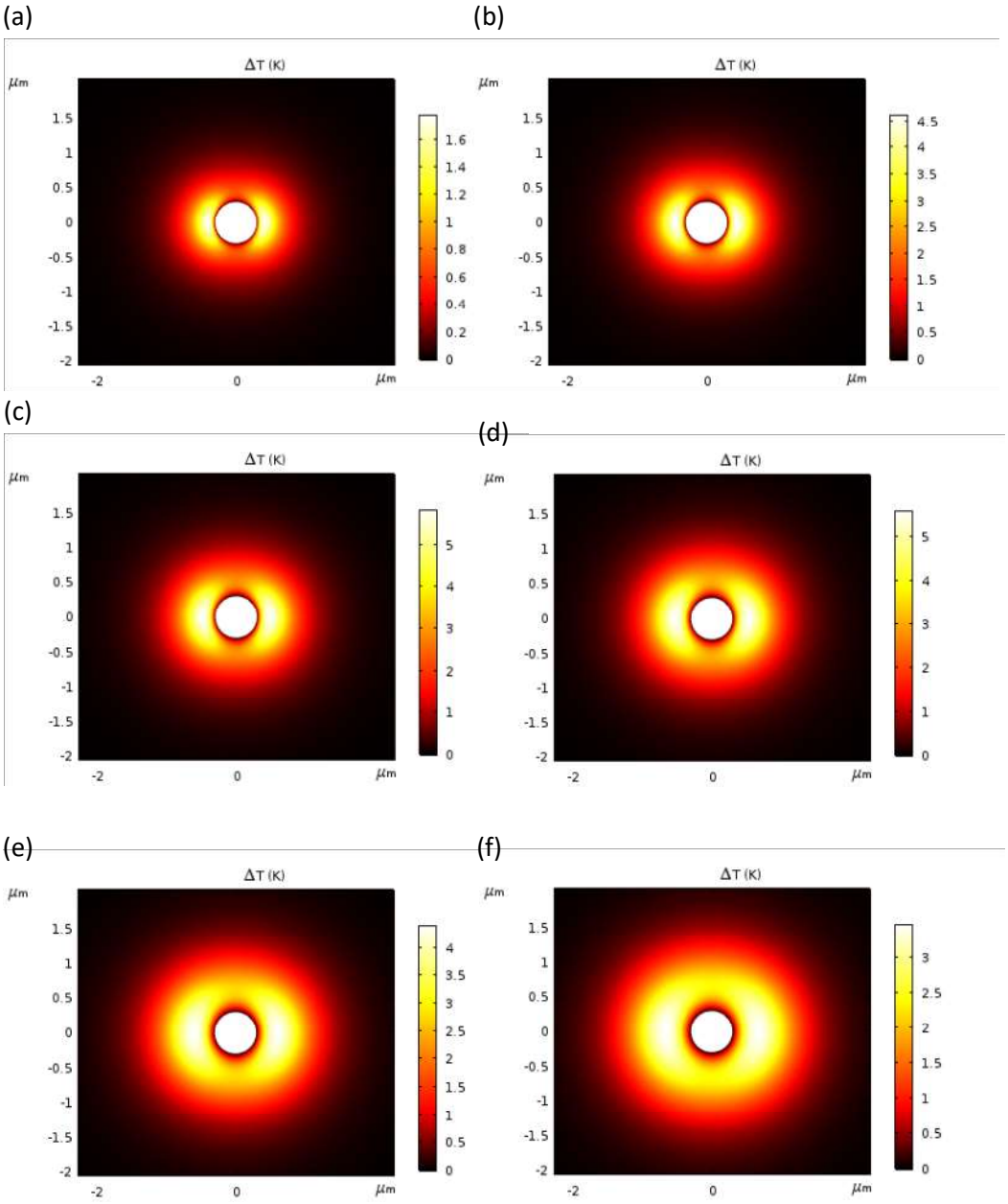

Fig. 6.4 The evolution of the temperature distribution at time point of 5, 10, 15, 20, 30 and 40 ns after the pulsed pump is on.

simplification. Supposing a constant differential temperature ΔT of $5\ K$ between the acetylene and silica, then the rate of temperature rising for the silica under a typical heat transfer coefficient of $h = 50\ W \cdot m^{-2}K^{-1}$ for the interface will be:

$$\delta T_s = \frac{h \cdot \Delta T \cdot 2\pi r_s}{\pi r_s^2 \cdot \rho_s \cdot C_s} = 1.1 \times 10^3\ K \cdot s^{-1}, \qquad (6.4)$$

where, r_s, ρ_s and C_s are the radius, density and specific heat capacity of the silica nanofiber respectively. Then for the time interval of 100 ns of concern, the temperature rise of the silica is at most of $\Delta T_s = 0.11\ mK$, which is negligible. In addition, due to the fast heat conduction within the silica, the core of nanofiber is basically of a uniform temperature, making its contribution to the birefringence even less. So, the silica core is just treated as out of the domain of definition with a constant temperature boundary condition defined on the surface.

Some qualitative explanations for the results as shown in Fig. 6.4 can be given here. Considering the pulse width of 10 ns, the optical excitation ceases at the time point when the Fig. 6.4(b) is snapshotted. However, the overall temperature keeps rising until 30 ns, as shown in Fig. 6.4(c) and (d). This originates from the time delay between pump absorption and vibrational relaxation, and it is the latter one that causes temperature rise. Due to the inevitable thermal conduction, the heat spot expands and the maximum differential temperature on a circle embracing the nanofiber decreases with time. Another interesting point is that accompanying the expansion of heat spot, the highest temperature point gradually moves far away from the nanofiber. This should originate from the heat sink effect of the silica nanofiber. Although the heating power is maximal near the surface of the silica, the heat loss rate is also the highest there, due to the largest temperature slop, especially when the overall temperature has reached a high level.

Actually, it is only in the region tightly surrounding the nanofiber that the temperature change contributes to the modification of the mode index. In addition, it is only the differential temperature on a circle surrounding the nanofiber that contributes to the birefringence. A qualitative method for evaluation of the birefringence is to find the amplitude of temperature variation on a circle that is just close to the surface of silica. Plotted in Fig. 6.5 is the relative temperature variation (with the DC part removed) on a circle that is $0.25r_s$ (75 nm) away from the surface of the nanofiber, at the

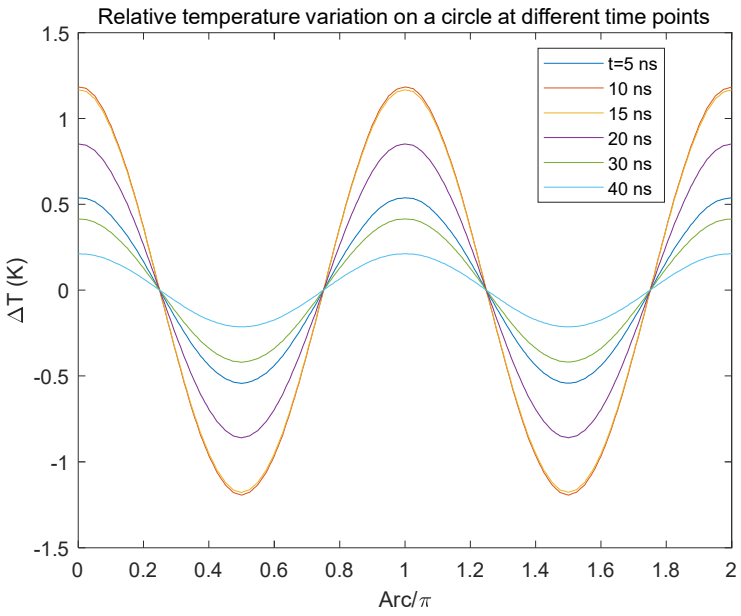

Fig. 6.5 Relative temperature variation on a circle $0.25r_s$ (75 nm) away from the surface of nanofiber at time points of 5, 10, 15, 20, 30 and 40 ns after pulse on.

time points corresponding to (a) to (f) in Fig. 6.4.

It is quite clear from the Fig. 6.5 that it is basically when the pulse is shut down that there is the highest temperature variation on a circle close to the nanofiber and thus the highest birefringence approximately. This further affirms the proposition that the transient birefringence is basically irrelevant to the size of the heat spot as well as the overall temperature rise.

It should be mentioned that the relation between temperature and RI is no longer linear for large temperature change. It is better to directly use the gas density to calculate the RI change:

$$n = 1 + (n_0 - 1)\frac{\rho}{\rho_0}, \qquad (6.5)$$

where, n_0 and ρ_0 are the RI and density at atmospheric pressure as well as room temperature and

equal to $1 + 5.5 \times 10^{-4}$ and $1.1\, kg \cdot m^{-3}$ for the pure acetylene, respectively. The density distributions at the time point of 5 , 10, 15, 20, 30 and 40 ns, corresponding to the (a) to (f) in Fig. 6.4 are shown in Fig. 6.6.

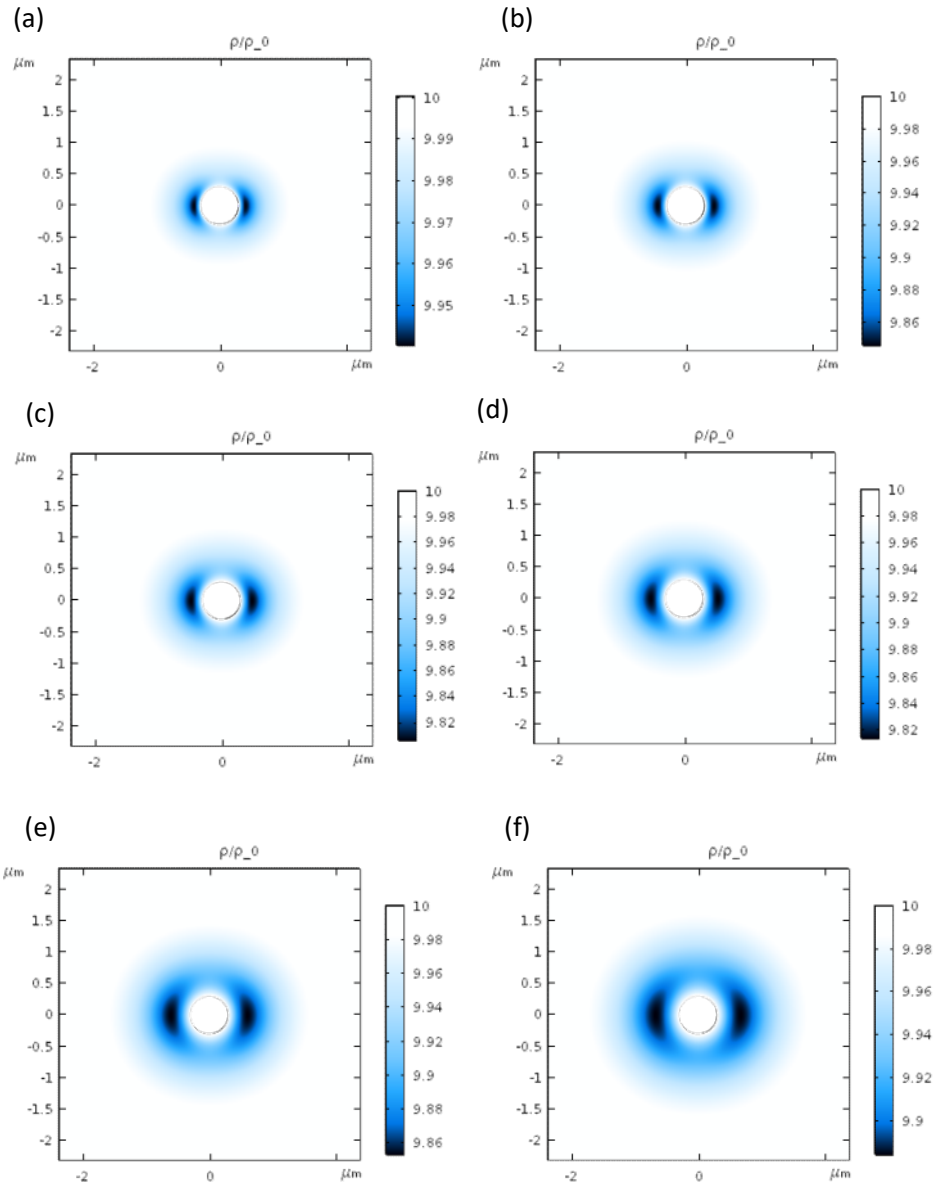

Fig. 6.6 The evolution of the density distribution at time point of 5, 10, 15, 20, 30 and 40 ns after the pulsed pump is on.

From the density distribution as shown in Fig. 6.6, the RI change can be directly obtained according to Equ. (6.5). Then still using the FEM method, the mode index of the two fundamental modes for a 1620 nm light beam guided along the 600 nm-diameter nanofiber can be calculated, as listed in Table 6.1.

Table 6.1 Parameters of mode index for a 1620 nm light beam propagating through the 600 nm-diameter nanofiber modified by transient PT effect.

Time	5 ns	10 ns	15 ns	20 ns	30 ns	40 ns
$N_{eff,x}$	1.0227135	1.0226967	1.0226865	1.0226850	1.0226892	1.0226942
$N_{eff,y}$	1.0227147	1.0226997	1.0226902	1.0226883	1.0226913	1.0226956
ΔN_{eff}	1.2×10^{-6}	3.0×10^{-6}	3.7×10^{-6}	3.3×10^{-6}	2.1×10^{-6}	1.4×10^{-6}
$L_b\ (cm)$	134	54	44	50	76	116

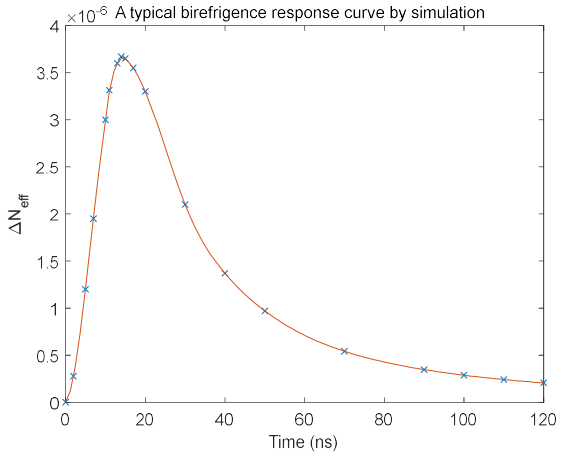

Fig. 6.7 Simulated birefringence response for acetylene of 10 bar and pump width of 10 ns.

A maximum birefringence of 3.7×10^{-6} is obtained around the time of 15 ns. The rising and falling time denoted as τ_r and τ_f are defined as the time required for the birefringence rises and

drops to the 90 % and 10 % of the maximum value. Then for the above case, it is found that the τ_r and τ_f are respectively 11 and 70 ns, according to the fitted response function of birefringence shown in Fig. 6.7.

6.3 All-optical polarization switching

The transient birefringence induced by the photothermal dynamics can be applied for all-optical polarization switching, in which the birefringent nanofiber works as a wave retarder with the Jones matrix representation denoted as $\begin{bmatrix} 1 & 0 \\ 0 & e^{i\phi} \end{bmatrix}$. Listed in Table 6.1 is also the polarization beating length L_b. The L_b is just the double of the polarization switching length L_s, which is the length required for the 45° linearly polarized input beam $\begin{bmatrix} 1 \\ 1 \end{bmatrix}$ switched to 135° $\begin{bmatrix} 1 \\ -1 \end{bmatrix}$ with respect to the x-axis. In this situation, the birefringent nanofiber working as a half wave retarder with the phase retardation $\phi = \pi$. For the maximum birefringence achieved at 15 ns, the switching length and thus the waist length of nanofiber is as high as 22 cm, which is quite impractical. However, as long as the gas pressure is sufficiently high, the relation between the pump level and the amplitude of the transient birefringence is approximately linear, so the switching level can be proportionally reduced by improving the pump level. For example, still with the pure acetylene of 10 bar and pump width of 10 ns but improving the pump level to 10 W, the ΔN_{eff} at 15 ns for the same 1620 nm beam is

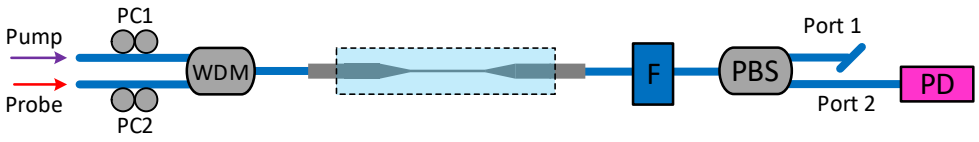

Fig. 6.8 The experimental setup for the nanofiber based polarization switch. Both the waist and transition region of the nanofiber are sealed in a gas chamber filled with pure acetylene, depicted as the blue area embraced by the dashed line. PBS: polarization beam splitter. F: optical filter for elimination of pump beam.

found to be 4.9×10^{-5}, resulting in a switching length of only 1.7 cm, which length is quite common for an optical nanofiber.

The experiments are performed with a 15 mm long and ~ 600 nm-diameter nanofiber taper-drawn from the SMF with transmission loss less than 0.3 db. The experimental setup is shown in Fig. 6.8. The pump beam is of 1532.83 nm corresponding to the P13 absorption line of acetylene while the probe beam is at 1555 nm, where there is basically no absorption. The pump beam is initially offered by a DFB laser of 3 MHz linewidth and then shaped by an AOM into pulsed output with width of ~ 15 ns. After being amplified by an EDFA, it is then injected into the system as depicted by the purple marked arrow. The probe beam is offered by an ECDL with 300 kHz linewidth. The pump and probe beams are combined by a WDM and injected into the nanofiber together. After passing through the nanofiber, the pump beam is eliminated out by a filter, leaving only the probe beam entering the polarization beam splitter (PBS). As the output power from the two ports of the PBS are complementary with each other, the signal from only one beam needs to be monitored. The peak power of the pulsed pump is measured to be ~ 30 W before entering the nanofiber. At the beginning

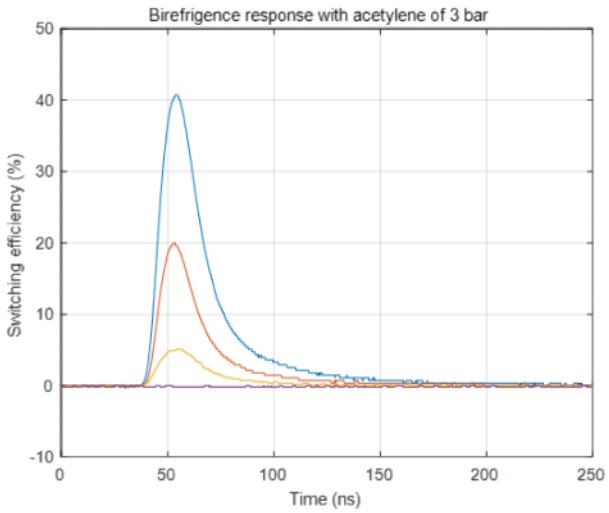

Fig. 6.9 Birefringence response in pure acetylene of 3 bar, under pulsed pump with different polarization state.

of each group of experiments, the polarization state of the probe beam is adjusted and then fixed so that there is no portion of the probe getting out from the port 2 or in another word, the probe beam is totally transferred to the port 1. Then any birefringence change in nanofiber can be reflected as the power change monitored by the photodetector.

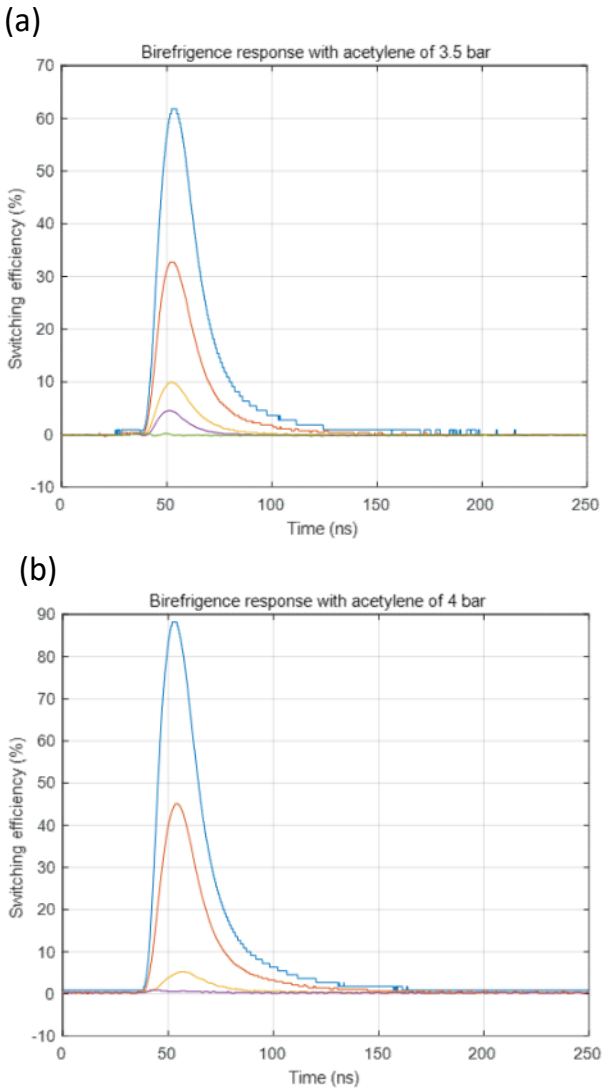

Fig. 6.10 Birefringence response in pure acetylene of (a) 3.5 bar and (b) 4 bar, under the pulsed pump with different polarization state.

The first group of experiments are performed with pure acetylene of 3 bar, as shown in Fig. 6.9,

where the pulsed pump is on at fixed time point of 40 ns. The different trace correspond to the different polarization states of the pump beam. The blue trace is the one where the highest birefringence can be achieved. It can be seen that under the pressure of 3 bar, the 30 W pulsed pump is not enough to result in a complete polarization switch. However, instead of increasing the pump power, pressurization should be a more convenient way to enhance the maximum birefringence and thus to realize a complete switch. As illustrated in the previous section, the higher the pressure, the faster the nonuniform temperature distribution will be established. This proposition is verified by the experimental results as demonstrated in Fig. 6.10.

As seen from the Fig. 6.10(a) and 6.10(b), the maximum switching efficiency as well as the birefringence are improved from 40 % to 60 % and 90 % respectively, by increasing the acetylene pressure to 3.5 and 4 bar. For the last group with acetylene of 4 bar, the switch-on and switching-off time are determined to be 11 and 37 ns, respectively. Compared with the simulation results, the experimentally measured switching-on time matches well but the switching-off time is nearly two times shorter. The experimental results match well with the theoretical ones in stage of birefringence generation but has a higher drops rate in the erasing process. The mismatch should come from the

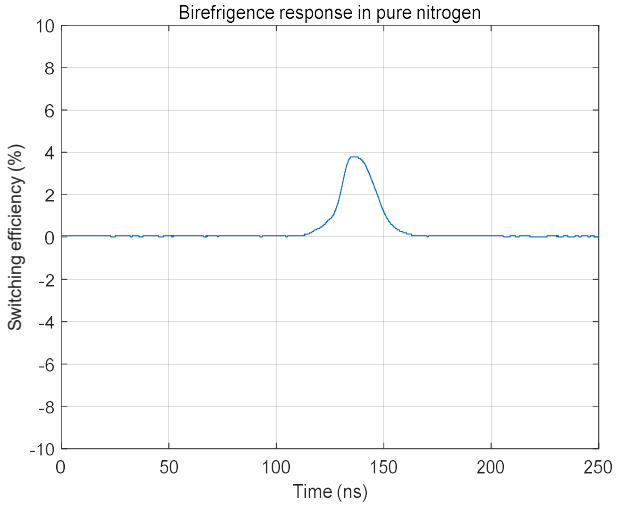

Fig. 6.11 The largest Birefringence response in pure nitrogen.

neglect of convection in the simulation. In the thermal convection, the heated gas goes up due to the buoyancy and making the elimination of the inhomogeneous temperature distribution faster. Experiments are also conducted where the acetylene is replaced with nitrogen to confirm that the switching effect does originate from the pump absorption of the ambient acetylene. It is found that the maxima switching efficiency for nanofiber in pure nitrogen is about 4%, as shown in Fig. 6.11. This residual transient birefringence does not originate from the direct absorption of the nanofiber itself, but comes from the Kerr effect, in consideration of the fast drop in the trailing edge.

6.4 Summary

The phenomenon of transient birefringence induced by the photothermal dynamics in the nanofiber is described and studied. This transient birefringence originates from the 2-fold rotational symmetric density distribution of the gas molecules excited by the linearly polarized input pump beam, as verified by the numerical simulation. Based on this effect, an all-optical polarization switching is demonstrated. With a piece of 15 mm long and 600 nm-diameter nanofiber in pure acetylene of 4 bar, a polarization switch with efficiency of 90 %, switching -on and -off time of 11 and 37 ns is achieved, under a 15 ns pulsed pump with peak power of 30 W. It is found that the switching efficiency depends not only on the pump power, but also on the pressure and the relative polarization configuration between the pump and the signal beams. Further reduction of the switching time as well as improvement of the efficiency can be realized by either pressurization or inflation of buffer gas with higher thermal conductivity, such as hydrogen.

Chapter 7 Conclusions and future works

7.1 Conclusions

The nanofiber based spectroscopic gas sensing is presented as well as the potential ability of light manipulation. The main contributions of this thesis are summarized as follow:

The nanofiber enhanced PTI spectroscopy for trace gas sensing is demonstrated with the clearly explained principles by both numerical simulation and experiments. The absorbed evanescent field of pump results in the temperature rise of the air surrounding the nanofiber. Through thermal conduction, the temperature of the nanofiber is also increased as well as it RI. The much higher thermo-optic coefficient greatly enhances the phase modulation amplitude compared with the free-space and HC-PBG fiber counterparts. Using a piece of 15 mm long and 800 nm-diameter silica nanofiber, trace acetylene detection limit of 600 ppb has been achieved. In addition, it is anticipated that by replacing the silica with materials that has much higher thermo-optic coefficients for fabrication of the nano-fiber/waveguide, even further tremendous enhancement in photothermal signal could be achieved.

The nanofiber enhanced SRS for highly sensitive trace hydrogen detection with fast response is presented. The enhancement effect originates from both the higher SRS efficiency due to the highly intensive evanescent field associated with the nanofiber and the low noise level thanks to the single-mode operation. Using a piece of 48 mm long and 700 nm-diameter silica nanofiber, trace hydrogen detection limit of 3 ppm has been achieved with fast response less than 10 s. The influence of polarization states of both the pump and Stokes beams on the Raman signal is also investigated. The polarization change is the main reason for long term drift.

The transit time broadening effect in nanofiber based spectroscopy is presented. Different from the

traditional free space and the HC-PBG fiber platform, the mode field area of nanofiber is much reduced, making the transit time broadening effect promoted. For the gas sensing application which is basically performed at atmospheric pressure, the transit time effect for the light absorbing molecules at near infrared band is actually negligible and the overall linewidth is determined by the collisional broadening. However, for the SRS of pure hydrogen, the dominant broadening factor is the transit time effect for the S_{00} rotational transition, even at the atmospheric pressure.

The phenomenon of transient birefringence in nanofiber which originates from the photothermal dynamics is studied. When absorbed by the ambient gas molecules, the two-fold rotational symmetric evanescent field will excite a transient temperature distribution in the similar shape, which then leads to birefringence in the nanofiber. An application of all-optical nanofiber polarization switching based on the transient photothermal effect is demonstrated. With a piece of 15 mm long and 600 nm diameter nanofiber, the polarization switch with switching efficiency of 90 % and switch-on and off time of 11 and 37 ns has been realized.

It should be mentioned that there are still some limitations of nanofiber based spectroscopic gas detection for real-time applications. First, the nanofiber needs to be well protected from pollution, so the dust or even water vapor filter are required to prolong the operating lifetime. Second, different from the hollow-core fiber, where there is basically no light power within the silica, the silica material at the waist region needs to withstand the highest light intensity in the whole system. The reliability of long-term operation, especially with a relatively high power cw beam, deserves further investigation.

7.2 Future works

It has been demonstrated that the nanofiber is a good platform for spectroscopic gas sensing. Some suggestions for the future works are given as follow:

1) Considering the much larger thermo-optic and thermal expansion coefficients of the polymer

materials, nanofibers made form polymer should have much larger phase modulation and thus photothermal signal compared with the currently adopted silica nanofiber.

2) The polarization drift is inevitable in the present system which makes the reliability in real application. For realization of polarization insensitivity, either the polarization scrambler that averages out all the polarization states or highly birefringent optical nano/microfiber combined with polarization maintaining transmission link may be adopted.

3) The remarkable transit time broadening in SRS of hydrogen on nanofiber platform may be suppressed by pressurization which reduces the mean free path and thus increases the time that the hydrogen molecules stay in the evanescent field. This should be an analogy of buffering gas narrowing in atomic spectroscopy, but the buffering gas is the hydrogen itself in the nanofiber case.

4) In the nanofiber photothermal based polarization switch, the switching on and off time could be further reduced by buffering gas. Especially for the latter one, by adding buffering gas with much higher thermal conductivity, such as hydrogen, the switching off time could be remarkably shortened.

References

[1] X. Liu, S. Cheng, H. Liu, S. Hu, D. Zhang, and H. Ning, "A survey on gas sensing technology," *Sensors,* vol. 12, pp. 9635-9665, 2012.

[2] T. Liu, Y. Wei, G. Song, Y. Li, J. Wang, Y. Ning*, et al.*, "Advances of optical fiber sensors for coal mine safety monitoring applications," in *2013 International Conference on Microwave and Photonics (ICMAP)*, 2013, pp. 1-5.

[3] G. G. Gifford and B. E. Osborn, "Method and system employing optical emission spectroscopy for monitoring and controlling semiconductor fabrication," ed: Google Patents, 1994.

[4] G. Plant, M. Nikodem, P. Mulhall, R. Varner, D. Sonnenfroh, and G. Wysocki, "Field test of a remote multi-path CLaDS methane sensor," *Sensors,* vol. 15, pp. 21315-21326, 2015.

[5] B. Buszewski, M. Kęsy, T. Ligor, and A. Amann, "Human exhaled air analytics: biomarkers of diseases," *Biomedical chromatography,* vol. 21, pp. 553-566, 2007.

[6] J. Wang, "Electrochemical sensing of explosives," *Electroanalysis: An International Journal Devoted to Fundamental and Practical Aspects of Electroanalysis,* vol. 19, pp. 415-423, 2007.

[7] D. Matthews and J. Hayes, "Isotope-ratio-monitoring gas chromatography-mass spectrometry," *Analytical Chemistry,* vol. 50, pp. 1465-1473, 1978.

[8] A. Pittet, A. Périsset, and J.-M. Oberson, "Trace level determination of acrylamide in cereal-based foods by gas chromatography–mass spectrometry," *Journal of Chromatography A,* vol. 1035, pp. 123-130, 2004.

[9] A. Azad, S. Akbar, S. Mhaisalkar, L. Birkefeld, and K. Goto, "Solid-state gas sensors: A review," *Journal of the Electrochemical Society,* vol. 139, pp. 3690-3704, 1992.

[10] M. J. Tierney and H. O. L. Kim, "Electrochemical gas sensor with extremely fast response times," *Analytical Chemistry,* vol. 65, pp. 3435-3440, 1993.

[11] L. P. Martin, A.-Q. Pham, and R. S. Glass, "Electrochemical hydrogen sensor for safety monitoring," *Solid State Ionics,* vol. 175, pp. 527-530, 2004.

[12] G. Matz, T. Hunte, and W. Schröder, "Hand-portable gas-detector array (GDA) for rapid field detection and identification of chemical threat," *Field Analytical Chemistry & Technology,* vol. 4, pp. 195-203, 2000.

[13] P. A. Smith, C. J. Lepage, K. L. Harrer, and P. J. Brochu, "Hand-held photoionization instruments for quantitative detection of sarin vapor and for rapid qualitative screening of contaminated objects," *Journal of occupational and environmental hygiene,* vol. 4, pp. 729-738, 2007.

[14] R. A. Hites, "Development of gas chromatographic mass spectrometry," *Analytical chemistry,* vol. 88, pp. 6955-6961, 2016.

[15] X. Lu, S. Wu, L. Wang, and Z. Su, "Solid-state amperometric hydrogen sensor based on polymer electrolyte membrane fuel cell," *Sensors and Actuators B: Chemical,* vol. 107, pp. 812-817, 2005.

[16] S. Kawashima and S. Yonemura, "Measuring ammonia concentration over a grassland near livestock facilities using a semiconductor ammonia sensor," *Atmospheric Environment,* vol. 35, pp. 3831-3839, 2001.

[17] C.-H. Han, D.-U. Hong, J. Gwak, and S.-D. Han, "A planar catalytic combustion sensor using nano-crystalline F-doped SnO 2 as a supporting material for hydrogen detection," *Korean Journal of Chemical Engineering,* vol. 24, pp. 927-931, 2007.

[18] T. Hübert, L. Boon-Brett, G. Black, and U. Banach, "Hydrogen sensors–a review," *Sensors and Actuators B: Chemical,* vol. 157, pp. 329-352, 2011.

[19] G. Korotcenkov, S. D. Han, and J. R. Stetter, "Review of electrochemical hydrogen sensors," *Chemical reviews,* vol. 109, pp. 1402-1433, 2009.

[20] G. Maureenv. (2009). *Fraunhofer lines: Solar spectrum with Fraunhofer lines as it appears visually*. Available: https://en.wikipedia.org/wiki/File:Fraunhofer_lines.svg#filelinks

[21] J. Hodgkinson and R. P. Tatam, "Optical gas sensing: a review," *Measurement Science and Technology,* vol. 24, p. 012004, 2012.

[22] P. Werle, F. Slemr, K. Maurer, R. Kormann, R. Mücke, and B. Jänker, "Near-and mid-infrared laser-optical sensors for gas analysis," *Optics and lasers in engineering,* vol. 37, pp. 101-114, 2002.

[23] H. Schiff, G. Mackay, and J. Bechara, "The use of tunable diode laser absorption spectroscopy for atmospheric measurements," *Research on chemical intermediates,* vol. 20, pp. 525-556, 1994.

[24] M. Hollas, *Modern Spectroscopy*, fourth ed. England: John Wiley & Sons, 2004.

[25] J. Ye, L.-S. Ma, and J. L. Hall, "Ultrasensitive detections in atomic and molecular physics: demonstration in molecular overtone spectroscopy," *Journal of the Optical Society of America B,* vol. 15, pp. 6-15, 1998/01/01 1998.

[26] J.-F. Doussin, R. Dominique, and C. Patrick, "Multiple-pass cell for very-long-path infrared spectrometry," *Applied optics,* vol. 38, pp. 4145-4150, 1999.

[27] D. Halmer, G. Von Basum, P. Hering, and M. Mürtz, "Mid-infrared cavity leak-out spectroscopy for ultrasensitive detection of carbonyl sulfide," *Optics letters,* vol. 30, pp. 2314-2316, 2005.

[28] A. van Brakel, C. Jáuregui Misas, T. T. Ng, P. Petropoulos, J. P. Dakin, C. Grivas*, et al.*, "Cavity Ring-down in a Photonic Bandgap Fiber Gas Cell," in *Conference on Lasers and Electro-Optics/Quantum Electronics and Laser Science Conference and Photonic Applications Systems Technologies*, San Jose, California, 2008, p. CThEE4.

[29] G. C. Bjorklund, M. D. Levenson, W. Lenth, and C. Ortiz, "Frequency modulation (FM) spectroscopy," *Applied Physics B,* vol. 32, pp. 145-152, November 01 1983.

[30] J. Reid and D. Labrie, "Second-harmonic detection with tunable diode lasers—comparison of experiment and theory," *Applied Physics B,* vol. 26, pp. 203-210, 1981.

[31] J. Stone, "Measurements of the Absorption of Light in Low-Loss Liquids," *Journal of the Optical Society of America,* vol. 62, pp. 327-333, 1972/03/01 1972.

[32] C. C. Davis, "Trace detection in gases using phase fluctuation optical heterodyne spectroscopy," *Applied Physics Letters,* vol. 36, pp. 515-518, 1980.

[33] W. Jin, Y. Cao, F. Yang, and H. L. Ho, "Ultra-sensitive all-fibre photothermal spectroscopy with large dynamic range," *Nature communications,* vol. 6, 2015.

[34] A. Kosterev, Y. A. Bakhirkin, R. Curl, and F. Tittel, "Quartz-enhanced photoacoustic spectroscopy," *Optics Letters,* vol. 27, pp. 1902-1904, 2002.

[35] S. Bialkowski, *Photothermal Spectroscopy Methods for Chemical Analysis*: Wiley, 1996.

[36] B. Culshaw, G. Stewart, F. Dong, C. Tandy, and D. Moodie, "Fibre optic techniques for remote spectroscopic methane detection—from concept to system realisation," *Sensors and actuators B: chemical,* vol. 51, pp. 25-37, 1998.

[37] J. Dakin and B. Culshaw, "Optical fiber sensors: Principles and components. Volume 1," *Boston, MA, Artech House, 1988, 343 p. For individual items see A90-36770 to A90-36775.,* 1988.

[38] B. Lee, "Review of the present status of optical fiber sensors," *Optical fiber technology,* vol. 9, pp. 57-79, 2003.

[39] H. L. Ho, W. Jin, and M. Demokan, "Quantitative measurement of acetylene by using external-cavity tunable diode laser," *Proceedings of SPIE - The International Society for Optical Engineering,* 12/08 1999.

[40] H. L. Ho, J. Ju, and W. Jin, "Fiber optic gas detection system for health monitoring of oil-filled transformer," *Proceedings of SPIE - The International Society for Optical Engineering,* vol. 7503, 10/01 2009.

[41] F. Muhammad, G. Stewart, and W. Jin, "Sensitivity enhancement of D-fibre methane gas sensor using high-index overlay," *IEE Proceedings J (Optoelectronics),* vol. 140, pp. 115-118, 1993.

[42] H. Tai, H. Tanaka, and T. Yoshino, "Fiber-optic evanescent-wave methane-gas sensor using optical absorption for the 3.392-μm line of a He–Ne laser," *Optics Letters,* vol. 12, pp. 437-439, 1987/06/01 1987.

[43] J. Lou, Y. Wang, and L. Tong, "Microfiber optical sensors: A review," *Sensors,* vol. 14, pp. 5823-5844, 2014.

[44] B. Lee, S. Roh, and J. Park, "Current status of micro- and nano-structured optical fiber sensors," *Optical Fiber Technology,* vol. 15, pp. 209-221, 6// 2009.

[45] C. M. Smith, N. Venkataraman, M. T. Gallagher, D. Müller, J. A. West, N. F. Borrelli*, et al.*, "Low-loss hollow-core silica/air photonic bandgap fibre," *Nature,* vol. 424, pp. 657-659, 2003.

[46] M. I. Hasan, N. Akhmediev, and W. Chang, "Mid-infrared supercontinuum generation in supercritical xenon-filled hollow-core negative curvature fibers," *Optics Letters,* vol. 41, pp. 5122-5125, 2016/11/01 2016.

[47] M. Cassataro, D. Novoa, M. C. Günendi, N. N. Edavalath, M. H. Frosz, J. C. Travers*, et al.*, "Generation of broadband mid-IR and UV light in gas-filled single-ring hollow-core PCF," *Optics Express,* vol. 25, pp. 7637-7644, 2017/04/03 2017.

[48] F. Belli, A. Abdolvand, W. Chang, J. C. Travers, and P. S. J. Russell, "Vacuum-ultraviolet to infrared supercontinuum in hydrogen-filled photonic crystal fiber," *Optica,* vol. 2, pp. 292-300, 2015/04/20 2015.

[49] R. A. Bartels, A. Paul, H. Green, H. C. Kapteyn, M. M. Murnane, S. Backus*, et al.*, "Generation of spatially coherent light at extreme ultraviolet wavelengths," *Science,* vol. 297, pp. 376-378, 2002.

[50] A. Hoffmann, M. Zürch, M. Gräfe, and C. Spielmann, "Spectral broadening and compression of sub-millijoule laser pulses in hollow-core fibers filled with sulfur hexafluoride," *Optics Express,* vol. 22, pp. 12038-12045, 2014.

[51] V. Cardin, N. Thiré, S. Beaulieu, V. Wanie, F. Légaré, and B. E. Schmidt, "0.42 TW 2-cycle pulses at 1.8 μ m via hollow-core fiber compression," *Applied Physics Letters,* vol. 107, p. 181101, 2015.

[52] A. Abdolvand, A. M. Walser, M. Ziemienczuk, T. Nguyen, and P. S. J. Russell, "Generation of a phase-locked Raman frequency comb in gas-filled hollow-core photonic crystal fiber," *Optics Letters,* vol. 37, pp. 4362-4364, 2012/11/01 2012.

[53] F. Tani, F. Belli, A. Abdolvand, J. C. Travers, and P. S. J. Russell, "Generation of three-octave-spanning transient Raman comb in hydrogen-filled hollow-core PCF," *Optics Letters,* vol. 40, pp. 1026-1029, 2015/03/15 2015.

[54] G. Humbert, J. C. Knight, G. Bouwmans, P. S. J. Russell, D. P. Williams, P. J. Roberts*, et al.*, "Hollow core photonic crystal fibers for beam delivery," *Optics Express,* vol. 12, pp. 1477-1484, 2004/04/19 2004.

[55] A. F. Kosolapov, A. D. Pryamikov, A. S. Biriukov, V. S. Shiryaev, M. S. Astapovich, G. E. Snopatin*, et al.*, "Demonstration of CO2-laser power delivery through chalcogenide-glass fiber with negative-curvature hollow core," *Optics Express,* vol. 19, pp. 25723-25728, 2011/12/05 2011.

[56] F. Benabid, F. Couny, J. C. Knight, T. A. Birks, and P. S. J. Russell, "Compact, stable and efficient all-fibre gas cells using hollow-core photonic crystal fibres," *Nature,* vol. 434, pp. 488-491, 03/24/print 2005.

[57] F. Yang, W. Jin, Y. Cao, H. L. Ho, and Y. Wang, "Towards high sensitivity gas detection with hollow-core photonic bandgap fibers," *Optics Express,* vol. 22, pp. 24894-24907, 2014/10/06 2014.

[58] M. P. Buric, K. P. Chen, J. Falk, and S. D. Woodruff, "Enhanced spontaneous Raman scattering and gas composition analysis using a photonic crystal fiber," *Applied Optics,* vol. 47, pp. 4255-4261, 2008.

[59] S. Hanf, T. Bögözi, R. Keiner, T. Frosch, and J. r. Popp, "Fast and highly sensitive fiber-enhanced Raman spectroscopic monitoring of molecular H2 and CH4 for point-of-care diagnosis of malabsorption disorders in exhaled human breath," *Analytical chemistry,* vol. 87, pp. 982-988, 2014.

[60] S. Hanf, R. Keiner, D. Yan, J. r. Popp, and T. Frosch, "Fiber-enhanced Raman multigas spectroscopy: a versatile tool for environmental gas sensing and breath analysis," *Analytical chemistry,* vol. 86, pp. 5278-5285, 2014.

[61] F. Yang, W. Jin, Y. Lin, C. Wang, H. L. Ho, and Y. Tan, "Hollow-core Microstructured Optical Fiber Gas Sensors," *Journal of Lightwave Technology,* vol. 35, pp. 3413-3424, 2016.

[62] F. Yang, Y. Tan, W. Jin, Y. Lin, Y. Qi, and H. L. Ho, "Hollow-core fiber Fabry–Perot photothermal gas sensor," *Optics Letters,* vol. 41, pp. 3025-3028, 2016/07/01 2016.

[63] Y. Zhao, W. Jin, Y. Lin, F. Yang, and H. L. Ho, "All-fiber gas sensor with intracavity photothermal spectroscopy," *Optics letters,* vol. 43, pp. 1566-1569, 2018.

[64] F. Yang and W. Jin, "All-fiber hydrogen sensor based on stimulated Raman gain spectroscopy with a 1550 nm hollow-core fiber," in *Optical Fiber Sensors Conference (OFS), 2017 25th*, 2017, pp. 1-4.

[65] F. Yang, Y. Zhao, Y. Qi, Y. Z. Tan, H. L. Ho, and W. Jin, "Towards label-free distributed fiber hydrogen sensor with stimulated Raman spectroscopy," *Optics Express,* vol. 27, pp. 12869-12882, 2019/04/29 2019.

[66] P. G. Westergaard, M. Lassen, and J. C. Petersen, "Differential high-resolution stimulated CW Raman spectroscopy of hydrogen in a hollow-core fiber," *Optics express,* vol. 23, pp. 16320-16328, 2015.

[67] B. S. Kawasaki and K. O. Hill, "Low-loss access coupler for multimode optical fiber distribution networks," *Applied Optics,* vol. 16, pp. 1794-1795, 1977/07/01 1977.

[68] B. S. Kawasaki, K. O. Hill, and R. G. Lamont, "Biconical-taper single-mode fiber coupler," *Optics Letters,* vol. 6, pp. 327-328, 1981/07/01 1981.

[69] T. A. Birks, S. G. Farwell, P. S. J. Russell, and C. N. Pannell, "Four-port fiber frequency shifter with a null taper coupler," *Optics Letters,* vol. 19, pp. 1964-1966, 1994/12/01 1994.

[70] L. Tong, R. R. Gattass, J. B. Ashcom, S. He, J. Lou, M. Shen*, et al.*, "Subwavelength-diameter silica wires for low-loss optical wave guiding," *Nature,* vol. 426, pp. 816-819, 2003.

[71] S. G. Leon-Saval, T. A. Birks, W. J. Wadsworth, P. S. J. Russell, and M. W. Mason, "Supercontinuum generation in submicron fibre waveguides," *Optics Express,* vol. 12, pp. 2864-2869, 2004/06/28 2004.

[72] G. Brambilla, V. Finazzi, and D. J. Richardson, "Ultra-low-loss optical fiber nanotapers," *Optics*

Express, vol. 12, pp. 2258-2263, 2004.

[73] T. Birks and Y. W. Li, "The shape of fiber tapers," *Journal of Lightwave Technology,* vol. 10, pp. 432-438, 1992.

[74] F. Le Kien, J. Liang, K. Hakuta, and V. Balykin, "Field intensity distributions and polarization orientations in a vacuum-clad subwavelength-diameter optical fiber," *Optics Communications,* vol. 242, pp. 445-455, 2004.

[75] G. Brambilla, "Optical fibre nanowires and microwires: a review," *Journal of Optics,* vol. 12, p. 043001, 2010.

[76] G. Brambilla, F. Xu, P. Horak, Y. Jung, F. Koizumi, N. P. Sessions*, et al.*, "Optical fiber nanowires and microwires: fabrication and applications," *Advances in Optics and Photonics,* vol. 1, pp. 107-161, 2009/01/30 2009.

[77] T. A. Birks, W. J. Wadsworth, and P. S. J. Russell, "Supercontinuum generation in tapered fibers," *Optics Letters,* vol. 25, pp. 1415-1417, 2000/10/01 2000.

[78] R. R. Gattass, G. T. Svacha, L. Tong, and E. Mazur, "Supercontinuum generation in submicrometer diameter silica fibers," *Optics Express,* vol. 14, pp. 9408-9414, 2006.

[79] D. D. Hudson, S. Antipov, L. Li, I. Alamgir, T. Hu, M. E. Amraoui*, et al.*, "Toward all-fiber supercontinuum spanning the mid-infrared," *Optica,* vol. 4, pp. 1163-1166, 2017/10/20 2017.

[80] X. Liu, C. Xu, W. Knox, J. Chandalia, B. Eggleton, S. Kosinski*, et al.*, "Soliton self-frequency shift in a short tapered air–silica microstructure fiber," *Optics Letters,* vol. 26, pp. 358-360, 2001.

[81] M. A. Foster, A. L. Gaeta, Q. Cao, and R. Trebino, "Soliton-effect compression of supercontinuum to few-cycle durations in photonic nanowires," *Optics Express,* vol. 13, pp. 6848-6855, 2005/09/05 2005.

[82] V. Grubsky and A. Savchenko, "Glass micro-fibers for efficient third harmonic generation," *Optics express,* vol. 13, pp. 6798-6806, 2005.

[83] V. Grubsky and J. Feinberg, "Phase-matched third-harmonic UV generation using low-order modes in a glass micro-fiber," *Optics Communications,* vol. 274, pp. 447-450, 2007/06/15/ 2007.

[84] R. Ismaeel, T. Lee, M. Ding, N. G. Broderick, and G. Brambilla, "Nonlinear microfiber loop resonators for resonantly enhanced third harmonic generation," *Optics letters,* vol. 37, pp. 5121-5123, 2012.

[85] M. Morrissey, K. Deasy, M. Frawley, R. Kumar, E. Prel, L. Russell*, et al.*, "Spectroscopy, manipulation and trapping of neutral atoms, molecules, and other particles using optical nanofibers: a review," *Sensors,* vol. 13, pp. 10449-10481, 2013.

[86] F. Le Kien, V. Balykin, and K. Hakuta, "Atom trap and waveguide using a two-color evanescent light field around a subwavelength-diameter optical fiber," *Physical Review A,* vol. 70, p. 063403, 2004.

[87] P. Solano, F. K. Fatemi, L. A. Orozco, and S. Rolston, "Dynamics of trapped atoms around an optical nanofiber probed through polarimetry," *Optics Letters,* vol. 42, pp. 2283-2286, 2017.

[88] H. Xin, R. Xu, and B. Li, "Optical trapping, driving, and arrangement of particles using a tapered fibre probe," *Scientific reports,* vol. 2, p. 818, 2012.

[89] L. Zhang, F. Gu, J. Lou, X. Yin, and L. Tong, "Fast detection of humidity with a subwavelength-diameter fiber taper coated with gelatin film," *Optics express,* vol. 16, pp. 13349-13353, 2008.

[90] Y. Liao, J. Wang, H. Yang, X. Wang, and S. Wang, "Salinity sensing based on microfiber knot resonator," *Sensors and Actuators A: Physical,* vol. 233, pp. 22-25, 2015.

[91] Y. Huang, Z. Tian, L.-P. Sun, D. Sun, J. Li, Y. Ran*, et al.*, "High-sensitivity DNA biosensor based on optical fiber taper interferometer coated with conjugated polymer tentacle," *Optics express,* vol. 23, pp. 26962-26968, 2015.

[92] Y. Wu, B. Yao, A. Zhang, Y. Rao, Z. Wang, Y. Cheng*, et al.*, "Graphene-coated microfiber Bragg grating for high-sensitivity gas sensing," *Optics letters,* vol. 39, pp. 1235-1237, 2014.

[93] K. Schroeder, W. Ecke, and R. Willsch, "Optical fiber Bragg grating hydrogen sensor based on evanescent-field interaction with palladium thin-film transducer," *Optics and Lasers in Engineering,* vol. 47, pp. 1018-1022, 2009.

[94] P. F. Bernath, *Spectra of atoms and molecules*: Oxford university press, 2015.

[95] J. I. Steinfeld, *Molecules and radiation: An introduction to modern molecular spectroscopy*: Courier Corporation, 2012.

[96] N. M. Laurendeau, *Statistical Thermodynamics: Fundamentals and Applications*: Cambridge University Press, 2005.

[97] W. Demtröder, *Laser Spectroscopy*, 2008.

[98] D. A. Long, *The Raman Effect*: Wiley, 2002.

[99] J. Reid, J. Shewchun, B. Garside, and E. Ballik, "High sensitivity pollution detection employing tunable diode lasers," *Applied optics,* vol. 17, pp. 300-307, 1978.

[100] D. Rojas, P. Ljung, and O. Axner, "An investigation of the 2f—wavelength modulation technique for detection of atoms under optically thin as well as thick conditions," *Spectrochimica Acta Part B: Atomic Spectroscopy,* vol. 52, pp. 1663-1686, 1997.

[101] C. C. Davis and S. J. Petuchowski, "Phase fluctuation optical heterodyne spectroscopy of gases," *Applied Optics,* vol. 20, pp. 2539-2554, 1981.

[102] M. A. Owens, C. C. Davis, and R. R. Dickerson, "A Photothermal Interferometer for Gas-Phase Ammonia Detection," *Analytical Chemistry,* vol. 71, pp. 1391-1399, 1999.

[103] Y. Lin, W. Jin, F. Yang, J. Ma, C. Wang, H. L. Ho*, et al.*, "Pulsed photothermal interferometry for spectroscopic gas detection with hollow-core optical fibre," *Scientific Reports,* vol. 6, p. 39410, 2016.

[104] Y. Lin, W. Jin, F. Yang, Y. Tan, and H. L. Ho, "Performance optimization of hollow-core fiber photothermal gas sensors," *Optics Letters,* vol. 42, pp. 4712-4715, 2017/11/15 2017.

[105] J. H. Lienhard, *A heat transfer textbook*: Courier Corporation, 2013.

[106] A. W. Snyder and J. Love, *Optical waveguide theory*: Springer Science & Business Media, 2012.

[107] K. Kråkenes and K. Bløtekjaer, "Sagnac interferometer for underwater sound detection: noise properties," *Optics Letters,* vol. 14, pp. 1152-1154, 1989.

[108] R. Bartolo, A. Tventen, C. Kirkendall, P. Juodawlkis, W. Loh, and J. Plant, "Characterization of a Low-phase-noise, High-power (370 mW), External-cavity Semiconductor Laser," DTIC Document2010.

[109] Y. Qi, F. Yang, Y. Lin, W. Jin, and H. L. Ho, "Nano-waveguide enhanced photothermal interferometry spectroscopy," *Journal of Lightwave Technology,* pp. 5267-5275, 2017.

[110] M. J. Weber, *Handbook of Optical Materials*: Taylor & Francis, 2002.

[111] K. Peters, "Polymer optical fiber sensors—a review," *Smart materials and structures,* vol. 20, p. 013002, 2010.

[112] P. E. Ciddor, "Refractive index of air: new equations for the visible and near infrared," *Applied optics,* vol. 35, pp. 1566-1573, 1996.

[113] D. B. Leviton and B. J. Frey, "Temperature-dependent absolute refractive index measurements of synthetic fused silica," 2006, pp. 62732K-62732K-11.

[114] R. Gravina, G. Testa, and R. Bernini, "Perfluorinated plastic optical fiber tapers for evanescent wave sensing," *Sensors,* vol. 9, pp. 10423-10433, 2009.

[115] G. Ghosh, *Handbook of optical constants of solids: Handbook of thermo-optic coefficients of optical materials with applications*: Academic Press, 1998.

[116] J. Gosciniak and S. I. Bozhevolnyi, "Performance of thermo-optic components based on dielectric-loaded surface plasmon polariton waveguides," *Scientific Reports,* vol. 3, p. 1803, 2013.

[117] A. Lacraz, M. Polis, A. Theodosiou, C. Koutsides, and K. Kalli, "Femtosecond Laser Inscribed Bragg Gratings in Low Loss CYTOP Polymer Optical Fiber," *IEEE Photonics Technology Letters,* vol. 27, pp. 693-696, 2015.

[118] W. H. Souder, P., "Measurements on the thermal expansion of fused silica," *Scientific Papers of the Bureau of Standards,* vol. 21, pp. 1-23, 1925.

[119] R. Van Laer, B. Kuyken, D. Van Thourhout, and R. Baets, "Interaction between light and highly confined hypersound in a silicon photonic nanowire," *Nature Photonics,* vol. 9, pp. 199-203, 2015.

[120] L. Xiao, M. Demokan, W. Jin, Y. Wang, and C.-L. Zhao, "Fusion splicing photonic crystal fibers and conventional single-mode fibers: microhole collapse effect," *Journal of lightwave technology,* vol. 25, pp. 3563-3574, 06 December 2007 2007.

[121] Y. L. Hoo, W. Jin, C. Shi, H. L. Ho, D. N. Wang, and S. C. Ruan, "Design and modeling of a photonic crystal fiber gas sensor," *Applied Optics,* vol. 42, pp. 3509-3515, 2003/06/20 2003.

[122] W. K. Bischel and M. J. Dyer, "Wavelength dependence of the absolute Raman gain coefficient for the Q (1) transition in H 2," *JOSA B,* vol. 3, pp. 677-682, 1986.

[123] O. Svelto and D. C. Hanna, *Principles of lasers* vol. 4: Springer, 1998.

[124] M. J. F. Digonnet, K. Hyang Kyun, G. S. Kino, and F. Shanhui, "Understanding air-core photonic-bandgap fibers: analogy to conventional fibers," *Lightwave Technology, Journal of,* vol. 23, pp. 4169-4177, 2005.

[125] F. Farahi, P. A. Leilabady, J. Jones, and D. Jackson, "Interferometric fibre-optic hydrogen sensor," *Journal of Physics E: Scientific Instruments,* vol. 20, p. 432, 1987.

[126] X. Wei, T. Wei, H. Xiao, and Y. Lin, "Nano-structured Pd-long period fiber gratings integrated optical sensor for hydrogen detection," *Sensors and Actuators B: Chemical,* vol. 134, pp. 687-693, 2008.

[127] J. S. Zeakes, K. A. Murphy, A. Elshabini-Riad, and R. O. Claus, "Modified extrinsic Fabry-Perot interferometric hydrogen gas sensor," in *Lasers and Electro-Optics Society Annual Meeting, 1994. LEOS'94 Conference Proceedings. IEEE*, 1994, pp. 235-236.

[128] X. Bevenot, A. Trouillet, C. Veillas, H. Gagnaire, and M. Clement, "Surface plasmon resonance hydrogen sensor using an optical fibre," *Measurement Science and Technology,* vol. 13, p. 118, 2001.

[129] M. Tabib-Azar, B. Sutapun, R. Petrick, and A. Kazemi, "Highly sensitive hydrogen sensors using palladium coated fiber optics with exposed cores and evanescent field interactions," *Sensors and actuators B: Chemical,* vol. 56, pp. 158-163, 1999.

[130] Y. Oki, S. Nakazono, Y. Nonaka, and M. Maeda, "Sensitive H2 detection by use of thermal-lens Raman spectroscopy without a tunable laser," *Optics Letters,* vol. 25, pp. 1040-1042, 2000/07/15 2000.

[131] R. Wynne and B. Barabadi, "Gas-filling dynamics of a hollow-core photonic bandgap fiber for nonvacuum conditions," *Applied Optics,* vol. 54, pp. 1751-1757, 2015.

[132] R. Minck, E. Hagenlocker, and W. Rado, "Stimulated pure rotational Raman scattering in deuterium," *Physical review letters,* vol. 17, p. 229, 1966.

[133] J. Carlsten and R. Wenzel, "Stimulated rotational Raman scattering in CO2-pumped para-H2," *IEEE journal of quantum electronics,* vol. 19, pp. 1407-1413, 1983.

[134] R. Ulrich, S. Rashleigh, and W. Eickhoff, "Bending-induced birefringence in single-mode fibers," *Optics letters,* vol. 5, pp. 273-275, 1980.

[135] Y. Jung, G. Brambilla, K. Oh, and D. J. Richardson, "Highly birefringent silica microfiber," *Optics letters,* vol. 35, pp. 378-380, 2010.

[136] H. Xuan, J. Ma, W. Jin, and W. Jin, "Polarization converters in highly birefringent microfibers," *Optics Express,* vol. 22, pp. 3648-3660, 2014/02/10 2014.

[137] C. J. Bordé, J. Hall, C. Kunasz, and D. Hummer, "Saturated absorption line shape: Calculation of the transit-time broadening by a perturbation approach," *Physical Review A,* vol. 14, p. 236, 1976.

[138] S. Hendrickson, M. Lai, T. Pittman, and J. Franson, "Observation of two-photon absorption at low power levels using tapered optical fibers in rubidium vapor," *Physical review letters,* vol. 105, p. 173602, 2010.

[139] M. de Labachelerie, K. Nakagawa, Y. Awaji, and M. Ohtsu, "High-frequency-stability laser at 1.5 μm using Doppler-free molecular lines," *Optics Letters,* vol. 20, pp. 572-574, 1995/03/15 1995.

[140] R. Thapa, K. Knabe, M. Faheem, A. Naweed, O. L. Weaver, and K. L. Corwin, "Saturated absorption spectroscopy of acetylene gas inside large-core photonic bandgap fiber," *Optics Letters,* vol. 31, pp. 2489-2491, 2006/08/15 2006.

[141] M. Takiguchi, Y. Yoshikawa, T. Yamamoto, K. Nakayama, and T. Kuga, "Saturated absorption spectroscopy of acetylene molecules with an optical nanofiber," *Optics Letters,* vol. 36, pp. 1254-1256, 2011/04/01 2011.

[142] N. V. Wheeler, M. D. Grogan, P. S. Light, F. Couny, T. A. Birks, and F. Benabid, "Large-core acetylene-filled photonic microcells made by tapering a hollow-core photonic crystal fiber," *Optics letters,* vol. 35, pp. 1875-1877, 2010.

[143] L. S. Rothman, D. Jacquemart, A. Barbe, D. C. Benner, M. Birk, L. Brown*, et al.*, "The HITRAN 2004 molecular spectroscopic database," *Journal of Quantitative Spectroscopy and Radiative Transfer,* vol. 96, pp. 139-204, 2005.

[144] W. K. Bischel and M. J. Dyer, "Temperature dependence of the Raman linewidth and line shift for the Q (1) and Q (0) transitions in normal and para-H 2," *Physical Review A,* vol. 33, p. 3113, 1986.

[145] G. Herring, M. J. Dyer, and W. K. Bischel, "Temperature and density dependence of the linewidths and line shifts of the rotational Raman lines in N2 and H2," *Physical Review A,* vol. 34, p. 1944, 1986.

[146] J. C. Wang and G. S. Springer, "Vibrational relaxation times in some hydrocarbons in the range 300–900 K," *The Journal of Chemical Physics,* vol. 59, pp. 6556-6562, 1973.